Technische Universität München

Fakultät für Medizin

Identification of Treatment-induced Vulnerabilities in Pancreatic Cancer

Katja Peschke

Vollständiger Abdruck der von der Fakultät für Medizin der Technischen Universität München zur Erlangung des akademischen Grades einer

Doktorin der Naturwissenschaften (Dr. rer. nat.)

genehmigten Dissertation.

Vorsitzender:	Prof. Dr. Marc Schmidt-Supprian
Prüfer der Dissertation:	1. Prof. Dr. Maximilian Reichert
	2. Prof. Dr. Heiko Witt
	3. Prof. Dr. Matthias Lauth

Die Dissertation wurde am 11.01.2022 bei der Fakultät für Medizin der Technischen Universität München eingereicht und durch die Fakultät für Medizin am 17.05.2022 angenommen.

Table of Contents

List of Figures

List of Tables

Abbreviations

°C	degree Celsius
2D	two-dimensional
3D	three-dimensional
5-FU	5-fluorouracil
ACN	acetonitrile
ADEX	aberrantly differentiated endocrine exocrine
APS	ammonium persulphate
aREA	analytic rank-based enrichment analysis
α-SMA	α-smooth muscle actin
ATP	adenosine triphosphate
AUC	area under the curve
BPE	bovine pituitary extract
BSA	bovine serum albumin
CAF	cancer-associated fibroblasts
CDKN2A	cyclin-dependent kinase inhibitor 2A
cDNA	complementary deoxyribonucleic acid
CK19	cytokeratin 19
CTC	circulating tumor cell
ddPCR	digital droplet polymerase chain reaction
DHM	digital holographic microscopy
DMEM	Dulbecco´s modified Eagle medium
DMSO	dimethylsulfoxide
DNA	deoxyribonucleic acid
ECM	extracellular matrix
EDTA	ethylenediaminetetraacetic acid
EGF(R)	epidermal growth factor (receptor)

EMT	epithelial-to-mesenchymal transition
ERK	extracellular signal-related kinase
EtOH	ethanol
FBS	fetal bovine serum
FDR	false discovery rate
FFX	folinic acid, fluorouracil, irinotecan, oxaliplatin (FOLFIRINOX)
Gem/nP	gemcitabine plus nab-paclitaxel
GES	gene expression signature
GSEA	gene set enrichment analysis
HE	hematoxylin/eosin
HIF1A	hypoxia-inducible factor 1A
HPDEC	human pancreatic ductal epithelial cell
IF	immunofluorescence
IFN-γ	interferon-γ
IHC	immunohistochemistry
IL	interleukin
Indel	insertion/deletion
IPMN	intraductal papillary mucinous neoplasm
IT	injection time
Kras	v-Ki-ras2 Kirsten rat sarcoma viral oncogene homolog
$KRAS^{Ba}$	balanced KRAS
$KRAS^{Ma}$	major KRAS imbalance
$KRAS^{Mi}$	minor KRAS imbalance
k-NN	k-nearest neighbor
MAPK	mitogen-activated protein kinase
MCN	mucinous cystic neoplasm
mTOR	mammalian target of rapamycin
MTT	3-(4,5-dimethyl-2-thiazolyl)-2,5-diphenyl-tetrazolium bromide

NES	normalized enrichment score
NMF	non-negative matrix fractorization
NN	neural network
OS	overall survival
OXPHOS	oxidative phosphorylation
PAGE	polyacrylamide gel electrophoresis
PanIN	pancreatic intraepithelial neoplasia
PBS	phosphate buffered saline
PBST	phosphate buffered saline tween-20
p120ctn	p120-catenin
PCR	polymerase chain reaction
PDAC	pancreatic ductal adenocarcinoma
PDC	pancreatic ductal cell
PDO	patient-derived organoid
PI3K	phosphoinositide 3-kinase
P/S	penicillin/streptomycin
PSC	pancreatic stellate cell
PurIST	purity independent subtyping of tumors
PVP	polyvinylpyrrolidone
ResNet	residual neural networks
RF	random forest
RNA	ribonucleic
ROS	reactive oxygen species
RT	room temperature
RT-qPCR	real-time quantitative polymerase chain reaction
scRNAseq	single cell RNA sequencing
SEM	standard error of mean
SDS	sodium dodecyl sulphate

Snail1	zinc finger protein Snai1
SNV	single nucleotide variants
ssEMT score	single sample epithelial-to-mesenchymal score
STI	soy trypsin inhibitor
SVM	support vector machines
TAE	tris-acetate-EDTA
TEMED	N, N, N', N'-tetramethylethylenediamine, 1,2-bis(dimethylamino)-ethane
TGF-β	transforming growth factor-β
TME	tumor microenvironment
TMT	tandem mass tag
TNFA	tumor necrosis factor-α
UMAP	uniform manifold approximation and projection
UMI	unique molecular identifier
WO	wash out
WT	wild type
Zeb1	zinc Finger E-Box Binding Homeobox 1

Abbreviations according to the international standardization system (SI units) are not included.

1. Abstract

Pancreatic ductal adenocarcinoma (PDAC) remains a devastating cancer entity with very poor survival rates. Combinational chemotherapy regimens such as FOLFIRINOX (FFX) or Gemcitabine plus nab-Paclitaxel (Gem/nP) prolong life only for a few months as patients often rapidly acquire resistance towards treatment. This resistance is largely driven by intratumoral heterogeneity due to clonal diversity and tumor cell plasticity. However, a detailed molecular characterization of resistance mechanisms and the identification of treatment-induced vulnerabilities and dynamic changes in phenotype and heterogeneity upon FFX and Gem/nP are mainly lacking, as scaleable and time-efficient single cell technologies barely exist.

Therefore, we established digital holographic microscopy (DHM) as a label-free high-throughput tool for investigating cellular heterogeneity in PDAC on a single cell level in real-time. We set up a robust experimental and machine learning analysis pipeline including feature extraction and pixel-based classification to perform single cell phenotyping based on DHM phase images of PDAC cells in suspension. This platform enabled us to monitor treatment-induced changes in cellular morphology on a single cell level allowing to asses particularly intratumoral heterogeneity. In addition, the molecular characterization of chemotherapy-induced adaptations in PDAC cells by genomic, transcriptomic and proteomic analysis gave insight into subtype-specific resistance mechanisms. Furthermore, we implemented a longitudinal precision oncology platform with a multi-dimensional characterization of matching patient-derived organoids before and after neoadjuvant FFX. Although cells isolated pre and post FFX did not significantly differ in PDAC subtype and their genomic landscape, unbiased drug screening identified FFX-induced vulnerabilities such as sensitivity towards MEK inhibition.

In sum, integrating functional layers such as DHM analysis and unbiased drug screening into precision oncology allows us to retrieve more detailed information about adaptive processes in tumor evolution and treatment-imposed pressure in PDAC than genomic and transcriptomic analysis alone. This information can be used in future to overcome this defined mode of resistance, guide treatment decisions and longitudinally monitor treatment response.

2. Zusammenfassung

Das duktale Adenokarzinom der Bauchspeicheldrüse (PDAC) ist nach wie vor eine verheerende Krebsart mit sehr schlechten Überlebensraten. Kombinierte Chemotherapieschemata wie FOLFIRINOX (FFX) oder Gemcitabin plus nab-Paclitaxel (Gem/nP) verlängern das Leben nur für wenige Monate, da die Patienten oft schnell eine Resistenz gegen die Behandlung entwickeln. Diese Resistenz wird weitgehend durch intratumorale Heterogenität aufgrund klonaler Diversität und Plastizität der Tumorzellen verursacht. Eine detaillierte molekulare Charakterisierung der Resistenzmechanismen und die Identifizierung behandlungsbedingter Schwachstellen und dynamischer Veränderungen des Phänotyps und der Heterogenität bei FFX und Gem/nP fehlen jedoch weitgehend, da skalierbare und kosteneffiziente Einzelzelltechnologien kaum existieren.

Daher haben wir die digitale holographische Mikroskopie (DHM) als markierungsfreies Hochdurchsatzinstrument zur Untersuchung der zellulären Heterogenität in PDAC auf Einzelzellebene in Echtzeit etabliert. Wir haben eine robuste experimentelle und maschinelle Lernanalyse-Pipeline mit Merkmalsextraktion und pixelbasierter Klassifizierung eingerichtet, um die Phänotypisierung einzelner Zellen auf der Grundlage von DHM-Phasenbildern von PDAC-Zellen in Suspension durchzuführen. Diese Plattform ermöglichte es uns, behandlungsbedingte Veränderungen der Zellmorphologie auf Einzelzellebene zu überwachen und insbesondere die intratumorale Heterogenität zu beurteilen. Darüber hinaus ermöglichte die molekulare Charakterisierung der Chemotherapie-induzierten Anpassungen in PDAC-Zellen durch genomische, transkriptomische und proteomische Analysen Einblicke in subtypspezifische Resistenzmechanismen. Zusätzlich haben wir eine longitudinale Präzisions-Onkologie-Plattform mit einer multidimensionalen Charakterisierung von Organoiden, die von einem Patienten vor und nach neoadjuvanter FFX stammen, implementiert. Obwohl sich die vor und nach der FFX-Behandlung isolierten Zellen hinsichtlich des PDAC-Subtyps und ihrer genomischen Landschaft nicht signifikant unterschieden, identifizierte das automatisierte Wirkstoffscreening FFX-induzierte Schwachstellen wie die Empfindlichkeit gegenüber MEK-Inhibition.

Zusammenfassend lässt sich sagen, dass die Integration funktioneller Schichten wie der DHM-Analyse und des automatisierten Wirkstoffscreenings in die Präzisionsonkologie es uns ermöglicht, detailliertere Informationen über adaptive Prozesse in der Tumorevolution und behandlungsbedingten Druck bei PDAC zu erhalten als Genom- und Transkriptomanalysen allein. Diese Informationen können in Zukunft genutzt werden, um diese definierte Art der Resistenz zu überwinden, Behandlungsentscheidungen zu treffen und das Ansprechen auf die Behandlung zu überwachen.

3. Introduction

3.1 Pancreatic ductal adenocarcinoma (PDAC)

Pancreatic ductal adenocarcinoma (PDAC) makes up 90% of all cases of pancreatic cancer and is the most common malignancy of the pancreas. Despite a low incidence in comparison to other types of cancer, PDAC has a very poor patient outcome. The five-year survival rate of PDAC patients in the US in 2020 was 9%. When diagnosed at a distant stage with metastatic spread, only 3% of the patients survived five years after diagnosis (Siegel et al., 2020). By 2040, pancreatic cancer is projected to ascend from the fourth to the second rank of cancer-related deaths, while mortality rates of the leading causes of cancer deaths such as colorectal cancer are projected to decrease (Rahib et al., 2021). Scientifically established risk factors for pancreatic cancer encompass both genetic as well as modifiable components. The presence of even one hereditary hazard increases the risk for PDAC by around 80% and it is estimated that 10% of all PDAC cases are driven by hereditary disorders. Furthermore, extensive abuse of tobacco and alcohol as well as following an unhealthy diet, obesity and diabetes are the most important modifiable risk factors (Becker et al., 2014). Once developed, PDAC is curable only by a complete surgical removal of the tumor. However, a majority of the patients are diagnosed at a metastatic stage due to the lack of visible and distinctive symptoms as well as reliable biomarkers. Thus, less than 20% of PDAC patients are eligible for surgical resection and those who received surgical resection frequently relapse often due to microscopic residual disease and chemotherapy-imposed pressure (Adamska et al., 2017; Hishinuma et al., 2006; Rahib et al., 2014; Rhim et al., 2012; Sakamoto et al., 2020).

3.1.1 PDAC progression model

In the pancreas, the progression to invasive carcinoma is accompanied by precursor lesions showing architectural as well as cytological abnormalities (Hruban et al., 2001). Three common precursors have been described: pancreatic intraepithelial neoplasia (PanIN), intraductal papillary mucinous neoplasm (IPMN) and mucinous cystic neoplasm (MCN). However, the best-characterized PDAC progression model is based on PanINs, which can be further classified into four groups. Early lesions, which are characterized by elongation of ductal cells with abundant mucin production are grouped into PanIN-1A when showing flat epithelial lesions, or PanIN1B, when already shaped papillary. In high-grade lesions, the presence of nuclear abnormalities such as loss of polarity, enlarged nuclei or nuclear crowding is classified as PanIN-2, while in PanIN-3 lesions additionally luminal necrosis, abnormal mitoses and dystrophy of goblet cells occur. In contrast, IPMNs involve the main pancreatic duct or major branches of the pancreas while in MCNs an ovarian-like stroma exists and the connection to

the duct system is absent. However, the larger size of both the IPMNs and MCNs enables their visualization and allows the discrimination from the microscopic PanINs, which are far too small to be imaged by current devices (Hruban et al., 2007).

All the above-mentioned morphological changes in PanINs are associated with distinct genetic alterations leading to the development of intraductal and invasive carcinoma. Recent genome as well as exome sequencing studies revealed activating mutations of *v-Ki-ras2 Kirsten rat sarcoma viral oncogene homolog (KRAS)* in more than 90% of low- and high-grade PanINs identifying the oncogene as a major genetic hallmark in PDAC leading to cancer initiation. Although most PanINs harbor mutations in *KRAS*, only a small percentage of all cells comprising a lesion is mutated. This percentage dramatically increases with the PanIN grade (Biankin et al., 2012; Kanda et al., 2012). Furthermore, inactivating mutations of the tumor suppressor gene *cyclin-dependent kinase inhibitor 2A* (*CDKN2A*), which encodes for the INK family member p16 and p14arf, occur already in early PanIN lesions. Additional mutations, which inactivate the tumor suppressor genes *TP53* and *SMAD4*, are shown to further drive PanIN progression (Kanda et al., 2012). Besides these well-validated mutations, germline alterations in DNA damage repair genes such as *BRCA1*, *BRCA2*, *PALB2* and *ATM* as well as mutations in the chromatin modifiers *EPC1* and *ARID2* give rise to genomic instability in a subset of pancreatic cancers (Bailey et al., 2016; Biankin et al., 2012; Jones et al., 2009; Roberts et al., 2016).

Recently, Mueller et al. identified evolutionary trajectories of murine PDAC involving different genetic hallmarks as well as variation in oncogene activation, that influencing the metastatic potential, cellular phenotype and tumor histology (Mueller et al., 2018). A major route of this trajectory has been described as beginning with a heterozygous *Kras* mutation and followed by a homozygous loss of *Cdkn2a* or *Tp53*. This in turn leads to an increase of mutant *Kras* dosage resulting in enhanced metastatic spread as well as more aggressive tumor phenotypes with mesenchymal cellularity and undifferentiated tumor histology.

Likewise, Chan-Seng-Yue et al. evaluated the genomic instability of 317 primary as well as metastatic PDAC samples of patients with a special focus on the *KRAS* gene, as well. They found the major *KRAS* imbalance (*KRAS*^{Ma}), favoring mutant *KRAS* allele, to be stage-dependent, since it was almost exclusively present in metastasis. Furthermore, *KRAS*^{Ma} was more frequently found in aggressive PDAC subtypes, similar to the results of Mueller and colleagues. Aggressive subtypes of the primary tumor exhibited mainly minor *KRAS* imbalances (*KRAS*^{Mi}). They additionally were able to correlate the *KRAS* status to existing clinical data and found a higher chemoresistance as well as worse patient outcome in the *KRAS*^{Ma} compared to *KRAS*^{Mi} or balanced *KRAS* (*KRAS*^{Ba}) subgroups (Chan-Seng-Yue et al., 2020).

3.1.2 Current treatment options in PDAC

Gemcitabine was used as standard chemotherapeutic agent for many years (Burris et al., 1997). It is a prodrug taken up by nucleoside transporters and the phospho-activation inside the cell leads to various inhibitory effects on DNA synthesis (Baldwin et al., 1999; Plunkett et al., 1995). It mainly acts as a cystidine and is incorporated into the DNA chain leading to the termination of DNA polymerase activity. It furthermore blocks the ribonucleotide reductase and prevents the *de novo* synthesis of deoxyribonucleotides (Huang et al., 1991; Huang and Plunkett, 1995). However, Gemcitabine has been recently replaced in clinical routine by the combination treatments FOLFIRINOX (FFX) and Gemcitabine plus nab-Paclitaxel (Gem/nP).

FFX is a combination of the cytostatic agents Leucovorin, 5-Fluorouracil (5-FU), Irinotecan and Oxaliplatin. 5-FU is a pyrimidine antagonist and acts in a fashion similar to that of Gemcitabine by incorporating into the DNA and causing cell death (Longley et al., 2003). While Irinotecan is a topoisomerase inhibitor inducing replication arrest and lethal double-strand breaks, Oxaliplatin inhibits DNA synthesis and transcription due to cross-linking the DNA by binding to guanine and cytosine (Liu et al., 2000; Mathijssen et al., 2002; Raymond et al., 1998). Leucovorin is a folinic acid used to reduce the toxic side effects of chemotherapies. It additionally stabilizes the active form of 5-FU to thymidylate synthase and enhances its activity. The combination of these drugs has shown a significant survival advantage in patients with metastatic cancer compared to the standard treatment gemcitabine alone. However, the median prolongation of life for only approximately 4.3 months is still frustrating (Conroy et al., 2011). Additionally, they could show a significantly increased disease-free survival upon adjuvant modified FFX (21.6 months) compared to gemcitabine (12.8 months) in patients with resected cancer (Conroy et al., 2018).

In another recent trial, a treatment regimen of nab-Paclitaxel in combination with Gemcitabine was tested for efficacy in increasing overall survival (Von Hoff et al., 2013). Paclitaxel is the active substance in nab-Paclitaxel and acts as an anti-microtubule agent interfering with the microtubule rearrangement by binding to α-tubulin. This in turn blocks the spindle apparatus during cell division resulting in cell arrest and ultimately cell death (Abal et al., 2003). The nanoparticle albumin bound (nab) form of Paclitaxel in nab-Paclitaxel improves the pharmacokinetic of the drug and leads to an increased mechanism of action in the tumor instead of healthy tissue (Chuang et al., 2002; Desai et al., 2006). Although combining Gemcitabine with nab-Paclitaxel has led to an overall survival (OS) of 8.5 months compared to the 6.7 months in the Gemcitabine only group, the survival advantage of only 1.8 months clearly demonstrates the need for further research and improvement (Von Hoff et al., 2013).

In clinical daily routine, the treatment decision is mainly based on the age and performance status of the patient. Due to the unfavorable side effects of FFX and Gem/nP, their administration is restricted to patients under 75 years of age with good performance only, while in patients with poor health, Gemcitabine is the preferred option (Gourgou-Bourgade et al., 2013). Recently, several studies have compared the efficacy and patient outcome of both combination treatments in order to find the most effective one. For instance, Papneja et al. reported comparable efficacies of FFX and Gem/nP in 119 retrospectively analyzed patients. While progression-free survival was 6 months in the FFX group compared to 4 months in the Gem/nP group, OS of 9 months was identical in both groups (Papneja et al., 2019). Furthermore, Chan et al. examined clinical data from 1130 patients with unresectable locally advanced as well as metastatic PDAC treated from April 2015 to March 2017. Results showed a survival advantage upon FFX treatment with a median OS of 9.6 months, an increase from the 6.1 months in the Gem/nP group (Chan et al., 2020). Likewise, 363 metastatic PDAC patients treated at the Yale Smilow Cancer Hospital from 2011 to 2019 were retrospectively studied regarding comparative effectiveness of FFX and Gem/nP. While treatment with FFX prolonged life for 11.3 months, the median survival was 7.2 months in the Gem/nP group (Patel, 2020). Although these studies indicate a survival advantage upon FFX treatment compared to Gem/nP in advanced and metastatic PDAC, research on the characterization of these treatment regimens on a molecular level is still lacking.

Recently, molecular profiling is more frequently used to identify individual actionable targets for personalized medicine, as well. In the Know Your Tumor registry trial they have retrospectively analyzed the treatment response of targeted therapies versus unmatched treatment and found a tremendous effect of matched over unmatched therapies for patient survival. They have identified genetic alterations in the tumor such as the *breast cancer gene 1 and 2 (BRCA1/2)* and *BRAF* and treated patients with the matched therapies Olaparib and Trametinib plus Dabrafenib, respectively. However, only 26% of PDAC patients display actionable targets, which is why molecular profiling alone might not be sufficient to find effective treatment options (Pishvaian et al., 2020).

The efficacy of targeted therapies and personalized medicine is tested also *in vitro* using the organoid technology by generating patient-derived organoids (PDOs). For instance, Tiriac et al. generated numerous PDO lines and tested for different chemotherapeutic drugs and 21 targeted agents (Tiriac et al., 2018). They found high sensitivity towards different targeted therapies in chemoresistant PDOs such as the broad-spectrum kinase inhibitor or Afatinib in *ERBB2*-amplified PDOs. They furthermore generated drug-sensitivity signatures by correlating drug response with PDO transcriptomes and

compared for example Gemcitabine sensitivity signature with clinical data of patients treated with Gemcitabine. Indeed, enrichment of this signature was significantly correlated with better progression free survival (Tiriac et al., 2018). In a similar study, they correlated the PDO mutational status with drug response of 76 drugs as well, in order to find effective combinations with Gemcitabine. The strongest association was detected with the EGFR inhibitor Lapatinib in combination with Gemcitabine and found drug sensitivity to depend on the mutational status of *PIK3K1* and *MAP3K1* (Driehuis et al., 2019). In our group, in the past years we have also generated a living PDO biobank and we recently established a workflow to identify druggable genetic alterations rapidly after PDO isolation using cell-free DNA in PDO supernatants (Dantes et al., 2020). In order to functionalize the obtained molecular information, PDOs were then subjected to a pharmacotyping using several common chemotherapeutic agents, which revealed a high inter-PDO line heterogeneity similar to what was shown before (Dantes et al., 2020; Driehuis et al., 2019; Tiriac et al., 2018).

Characterizing the molecular makeup of the tumor, such as tumor subtype and differentiation, and particularly evaluating its functional relevance might help better stratify patients for a specific treatment option and can be used as decision guidance in clinical routine.

3.1.3 PDAC subtyping

In the past decade, evolving next-generation approaches such as genomics and transcriptomics have enabled an in-depth characterization of PDAC on a molecular level.

In 2011, Collisson et al. performed gene expression microarrays from resected PDAC specimens and conducted non-negative matrix fractorization (NMF) with consensus clustering identifying three different subtypes (Collisson et al., 2011). After developing a subtype-specific gene signature based on 62 genes, they were able to cluster the analyzed PDAC samples into a classical, quasi-mesenchymal and exocrine-like subtype. While the classical subtype is marked by an enhanced expression of epithelial and adhesion-associated genes, the quasi-mesenchymal subtype had a higher expression of genes associated with the mesenchyme. In contrast, the exocrine-like subtype showed an increased expression of tumor cell-derived digestive enzyme genes. Furthermore, they found the tumor subtype itself to be an independent predictor of survival. Individuals with a classical subtype showed a better prognosis compared to individuals with a quasi-mesenchymal subtype. Additionally, subtypes significantly correlated with tumor grade and differentiation. When performing *in vitro* drug screening, quasi-mesenchymal human PDAC cells exhibited a higher sensitivity towards

Gemcitabine administration compared to cells with a classical subtype, indicating a phenotype-specific response towards chemotherapy (Collisson et al., 2011).

Moffitt et al. performed in 2015 whole genome microarrays on 145 primary and 61 metastatic PDAC tumors using virtual microdissection (Moffitt et al., 2015). NMF and consensus clustering identified two stromal gene expression signatures – namely normal and activated. While the normal subtype showed an increased expression of smooth muscle actin (α-SMA) and Vimentin, the activated subtype showed increased expression of matrix metalloproteases as well as SPARC and WNT family members. Patients with the activated stroma subtype additionally had a worse median survival than patients with a normal subtype. They identified cancer-associated fibroblasts (CAFs) and not the tumor epithelium to be the origin of these stroma signatures. Furthermore, they identified the two tumor-specific subtypes – the classical and basal-like. When they compared their subtypes to the Collisson subtyping, they found high concordance in the gene list of the classical subtype, but detected the quasi-mesenchymal subtype to be a mixture of their basal-like and the stroma subtypes indicating a stromal contamination in the Collisson study. When analyzing survival of the patients, their subtypes significantly correlated with prognosis, showing an OS of 11 and 19 months in basal-like and classical subtypes, respectively. Interestingly, the response towards adjuvant chemotherapy was increased in individuals with the basal-like subtype exhibiting a hazard ratio of 0.38 compared to 0.76 with a classical subtype, again suggesting a subtype-specific response towards chemotherapy. Additionally, after comparing different individuals as well as including several metastatic sites, they detected high inter-tumoral but low intra-tumoral heterogeneity (Moffitt et al., 2015).

In 2016, Bailey et al. presented their work on integrated genomic as well as transcriptomic analysis of 456 pancreatic cancer tumors (Bailey et al., 2016). Unsupervised clustering of the RNA-Seq data revealed four subtypes: squamous, aberrantly differentiated endocrine exocrine (ADEX), pancreatic progenitor and immunogenic. These tumor subtypes were furthermore associated with tumor histology. The squamous subtype was associated with adenosquamous carcinomas, the pancreatic progenitor and immunogenic subtypes were associated with mucinous non-cystic and IPMN-driven carcinomas while the ADEX subtype was associated with rare acinar cell carcinomas. Transcriptional networks identified gene programs discriminating these four subtypes. The squamous group was characterized by processes such as inflammation, metabolic reprogramming, transforming growth factor β (TGF-β) signaling as well as epithelial-to-mesenchymal transition (EMT) and was found to be an independent prognostic factor for worse overall survival. While the pancreatic progenitor class showed increased expression of transcription factors, such as *PDX1*, involved in early stages of pancreatic development, the ADEX class was characterized by processes of later

development such as acinar and endocrine cell differentiation. Lastly, the immunogenic subtype showed a strong infiltration of immune cells with an upregulation of B cells as well as regulatory and cytotoxic T cell signaling. When comparing their data with the published classifiers, they found a strong overlap with the Collisson subtyping. The squamous, pancreatic progenitor and ADEX subtypes were equivalent to Collisson´s quasi-mesenchymal, classical and exocrine-like subtypes, respectively. Of note, the immunogenic subtype did not correlate with any subtype of the Collisson classification (Bailey et al., 2016).

Additionally, to investigate *KRAS* instability, Chan-Seng-Yue et al. performed PDAC subtyping as well (Chan-Seng-Yue et al., 2020). Based on four tumor-specific expression signatures they identified five PDAC subtypes – basal-like A, basal-like B, classical A, classical B and hybrid. Their subtypes matched with the previously published classifications, with an exception of the hybrid subtype. Classical subtypes were found mainly in early stage tumors while basal-like subtypes occurred rather in late stage disease. A further sub-classification of basal-like and classical revealed different response rates towards chemotherapy in basal-like A and B with the basal-like B subtype being highly chemoresistant. Furthermore, analyzing intra-tumoral heterogeneity by single cell RNA sequencing (scRNAseq) revealed an enrichment of both classical and basal-like signatures in the primary tumor, suggesting a co-existence of different tumor cell populations. Interestingly, when comparing a matched primary tumor and metastasis sample, they detected a phenotype switch from the hybrid (Moffitt: classical) to the basal-like subtype due to raising mutant *KRAS* copy numbers. This molecular switch was driven by the outgrowth of a minor subclone in the primary tumor. Moreover, they compared liver metastasis before and after Gem/nP treatment from another patient and again found a subtype switch – this time from basal-like B to classical A due to a reduction in genome doubling. Hence, a reduction of mutant *KRAS* from $KRAS^{Ma}$ to $KRAS^{Ba}$ resulted in a transcriptional phenotype switch from a highly aggressive to a less aggressive phenotype (Chan-Seng-Yue et al., 2020).

In recent studies, single cell profiling of tumor specimen and corresponding *in vitro* model systems such as PDOs identified in particular the tumor microenvironment (TME) as driver of tumor cell state and differentiation (Grunwald et al., 2021; Raghavan et al., 2021). For instance, they found paracrine factors such as interferon-γ (IFN-γ) secreted by CD8+ T cells to be enriched specifically in intermediate co-expressor PDAC cell states (classical and basal-like gene expression signatures) and single cell basal-like cells. Additionally, TGF-ß was the top differentially expressed gene in the PDAC cells of co-expressor and basal-like TMEs. Adding TGF-ß to the culture media induced a phenotype shift, which was accompanied by a differential response towards different drugs. While classical PDAC cells were more sensitive towards chemotherapeutics and drugs targeting DNA damage, basal-like cells were highly sensitive towards MAPK inhibitors (Raghavan et al., 2021). Grünwald et al. performed a deconvolution

of the TME in human PDAC specimen by combining histology-guided regional multiOMICs and PDO culture and identified two regional TME states, the deserted and reactive subTME. While the reactive subTME exhibited activated CAFs, an immune hot and T cell-inflamed phenotype as well as pro-proliferative features, the deserted subTME showed rather de-differentiated CAFs with immune cold and chemoprotective features. Interestingly, the presence of both subTMEs within one tumor were found in several PDAC patients proving again high levels of intratumoral heterogeneity. These differences in TME were driving fundamental differences in tumor cells, as well. PDAC cells surrounded by a reactive subTME showed an increased cell cycle progression and Myc signaling with squamous and poorly differentiated PDAC cells, whereas the deserted subTME induced increased metabolism including oxidative phosphorylation (OXPHOS) with well-polarized glands and well-differentiated PDAC cells (Grunwald et al., 2021).

Likewise, we could recently show that deleting the plasticity regulator *Prrx1* in CAFs induced enhanced CAF activation with an increased collagen production and immune cell infiltration of CD3/4/8+ T cells, B cells, macrophages and dendritic cells. This modification of the TME composition revealed significant impact also on tumor cell phenotype, tumor differentiation, dissemination as well as response towards chemotherapy (Feldmann et al., 2021).

All studies mentioned above but in particular single cell studies clearly demonstrate the extremely heterogeneous composition of PDAC tumors and the complex relationship between all cell populations present within the tumor including the TME suggesting the implementation of scaleable single cell technologies for clinical application.

3.1.4 Mechanisms involved in PDAC chemoresistance

The enormous inter- and intratumoral heterogeneity makes treating PDAC efficiently a major challenge. Additional resistance and escape mechanisms upon chemotherapeutic treatment frequently result in either progression or relapse, further contributing to the poor prognosis associated with PDAC. The tumor microenvironment (TME), EMT as well as metabolism are well-known factors driving chemoresistance in several cancer entities.

EMT – a phenotype switch towards a more aggressive mesenchymal morphology with changes in genome, transcriptome and proteome – is thought to be a major process in the primary as well as secondary resistance towards chemotherapy. For instance, silencing EMT-inducing transcription factors such as the *Zinc Finger E-Box Binding Homeobox 1* (*Zeb1*), *Twist-related protein 1* (*Twist1*) or *Zinc finger protein Snai1* (*Snail1*) led to increased sensitivity towards gemcitabine administration *in vitro* as well as *in vivo* due to an increased expression of the nucleoside transporters importing gemcitabine into the cell (Arumugam et al., 2009;

Zheng et al., 2015). In line with this experimental data, clinical data sets from Liu et al. and preliminary results from the COMPASS trial suggested the basal-like subtype to exhibit an increased resistance towards chemotherapy (Aung et al., 2018; Liu et al., 2017). However, Moffitt et al. indicated a trend towards a better response to adjuvant therapy in the patients with basal-like subtype (Moffitt et al., 2015). EMT can be induced tumor cell-intrinsically, but often extrinsic factors released from the TME, which makes up about 80% of the cellular compartment of the tumor, influence the phenotypic properties of tumor cells (Zeng et al., 2019).

The TME is composed of extracellular matrix (ECM), pancreatic stellate cells (PSCs), CAFs as well as different types of immune cells, all of which together has great impact on the response towards chemotherapy (Apte et al., 2015; Pothula et al., 2016). PDAC is a cancer entity extremely rich in ECM. The excessive ECM-production by PSCs and CAFs often leads to an imbalance between production and degradation of matrix components. This desmoplastic reaction results in an increased migration and invasion of tumor cells as well as chemoresistance due to limited drug access. Targeting the stroma in PDAC has shown controversial results in murine and human trials with less satisfactory effects in humans (Kindler et al., 2011; Kindler et al., 2010; Ko et al., 2016; Olive et al., 2009). Additionally, although depleting PSCs or CAFs could increase drug sensitivity, the stroma is likely to serve as a barrier and prevents tumor cells from invading and metastasizing (Liu et al., 2017). Furthermore, inflammation is a well-known hallmark of PDAC with an increased abundance of tumor-associated macrophages and myeloid-derived suppressor cells (Liu et al., 2017). For instance, tumor-associated macrophages were shown to limit the efficacy of chemotherapy by various mechanisms including blocking cytotoxic T cells, protecting cancer stem cells as well as altering the tumor vascularity and thereby inhibiting intra-tumoral drug access (Bruchard et al., 2013). They are additionally able to secrete cytidine deaminase, the enzyme known for metabolizing the active gemcitabine into its inactive form (Weizman et al., 2014).

Lastly, the altered energy metabolism of the tumor affects the response towards conventional chemotherapy, as well. Hypoxic conditions within the tumor are sensed via the transcription factor hypoxia-inducible factor 1A (HIF1A) leading to the expression of genes involved in several pathways such as glycolysis and cell proliferation (Wang et al., 1995). HIF1A was shown to correlate in PDAC with tumor size and worse prognosis (Kitada et al., 2003; Shibaji et al., 2003). Hypoxic tumor areas – tumor as well as stromal compartment – exhibit an increased glycolytic metabolism with an enhanced lactate secretion. The secreted lactate in turn is metabolized by surrounding tumor cells for sustaining their cell growth. Additionally, HIF1A was found to trigger EMT with reduced E-Cadherin and increased N-Cadherin expression in murine PDAC (Guillaumond et al., 2013; Guillaumond and Vasseur, 2013).

Daemen et al. subtyped in 2015 human PDAC cells according to their metabolic profile into glycolytic and lipogenic. These subtypes could further be correlated with the quasi-mesenchymal and epithelial phenotype, respectively. While epithelial PDAC cells use the glucose for the tricarboxylic acid cycle and *de novo* lipogenesis, quasi-mesenchymal PDAC cells use the glucose rather for glycolysis and lactate production (Daemen et al., 2015).

Both recent single cell studies on PDAC confirmed that these mentioned components might play an important role in chemoresistance as the transcriptional cell state, which can be driven by the TME, might be a determinant for the chemosensitivity or -resistance in single cell classical or basal PDAC cells, respectively (Raghavan et al., 2021). Furthermore, they observed an increased chemoresistance of PDOs cultured in CAF-conditioned media derived from deserted versus reactive subTME. This was in line with clinical data from patients with deserted subTME, who showed the least change in tumor size after first-line chemotherapy (Grunwald et al., 2021).

These single cell studies give more detailed insight into resistance mechanisms than studies using solely bulk technologies, as the majority of PDAC patients display high levels of intratumoral heterogeneity allowing to identify single cell resistance mechanisms. Therefore, the necessity arises to establish scaleable and clinically easy-to-implement single cell technologies to retrieve information about tumor cell state and inter- as well as intratumoral heterogeneity for guidance of treatment decision and therapy monitoring.

3.2 Digital holographic microscopy (DHM)

Brightfield microscopy offers an easy way for the visualization of samples without major adjustments needed. However, due to the low contrast properties, it is not possible to differentiate single cells from each other. Thus, new imaging techniques have been developed in the past years, with a special focus on three-dimensional (3D) biological imaging. Digital holographic microscopy (DHM) is one of these approaches enabling label-free high-precision quantitative phase-contrast imaging (Molder et al., 2008). This technology harbors great potential for the application in translational PDAC research as this approach is solely based on cellular phenotypes and is independent of the expression of certain markers allowing an unbiased and standardized analysis. Additionally, the DHM is capable of visualizing single cells, thereby enabling to investigate single cell plasticity and intratumoral heterogeneity and finally allowing to understand the complex single cell composition of the tumor.

3.2.1 DHM setup

The basic setup of a DHM includes an illumination source, an interferometer with microscopic imaging optics, a digitizing camera as well as the corresponding computer software. The operation principle is based on the detection of an optical path-length delay caused by the transparent unstained specimen against the surrounding medium. This optical path-length delay is used to assess the refractive index, which correlates with sample density and thus its intracellular structures. Once the light beam, which does not pass the object, interferes with the light beam passing the object, the interfering beams are recorded and quantitative phase information is reassembled from the recorded hologram. This phase-contrast created by the differences in the refractive index at internal structures, provides abundant intracellular information (El-Schich et al., 2018).

Compared to standard DHM setups, coupling the DHM to an additional microfluidic system allows to analyze the cells not in an adherent condition but in a single cell suspension in a high-throughput manner. In our construct, the sample flows through a microchannel with the following dimensions: 50µM x 500 µM x 50.000 µM. Due to the combination of multiple laminar flows, the top and bottom flows as well as two side flows, the sample flow is kept in a steady focus and autofocusing procedures are eliminated (Ugele et al., 2018a; Ugele et al., 2018b).

Hence, this customized DHM setup gives access to reliable and detailed quantitative phase information about the intracellular structures without prior staining and labeling procedures. Additionally, combining DHM with a microfluidic system allows to analyze samples in a high-throughput manner.

3.2.3 DHM applications in cancer research

Due to the above-mentioned advantages of the DHM, lately it is applied more frequently in biological and medical research fields. Many studies have already obtained clinically relevant information about several types of cancer cells by using DHM. For instance, platinum-resistant and -sensitive endometrial cancer cells were separated from each other by their respective cell height and cell projected area obtained by DHM (Yao et al., 2019). Similarly, drug-resistant ovarian cancer cells could be differentiated from their sensitive parental controls using DHM (Singh et al., 2017). Since triple-negative breast cancer cells often do not express EpCAM or do so in very low amounts, the analysis of circulating tumor cells (CTCs) via EpCAM staining is not the appropriate approach. For this reason, El-Schich et al. used DHM to discriminate six different breast cancer cell lines from the white blood cells THP-1 and Jurkat comparing cell area, cell volume and cell thickness (El-Schich et al., 2020). Furthermore, the metastatic potential – the extent of EMT – of PDAC cells has been determined via DHM, as well. The metastatic potential was negatively correlated with cell thickness, but positively correlated with cell elongation – in concordance with the mesenchymal morphology of tumor cells (Kastl et al., 2019). Also, Colin et al. suggested the implementation of the quantitative phase information for detecting optical biomarkers for the metastatic potential of cancer cells (Calin et al., 2017). Additionally, breast cancer cells were graded on their morphological features using DHM and machine learning algorithms. Using linear support vector machines yielded best results in the separation of epithelial MCF-7 and mesenchymal MDA-MB-231 breast cancer cells (Lam et al., 2020). Min et al. performed DHM in a flow cytometry arrangement in order to measure single PDAC cells in flow. By this, they were able to differentiate epithelial PatuS and quasi-mesenchymal PatuT cells. They furthermore identified both populations in a mixed sample using DHM (Min et al., 2019).

These results clearly illustrate the sensitivity of the phase signatures generated by DHM for characterizing tumor cells in various conditions due to the capability of detecting the smallest changes in their cellular features.

3.3 Objectives

Our major aim of this project was to elucidate treatment-imposed pressure of PDAC cells upon the standard chemotherapeutic regimens FFX and Gem/nP. For that reason, we used functional model systems such as PDOs and DHM as new phenotyping tool in order to define treatment-induced phenotypic changes and understand mechanisms of chemoresistance as well as acquired vulnerabilities.

First, we established DHM as a label-free tool for the high-throughput characterization of PDAC phenotypes on a single cell level. After implementing the workflow comprised of sample preparation, DHM measurement following computational analysis, we clustered numerous human and murine PDAC cells according to their cellular morphology and transcriptomic profile. Importantly, we analyzed the single cell EMT status of each cell line allowing to investigate inter- and particularly intratumoral heterogeneity in a label-free fashion. Additionally, DHM enabled to detect dynamic changes in tumor cell differentiation and heterogeneity of distinct PDAC subtypes upon induction of epithelial-to-mesenchymal transition and under treatment-imposed pressure in murine and patient-derived model systems.

After implementing DHM as novel tool to asses heterogeneity, we exposed PDAC cells with different phenotypes to FFX and Gem/nP in order to investigate phenotype-specific response rates. For detecting possible resistance mechanisms occurring during or after treatment, we performed deep molecular analysis including proteomics and RNA-sequencing of cells treated with either drug combination. In the same experimental setup, we used the DHM pipeline to identify morphological changes upon chemotherapeutic treatment on a single cell level. Additionally, we established a longitudinal precision oncology platform to compare two PDAC specimen of a patient pre and post FFX treatment to translate the knowledge about treatment-induced vulnerabilities generated by *in vitro* studies into clinics.

4. Materials

4.1 Consumables

Table 1. Consumables used in this study.

Consumables	Source
Cell scrapers, 16cm	Sarstedt AG & Co., Nürnbrecht
Cellstar Aspiration Pipette 2ml	Greiner Bio-One, Kremsmünster, AU
Cellstar Stripette 5ml	Greiner Bio-One, Kremsmünster, AU
Cellstar Stripette 10ml	Greiner Bio-One, Kremsmünster, AU
Cellstar Stripette 25ml	Greiner Bio-One, Kremsmünster, AU
Cryogenic Vial 2ml	Corning Inc., NY, USA
Cellstar Tubes 15ml, 50ml	Greiner Bio-One, Kremsmünster, AU
Cellstar cell culture flask 75cm^2	Greiner Bio-One, Kremsmünster, AU
Coverslips	Menzel-Gläser, Braunschweig, Germany
Combitips BioPur®, 0.5 mL, 1mL, 5 mL, 10 mL	Eppendorf AG, Hamburg
Conical tubes, 15 mL	Greiner Bio-one GmbH, Frickenhausen
Conical tubes, 50 mL	Greiner Bio-one GmbH, Frickenhausen
CryoPure tubes	Sarstedt AG & Co., Nümbrecht
Disposable scalpels	Feather Safety Razor Co., Ltd., Osaka, Japan
EASYstrainer, 100µm	Greiner Bio-One, Kremsmünster, AU
Falcon Tissue Culture Plate 24-well	Corning Inc., NY, USA
Ibidi µ-Slide 2 well, 8 well	Ibidi GmbH, Gräfelfing
MicroAmp® optical 96-well reaction plate	Applied Biosystems, Inc., Carlsbad, CA, USA
MicroAmp Optical Adhesive Film	Thermo Fischer, Waltham, MA, USA
Micro Slides, frosted end	Assistent, Sondheim vor der Rhön
Nitrocellulose Membrane, 3 mm	GE Healthcare Europe GmbH, Munich
Parafilm®	Merck, Darmstadt
Pasteur pipettes	Hirschmann Laborgeräte GmbH & Co. KG,Eberstadt
PCR reaction tubes	Brand GmbH + Co. KG, Wertheim; Eppendorf AG, Hamburg
Petri dishes	Sarstedt AG & Co., Nümbrecht
Pipette tips	Sarstedt AG & Co., Nümbrecht

Reaction tubes, 0.5 mL, 1.5 mL and 2 mL	Eppendorf AG, Hamburg
Safe seal pipette tips, professional	Biozym Scientific GmbH, Hessisch Oldenburg
Safe-lock reaction tubes BioPur®	Eppendorf AG, Hamburg
Single use needles Sterican® 27 gauge	B. Braun Melsungen AG, Melsungen
Single use syringes Omnifix®	B. Braun Melsungen AG, Melsungen
SteriFlip Vacuum Filtration System 0.22µm	Merck Millipore, Burlington, USA
Transfer membrane Immobilon-FL	Millipore GmbH, Schwalbach am Taunus
Blotting Paper	Whatman, Dassel, Germany
Microscope slides	Carl Roth GmbH, Karlsruhe, Germany
Serological pipette, 2ml, 5ml, 10ml, 25ml	Greiner Bio-one GmbH, Solingen,
Tissue culture plate, 6, 94 well	BD Bioscience, Heidelberg

4.2 Equipment

Table 2. Equipment used in this study.

Consumables	**Source**
Analytical balance A 1200 S	Sartorius AG, Göttingen
Analytical balance BP 610	Sartorius AG, Göttingen
Autoclave 2540 EL	Tuttnauer Europe B.V., Breda, The Netherlands
AxioCam HRc	Carl Zeiss AG, Oberkochen
AxioCam MRc	Carl Zeiss AG, Oberkochen
Bag sealer Folio FS 3602	Severin Elektrogeräte GmbH, Sundern
Biometra Compact Agarose Gel Eletrophorsis	Analytik Jena, Jena
Brand Neubauer Improved	Brand GmbH, Wertheim
Centrifuge Avanti® J25	Beckman Coulter GmbH, Krefeld
Centrifuge Rotina 46R	Andreas Hettich GmbH & Co. KG, Tuttlingen
Centrifuge Rotina 380	Andreas Hettich GmbH & Co. KG, Tuttlingen

CO2 incubator HERAcell 240	Thermo Fisher Scientific, Inc., Waltham, MA, USA
Countess II FI	Life Technologies, Waltham, MA, USA
Dewar carrying flask, type B	KGW-Isotherm, Karlsruhe
Digital holographic microscope	Ovizio, Brussels, Belgium
Drying Cabinet Memmert type II 96	Memmert GmbH, Schwabach
EcoVac	Schuett Biotec GmbH, Göttingen
Electrophoresis Power Supply Model 100/500	Bio-Rad Laboratories GmbH, Munich
Electrophoresis Power Supply Model	Life Technologies Waltham, MA, USA
Electrophoresis power supply Power Pac 200	Bio-Rad Laboratories GmbH, Munich
FLUOstar OPTIMA microplate reader	BMG Labtech GmbH, Ortenberg
Gel DocTM XR+ system	Bio-Rad Laboratories GmbH, Munich
GentleMACS™ Dissociator	Miltenyi Biotec B.V. & Co. KG, Bergisch Gladbach
Glass ware, Schott Duran®	Schott AG, Mainz
HERAsafe® biological safety cabinet	Thermo Fisher Scientific, Inc., Waltham, MA, USA
Homogenizer SilentCrusher M with tool 6F	Heidolph Instruments GmbH & Co. KG, Schwabach
Horizontal gel electrophoresis system	Biozym Scientific GmbH, Hessisch Oldenburg
Horizontal shaker	Titertek Instruments, Inc., Huntsville, USA
Immunostainer Bond RXm	Leica, Wetzlar
Incubator shaker Thermoshake	C. Gerhardt GmbH & Co. KG, Königswinter
Laminar Flow type HS 18/2	Heraeus Instruments, Hanau
Leica Bond RXm	Leica, Wetzlar
Leica TCS SP8 Confocal Microscope	Leica, Wetzlar
Magnetic stirrer, Ikamag® RCT	IKA® Werke GmbH & Co. KG, Staufen
Microcentrifuge 5415 D	Eppendorf AG, Hamburg
Microcentrifuge 5417 R	Eppendorf AG, Hamburg
Microscope Axio Imager.A1	Carl Zeiss AG, Oberkochen
Microscope Axiovert 25	Carl Zeiss AG, Oberkochen

Microspoce Camera Axiocam MRC	Carl Zeiss AG, Oberkochen
Microwave	Siemens AG, Munich
Minicentrifuge MCF-2360	LMS Consult GmbH & Co. KG, Brigachtal
Multipette® stream	Eppendorf AG, Hamburg
Multiscan FC	Thermo Fisher Scientific, Waltham, MA, USA
Nanodrop	Thermo Fisher Scientific, Waltham, MA, USA
NextSeq 500	Illumina, San Diego, USA
Odyssey® infrared imaging system	Li-Cor Biosciences, Lincoln, NE, USA
pH meter FiveEasy	Mettler-Toledo, Greifensee, Switzerland
Pipettes Reference®, Research®	Eppendorf AG, Hamburg
Pipetus®	Hirschmann Laborgeräte GmbH & Co. KG, Eberstadt
Power supplies E844, E822, EV243	Peqlab Biotechnologie GmbH, Erlangen
Qubit 2.0 fluorometer	Thermo Fisher Scientific, Inc., Waltham, MA, USA
QX200 ddPCR system	Bio-Rad Laboratories GmbH, Munich
Rotary Microtome Microm HM355S	Thermo Fisher Scientific, Inc., Waltham, MA, USA
Spectrophotometer NanoDrop 1000	Thermo Fisher Scientific, Inc., Waltham, MA, USA
StepOnePlusTM real time PCR system	Thermo Fisher Scientific, Inc., Waltham, MA, USA
Surgical instruments	Thermo Fisher Scientific, Inc., Waltham, MA, USA
Thermocycle FlexCycler	Analytik Jena, Jena
Tumbling Table WT 17	Biometra GmbH, Göttingen
UVsolo TS imaging System	Biometra Analytik Jena Company, Überlingen
Vortex Genius 3	IKA® Werke GmbH & Co. KG, Staufen
Water bath 1003	GFL (Gesellschaft für Labortechnik) mbH, Burgwedel
Western blot system Mini-PROTEAN Tetra System	Bio-Rad Laboratories GmbH, Munich
3T PET/MRI system	Siemens Healthcare, Erlangen

4.3 Chemicals and reagents

Table 3. Chemicals and reagents used in this study.

Chemicals and reagents	Source
2-Mercaptoethanol, 98%	Sigma-Aldrich Chemie GmbH, Munich
2-Propanol (isopropanol)	Carl Roth GmbH + Co.
3,3,5-Triiodo-L-thyronine	Sigma-Aldrich Chemie GmbH, Munich
3-(4,5-dimethyl-2-thiazolyl)-2,5-diphenyl-tetrazolium bromide (MTT)	Sigma-Aldrich Chemie GmbH, Munich
A83-01	STEMCELL Technologies, Vancouver, Canada
Acetic Acid, 2N	Carl Roth GmbH + Co. KG, Karlsruhe
ACK lysis buffer	Thermo Fisher Scientific Inc, Waltham, USA
Agarose	Sigma-Aldrich Chemie GmbH, Munich
ALLin RedTaq	HighQu GmbH, Kraichtal
Ammonium persulfate (APS)	Sigma-Aldrich Chemie GmbH, Munich
Antigen unmasking solution	Vector laboratories Inc., Burlingame, USA
Aqua-Poly/Mounting	Polysciences Inc., Pennsylvania, USA
Bovine Pituitary Extract	Sigma-Aldrich Chemie GmbH, Munich
Bovine serum albumin, fraction V	Sigma-Aldrich Chemie GmbH, Munich
Bradford reagent	Sigma-Aldrich Chemie GmbH, Munich
Cell Recovery Solution	Corning Inc., NY, USA
Cholera toxin	Sigma-Aldrich Chemie GmbH, Munich
Collagen Type I, rat tail	Corning Inc., NY, USA
Collagenase Type II	Invitrogen GmbH, Karlsruhe
Collagenase Type IV	Worthington Biochemical Corporation, Lakewood, USA
Complete, EDTA-free, protease inhibitor cocktail tablets	Roche Deutschland Holding GmbH, Grenzach-Wyhlen
ddPCR mutation assay: KRAS WT, G12D	Bio-Rad Laboratories GmbH, Munich
DAPI	Sigma-Aldrich Chemie GmbH, Munich
Dexamethasone	Sigma-Aldrich Chemie GmbH, Munich
D-Glucose	Sigma-Aldrich Chemie GmbH, Munich
Dimethylsulfoxide (DMSO)	Carl Roth GmbH + Co. KG, Karlsruhe

Dodecylsulfate Na-salt in pellets (SDS)	Serva Electrophoresis GmbH, Heidelberg
Donkey serum	Biozol Diagnostica Vertrieb GmbH, Eching
Doxycycline	Sigma-Aldrich Chemie GmbH, Munich
Dulbecco's modified eagle medium (DMEM), with L-Glutamine, high Glucose	Invitrogen GmbH, Karlsruhe
DMEM low Glucose	Invitrogen GmbH, Karlsruhe
DMEM/F-12	Invitrogen GmbH, Karlsruhe
Eosin	Waldeck GmbH & Co KG, Münster
Ethanol (70%, 80%, 96%, 100%)	Merck KGaA, Darmstadt
Ethylenediaminetetraacetic acid (EDTA)	Invitrogen GmbH, Karlsruhe
Fetal Bovine Serum (FBS)	Invitrogen GmbH, Karlsruhe
Glycerol	Sigma-Aldrich Chemie GmbH, Munich
Glycin Pufferan®	Carl Roth GmbH + Co. KG, Karlsruhe
Hematoxylin	Merck KGaA, Darmstadt
HEPES Pufferan®	Carl Roth GmbH + Co. KG, Karlsruhe
Hydrochloric acid (HCl)	Merck KGaA, Darmstadt
ITS+ premix	Corning Inc., NY, USA
Keratinocyte-SFM medium	Thermo Fisher Scientific Inc, Waltham, USA
Laemmli Sample buffer, 4x	Bio-Rad Laboratories GmbH, Munich
Magnesium chloride	Carl Roth GmbH + Co. KG, Karlsruhe
Matrigel, growth factor reduced	Corning Inc., NY, USA
Methanol	Merck KGaA, Darmstadt
Milk powder	Carl Roth GmbH + Co. KG, Karlsruhe
NaOH Lösung, 1N	Carl Roth GmbH + Co. KG, Karlsruhe
Nicotinamide	Sigma-Aldrich Chemie GmbH, Munich
Nu-Serum IV	Corning Inc., NY, USA
Paraformaldehyde (PFA) 16% w/v	Alfa Aesar, Massachusetts, USA
Penicillin/Streptomycin	Thermo Fisher Scientific Inc, Waltham, USA
Pertex Mountin media	Histolab, Askim, Norway
Phosphatase inhibitor mix I	Serva Electrophoresis GmbH, Heidelberg

Phosphate buffered saline (PBS), 1x, 10x	Thermo Fisher Scientific Inc, Waltham, USA
Polyethylene glycol 4000	Merck KGaA, Darmstadt
Polyvinylpyrrolidon (PVP)	Carl Roth GmbH + Co. KG, Karlsruhe
Precision Plus ProteinTM all blue standard	Bio-Rad Laboratories GmbH, Munich
Primocin	InvivoGen, San Diego, USA
Proteinase K, recombinant, PCR grade	Roche Deutschland Holding GmbH, Grenzach- Wyhlen
Recombinant human heregulin ß1	PeproTech Inc., New Jersey, USA
Recombinant human transforming growth factor ß1 (TGF-ß1)	PeproTech Inc., New Jersey, USA
Recombinant mouse epidermal growth factor (EGF)	R&D Systems, Minnesota, USA
RIPA buffer, 10x	Abcam, Cambridge, UK
RNase Zap™	Sigma-Aldrich Chemie GmbH, Munich
ROCK inhibitor Y-27632	Cayman Chemical, Ann Arbor, USA
Roswell Park Memorial Institute (RPMI) medium	Thermo Fisher Scientific Inc, Waltham, USA
Roti® Histofix 4%	Carl Roth GmbH + Co. KG, Karlsruhe
Roti® Histol	Carl Roth GmbH + Co. KG, Karlsruhe
Rotiphorese® gel 30	Carl Roth GmbH + Co. KG, Karlsruhe
Sodium acetate buffer solution	Sigma-Aldrich Chemie GmbH, Munich
Sodium chloride (NaCl)	Merck KGaA, Darmstadt
Sodium hydroxide solution (NaOH)	Merck KGaA, Darmstadt
Soy Trypsin Inhibitor (STI)	Thermo Fisher Scientific Inc, Waltham, USA
StainIN Green Nucleic Acid Stain	HighQu GmbH, Kraichtal
Sterile Water	B.Braun Melsungen AG, Melsungen
TEMED	Carl Roth GmbH + Co. KG, Karlsruhe
TRIS	Carl Roth GmbH + Co. KG, Karlsruhe
Triton® X-100	Merck KGaA, Darmstadt
Trypan Blue Stain 0.4%	Invitrogen GmbH, Karlsruhe

Trypsin-EDTA 0.5% (10x)	Thermo Fisher Scientific Inc, Waltham, USA
Tween® 20	Carl Roth GmbH + Co. KG, Karlsruhe

4.4 Kits

Table 4. Kits used in this study.

Kits	Source
Bond Polymer Refine Kit	Leica, Wetzlar
Nextera XT kit	Illumina, San Diego, USA
QIAamp® DNA Mini kit	Qiagen GmbH, Hilden
QIAshredder	Qiagen GmbH, Hilden
RNeasy mini kit	Qiagen GmbH, Hilden
RNeasy micro plus kit	Qiagen GmbH, Hilden
SensiFastTM cDNA Synthesis Kit	Bioline, London, UK
SensiFastTM SYBR Hi-Rox Kit	Bioline, London, UK
RNase-free DNase	Qiagen GmbH, Hilden
Senescence ß-Galactosidase Cell Staining kit	Signaling Technology, Massachusetts, USA
CellTiter-Glo Luminescent cell viability assay	Promega GmbH, Walldorf

4.5 Antibodies

Table 5. Antibodies used in this study.

Antibody	Dilution	Source
Phalloidin-Atto 647	1:250	Sigma-Aldrich Chemie GmbH, Munich
TROMA-III CK19	1:250	DSHB
aSMA	1:100	Cell Signaling Technology, Massachusetts, USA
Zeb1	1:100	Cell Signaling Technology, Massachusetts, USA
E-Cadherin	1:200	R&D Systems, Minnesota, USA
E-Cadherin	1:1000	Cell Signaling Technology, Massachusetts, USA
Vimentin	1:50	R&D Systems, Minnesota, USA

GATA 6	1:1000	Cell Signaling Technology, Massachusetts, USA
Ki67	1:50	Abcam, Cambridge, UK
Keratin 81	1:500	Santa Cruz Biotechnology, Dallas, USA
Phospho-p44/42 MAPK (pErk1/2)	1:1000	Cell Signaling Technology, Massachusetts, USA
p44/42 MAPK (Erk1/2)	1:1000	Cell Signaling Technology, Massachusetts, USA
GLUT1	1:750	Abcam, Cambridge, UK
donkey anti-goat AF488	1:250	Thermo Fisher Scientific Inc, Waltham, USA
donkey anti-rat AF594	1:250	Thermo Fisher Scientific Inc, Waltham, USA
donkey anti-rabbit AF680	1:250	Thermo Fisher Scientific Inc, Waltham, USA
donkey anti-mouse AF488	1:250	Thermo Fisher Scientific Inc, Waltham, USA
IRDye® 680RD Donkey anti-Rabbit IgG	1:10000	LI-COR Biosciences, Lincoln, USA
IRDye® 800CW Donkey anti-Rabbit IgG	1:10000	LI-COR Biosciences, Lincoln, USA
IRDye® 680RD Donkey anti-Mouse IgG	1:10000	LI-COR Biosciences, Lincoln, USA

4.6 Drugs

Table 6. Drugs used in this study.

Drug	Source
Irinotecan	Fresenius Kabi Deutschland GmbH, Bad Homburg
Oxaliplatin	Fresenius Kabi Deutschland GmbH, Bad Homburg
Fluorouracil	Medac GmbH, Wedel
Gemcitabine	Hexal AG, Holzkirchen
nab-Paclitaxel	Ratiopharm GmbH, Ulm
Poziotinib	SelleckChem, Houston, USA
Lapatinib	SelleckChem, Houston, USA
Binimetinib	SelleckChem, Houston, USA
Cobimetinib	SelleckChem, Houston, USA
PF-3758309	SelleckChem, Houston, USA
IACS-010759	SelleckChem, Houston, USA

4.7 Primers

Table 7. Primers used in this study.

Primer name	Sequence (5´ → 3´)
Quantitative real-time PCR	
mE-Cadherin Forward	5'-TCAAGCTCGCGGATAACCAGAACA-3'
mE-Cadherin Reverse	5'-ATTCCCGCCTTCATGCAGTTGTTG-3'
hE-Cadherin Forward	5'-GCCTCCTGAAAAGAGAGTGGAAG-3'
hE-Cadherin Reverse	5'-TGGCAGTGTCTCTCCAAATCCG-3'
hVimentin Forward	5'-AGGCAAAGCAGGAGTCCACTGA-3'
hVimentin Reverse	5'-ATCTGGCGTTCCAGGGACTCAT-3'
mN-Cadherin Forward	5'-ATGGCCTTTCAAACACAGCCACAG-3'
mN-Cadherin Reverse	5'-ACAATGACGTCCACCCTGTTCTCA-3'
mß-Actin Forward	5'-GTCGAGTCGCGTCCACC-3'
mß-Actin Reverse	5'-GTCATCCATGGCGAACTGGT-3'
hß-Actin Forward	5'-CACCATTGGCAATGAGCGGTTC-3'
hß-Actin Reverse	5'-AGGTCTTTGCGGATGTCCACGT-3'
Mycoplasm test	
5'Primer #1	CGCCTGAGTAGTACGTTCGC
5'Primer #2	CGCCTGAGTAGTACGTACGC
5'Primer #3	TGCCTGGGTAGTACATTCGC
5'Primer #4	TGCCTGAGTAGTACATTCGC
5'Primer #5	CGCCTGAGTAGTAGTCTCGC
5'Primer #6	CACCTGAGTAGTATGCTCGC
5'Primer #7	CGCCTGGGTAGTACATTCGC
3'Primer #1	GCGGTGTGTACAAGACCCGA
3'Primer #2	GCGGTGTGTACAAAACCCGA
3'Primer #3	GCGGTGTGTACAAACCCCGA

4.8 Molecular biology

Table 8. Buffers and solutions used for molecular biology.

Buffer	Composition
RIPA lysis buffer, pH 7.9	10x RIPA buffer
	ddH_20
	Phosphatase inhibitor (add prior use)
	Protease inhibitor (add prior use)

Stacking gel buffer, pH 6.8	0.5 M Tris, adjusted to pH 6.8 with HCl
Stacking gel buffer, pH 6.8	1.5 M Tris, adjusted to pH 8.8 with HCl
Running buffer	25 mM Tris 192 mM Glycine 0.1% SDS
Transfer buffer, pH 8.3	25 mM Tris 192 mM Glycine 20% Methanol/Ethanol
PBS-Tween (PBST)	1x PBS 0.1 % v/v Tween® 20
SDS lysis buffer	80 mM Tris, adjusted to pH 7.6 with HCl 4% SDS ddH_20
50x Tris acetate EDTA (TAE) buffer, pH 8.5	2 M Tris 50 mM EDTA 5.71% Acetic acid

4.9 Cell culture

Table 9. Media and buffers used for cell culture.

Media and buffers	Composition
Cancer cell media 1	DMEM 10% FBS 1% Penicillin/Streptomycin
Cancer cell media 2	RPMI 10% FBS 1% Penicillin/Streptomycin
Fibroblast media	50% DMEM low Glucose 50% DMEM/F12 20% FBS 1% Penicillin/Streptomycin
HPDEC media	Keratinocyte media 2.5 µg Human recombinant epidermal growth factor 25 mg Bovine pituitary extract
PDC media	DMEM/F12

	5% Nu-Serum IV 1% Penicillin/Streptomycin 25 µg/mL Bovine pituitary extract 0.5% ITS+ premix 20 ng/mL Epidermal Growth Factor 100 ng/mL Cholera toxin 5nM 3,3,5-Triiodo-L-thyronine 1 µM Dexamethasone 5 mg/mL D-Glucose 1.22 mg/mL Nicotinamide
Organoid media	DMEM/F12 5% Nu-Serum IV 1% Penicillin/Streptomycin 25 µg/mL Bovine pituitary extract 0.5% ITS+ premix 100 ng/mL Cholera toxin 5nM 3,3,5-Triiodo-L-thyronine 1 µM Dexamethasone 5 mg/mL Glucose 10 mM Nicotinamide 100 µg/mL Primocin 0.5µM A83-01 10% R-Spondin (self-produced) 100 ng/mL Neuregulin or 50 ng/mL WNT3A
Freezing media	90% FBS 10% DMSO
Freezing media (PDCs)	95% PDC media 5% DMSO
Digestion buffer (PDCs)	DMEM/F12 1.5 mg/mL Collagenase Type IV
Digestion buffer (human biopsies)	DMEM/F12 6 mg/mL Collagenase Type II

Table 10. Cell lines used in this study.

Cell line ID	Source
murine	
8442	Mueller et al., 2018
9591	Mueller et al., 2018
53631	Mueller et al., 2018
8028	Mueller et al., 2018
9091	Mueller et al., 2018
16992	Mueller et al., 2018
793 Y (p120+/+)	Reichert et al., 2018
363 Y (p120+/-)	Reichert et al., 2018
288 Y (p120-/-)	Reichert et al., 2018
human	
B361 (CAF)	Organoid core facility
HPDEC	RRID:CVCL_4376
ID188	Organoid core facility
ID211	Organoid core facility
ID203	Organoid core facility
ID208	Organoid core facility
ID226	Organoid core facility
ID250	Organoid core facility
PatuS	RRID: CVCL_1846
PatuT	RRID:CVCL_1847
DanG	RRID: CVCL_0243
HPAC	RRID:CVCL_3517
PSN-1	RRID:CVCL_1644

4.10 Software

Table 11. Software used in this study.

Software	Source
Adobe Photoshop 7.0	Adobe Systems Software Ireland Limited, Dublin, Ireland
Adobe Illustrator CS	Adobe Systems Software Ireland Limited, Dublin, Ireland
Ascent Software Version 2.6	Ascent Software, London, Great Britain
AxioVision 4.8	Carl Zeiss AG, Oberkochen
Microsoft Excel	Microsoft Corporation, Redmont, WA, USA
GraphPad Prism 8	La Jolla, CA, USA
Odyssey® v1.2	Li-Cor Biosciences, Lincoln, NE, USA
OsOne	Ovizio, Brussels, Belgium
OsiriX	OsiriX Foundation; Geneva, Switzerland
Perseus software 1.6.14.0	Max-Planck Institute of biochemistry, Munich
QuantaSoft droplet reader software	Bio-Rad Laboratories GmbH, Munich
Quantity One	Bio-Rad Laboratories GmbH, Munich
R studio 4.0.02, 4.0.04	R studio PBC, Boston, USA
StepOneTM v2.3	Applied Biosystems, Inc., Carlsbad, CA, USA
Fiji Version 1.0	LOCI, Madison, WI, USA
Textmaker	Free Software Foundation Boston, MA, USA

5 Methods

5.1 Clinical data

5.1.1 Patient recruitment

The study was conducted in accordance with the Declaration of Helsinki. Approval by the local ethics committee (Project 207/15, 1946/07, 330/19, 181/17S and 80/17S) was given and written informed consent was obtained from the patient prior to the investigation.

The following clinical data were obtained for the patient using the hospital's information system: sex, age at diagnosis, tumor markers CEA and CA 19-9, tumor formula, type of chemotherapy (neoadjuvant, adjuvant) and chemotherapeutic regime (FOLFIRINOX). Clinical evaluation of the tumor size, lymph node status and metastasis were performed on baseline CT before starting the treatment and in follow-up examinations.

5.1.2 Imaging protocol and analysis

Simultaneous 18F-FDG PET/MRI was performed using an integrated whole-body 3T PET/MRI system as previously described (Harder et al., 2021). The patient was instructed to fast for at least 6 hours before injection of 400 MBq (baseline) and 393 MBq (follow-up) 18F-FDG injection. In addition, 20 mg furosemide as well as oral contrast (Telebrix, 15ml on 1l) were applied. The PET/MRI scans were started 51 min (baseline) and 63 min (follow-up) after tracer injection.

PET/MRI examination of the pancreas was performed simultaneously within a 20-min PET scan of the upper abdomen. A T1-VIBE Dixon sequence was used for attenuation correction. Further MRI sequences included an axial and coronal T2 haste sequence, axial fat saturated (FS) T2 haste sequence, axial DWI (b-values 0, 50, 300 and 600 s/mm2), axial T1 VIBE Dixon sequence in breath-hold before and after dynamic administration of contrast agent (arterial, venous and late venous phase) with gadolinium (0,2 ml/kg bodyweight) and an axial T1 VIBE Dixon FS after contrast administration.

PET data were reconstructed using a vendor-provided iterative reconstruction algorithm (3 iterations, 21 subsets, image matrix 172 ×172, zoom 1, gauss filter, full width at half maximum 4.0 mm, relative scatter correction). Image analysis was performed by one radiologist with 3 years of experience (FNH) under supervision of a board certified expert abdominal radiologist with 10 years of experience (RFB) as well as a board certified expert nuclear medicine physician with 10 years of experience (ME).

Reviewing the axial T2w, DWI and ADC together with the PET images using OsiriX, the tumor localization was identified. The maximum as well as the peak standardized uptake values (SUVmax and SUVpeak; in g/ml) were obtained from the tumor (Harder et al., 2021).

5.2 Histological analysis

5.2.1 Paraffin-embedded sections

For histological analysis, tissue samples were fixed in 4% Roti® Histofix for 48 h and organoids were fixed in 4% PFA for 15min, dehydrated using the tissue processor ASP300, embedded in paraffin and stored at room temperature (RT) until further use. For following stainings, series of 2.5–3 µm thick serial sections were cut using the microtome Microm HM355S.

5.2.2 Hematoxylin and eosin (HE) staining

Paraffin-embedded sections were deparaffinized by incubation in xylol (2 x 5 min) and rehydrated in isopropanol, 96% and 70% EtOH for 2 x 5min each. After 25 s in water, slides were stained for 8 min with mayer´s hematoxylin and subsequently blued in running tab water for 10 min. Slides were then stained in eosin for 4 min and applied to 96% EtOH for 30 s, isopropanol for 2 x 25 s and xylol for 2 x 1.5 min before they were covered with mounting medium.

5.2.3 Immunohistochemical (IHC) staining

Immunohistochemistry (IHC) staining was performed at the Comparative Experimental Pathology Department at Klinikum rechts der Isar using a Leica Bond RXm system. Therefore, slides were briefly deparaffinized using a deparaffinization solution and epitope retrieval was performed using a citrate buffer with pH 6 or ETDA buffer with pH 9 for 20 – 40 min. The primary antibodies Ki67, GLUT1, pERK and ERK were diluted and applied for 15min. Antibody binding was detected using the polymer refine detection kit and visualized after 10 min of incubation with DAB as a dark brown precipitate. Counterstaining was performed using hematoxylin for 5 min. Dehydration was manually performed by alcohol washes with increasing concentrations (70%, 96% and 100%) and a final xylene incubation. Afterwards, slides were mounted with coverslips using Pertex mounting medium and scanned with 40x magnification.

Quantification was performed on five organoid images per condition and cell line using Fiji 2.1.1 (RRID:SCR_002285). Therefore, the plugin for color deconvolution was used to separately quantify the expression of Ki67, pERK as well as ERK and the hematoxylin staining.

Finally, the respective protein expression was normalized to hematoxylin in order to obtain relative expression levels.

5.3 Cell culture

5.3.1 Culturing of 2D cell lines

The different two-dimension (2D) cell lines were cultured in their respective medium and were maintained at 37°C and 5% CO_2. Murine PDAC cells as well as PatuS and PatuT were cultured in DMEM supplemented with 10% fetal bovine serum (FBS) and 1% penicillin/streptomycin (P/S), while DanG, HPAC and PSN-1 were cultured in RPMI plus 10% FBS and 1% P/S. Murine pancreatic ductal cells (PDCs) were cultured in the PDC medium (Reichert et al., 2013), while human pancreatic ductal epithelial cells (HPDECs) were maintained in Keratinocyte-SF media, which was enriched with human recombinant Epidermal Growth Factor 1-53 (EGF 1-53) and Bovine Pituitary Extract (BPE). Fibroblasts were cultivated in the fibroblast medium containing 50% DMEM-F12, 50% DMEM low Glucose, 20% FBS and 1% P/S.

For passaging PDAC cells and fibroblasts, medium was removed and cells were washed with PBS. Afterwards, 1-2mL of trypsin were added for 5-10min in order to detach the cells from the bottom of the flask. Trypsinization was stopped by adding new media and cells were distributed into new flasks or seeded for experiments.

For HPDECs, trypsinization was stopped using 4mL of Soybean Trypsin Inhibitor (STI) and an additional centrifugation step for 5min at 1000 rpm was performed to remove trypsin from the cells.

Murine PDCs were seeded onto collagen-coated plates (Table 12). For passaging, medium was carefully removed and the collagen layer containing the cells was collected in a reaction tube filled with filter sterilized digestion media and incubated for approximately 30min at 37°C. After the collagen was properly digested, cells were centrifuged at 1000 rpm for 5min and the pellet was resuspended in 1mL of trypsin. After 5min, trypsinization was stopped using 3mL of STI and washed by adding 5mL of PBS. Cells were centrifuged again and the cell pellet was resuspended in new PDC medium.

Table 12. Components used for collagen coating.

Components	Concentration
Collagen Type I, rat tail	2.31 mg/mL
10x PBS	10 %
1N NaOH	1.65%
ddH_2O	Adjust volume

For seeding a certain number of cells for an experiment, cell number was calculated using the Neubauer chamber.

Cells were thawed quickly to prevent cell damage. Then, cells were taken up with medium and transferred into a new flask. In order to remove DMSO present in freezing medium, medium was changed the next day.

For cryopreservation, cells were washed and trypsinized. Afterwards, they were centrifuged for 5 min at 1000 rpm and 4 °C and the supernatant was removed. The cell pellet was resuspended in 1 ml freezing medium per vial and quickly frozen in the -80 °C freezer.

5.3.2 Generation and culture of patient-derived organoids

Primary patient-derived PDAC 3D organoids (PDOs) were generated from endoscopic ultrasound-guided fine needle aspirations/biopsies (EUS-FNA/B) and surgical resections as it was described previously (Dantes et al., 2020). Briefly, biopsies were minced into small pieces and surgery specimen were incubated rotating for collagen digestion using a digestion buffer for 1-2 h. Tissue pellets were incubated for 3-10 min with red blood cell lysis buffer and afterwards further digested using TrypLE. Lastly, cell pellets were resuspended in 50 µl of Matrigel/well and PDO was added 10 min later.

For passaging, the media was aspirated and 250 µl of Cell Recovery Solution was added to each well for 5 min. Subsequently, this mixture was dissolved in 1 ml of ice-cold PBS supplemented with 0.1 % BSA. After 30 min on ice, organoids were centrifuged at 1000 rpm at 4°C for 5 minutes, washed and centrifuged again. Thereafter, cell pellets were resuspended in 50 µl Matrigel/well and medium was added 10 min later.

In order to make PDOs applicable to high-throughput drug screening using a liquid-handling robot, we generated 2D lines from PDOs using the outgrowth method. Briefly, after the establishment of 3D organoids from primary PDAC specimen, 2D cells were allowed to grow out from the Matrigel and attach to the plastic. Matrigel and organoids were removed and 2D cells were further cultured using RPMI medium supplemented with 10 % fetal bovine serum and 1 % penicillin/streptomycin. Passaging was performed as described in 5.3.1.

5.3.3 Pharmacotyping of murine PDAC cells

The 3-(4,5-dimethyl-2-thiazolyl)-2,5-diphenyl-tetrazolium bromide (MTT) assay was used to determine cell viability after drug administration by measuring the metabolic activity of the murine cells. Therefore, 1000 cells/well were seeded in a 96-well plate as triplicates. Cells

were incubated with 20 µl of the drugs, which were added the next day in a 7-point drug dilution for 72 h. For MTT measurement, 10 µl of MTT reagent were added per well and incubated for 4 h at 37 °C. Afterwards, cell media was removed and 200 µl of an EtOH-DMSO mixture, diluted 1:1, were added. After 15 min of shaking at room temperature (RT), the absorption was measured at a wavelength of 595 nm using the spectrophotometer Multiscan FC.

5.3.4 Pharmacotyping of patient-derived organoids

For pharmacotyping of human 3D cells, organoids were processed as described in 5.3 and digested to a single cell suspension using 1x trypsin. 500 cells/well were seeded in a total volume of 20 µl/well (2 µl Matrigel + 18 µl PDO media) in a 384-well plate. After 24 hours, drugs were added in a 7-point drug dilution to the cells (highest concentration = 10 µM) and incubated for 72 hours. In order to measure cell viability, the metabolic activity was determined by measuring ATP present. Therefore, 5µl of CellTiter-Glo® Luminescent Cell Viability reagent was added and incubated for 15 min shaking. Afterwards, luminescence was measured on a FLUOstar OPTIMA microplate reader (BMG Labtech GmbH).

5.3.5 Growth rate of patient-derived organoids

For investigating the growth rates of human 3D cells, organoids were processed as described in 5.3 and digested to a single cell suspension using 1x trypsin. 500 cells/well were seeded in a total volume of 20 µl/well (2 µl Matrigel + 18 µl PDO media) in a 384-well plate. Cell growth was determined for 5 consecutive days using 5 µL of the CellTiter-Glo® Luminescent Cell Viability reagent and values were normalized to the first day.

5.3.6 Automated drug screening

Automated drug screening of ID188 and ID211 2D cells was performed in the SFB1321 Core. Therefore, 1500-3000 cells per well (depending on growth rate) were seeded in 96-well plates using a Multidrop™ Combi Reagent Dispenser (Thermo Fisher Scientific). After overnight incubation at 37 °C and in 5 % CO_2 in a Cytomat™ 24C automated incubator (Thermo Fisher Scientific), cells were treated with a compound library using a CyBio® FeliX pipetting platform (Analytik Jena). All compounds were obtained from SelleckChem. Each drug was added in 7 concentrations (3-fold dilution series, highest concentration 10 µM). Cell viability was measured after 72 hours using CellTiter-Glo® Luminescent Cell Viability Assay (Promega). The reagent was added using a Multidrop™ Combi Reagent Dispenser (Thermo Fisher

Scientific). After incubation for 10 minutes luminescence was measured in an Infinite® 200 PRO microplate reader (Tecan). Drug response was analyzed using the R package GRmetrics (Clark et al., 2017; Hafner et al., 2016). The difference of the area under the curve (delta AUC) between ID188 and ID211 for each drug was calculated and a threshold of >0.3 and <-0.3 was set to identify top hits.

5.3.7 Senescence β-Galactosidase Staining

HPDECs were seeded in a 6 well plate and in order to activate the *Kras*^{G12D} mutation, cells were treated for 24h with 125 ng/mL doxycycline. For senescence β-Galactosidase staining, the Senescence β-Galactosidase Staining Kit was used according to manufacterer´s protocol. Briefly, cells were washed with PBS and fixed for 15min. The β-Galactosidase staining solution was incubated overnight at 37°C without CO_2. The development of blue color was analyzed by taking images with a brightfield microscope.

5.4 Molecular biology

5.4.1 Isolation of genomic DNA

Murine and human 2D cells were seeded in 10cm dishes and genomic DNA was harvested once they were 80% confluent. Therefore, media was removed, cells washed with PBS and collected using cell scrapers. Genomic DNA was isolated using the QIAamp® DNA Mini kit according to manufacturer´s protocol. DNA concentrations were measured using Nanodrop.

Organoids were processed to a cell pellet as described in 5.3.2 and genomic DNA was isolated from organoid lines (ID188 passage 7, ID211 passage 6) and blood as reference tissue using the AllPrep® DNA/RNA micro kit according to the manufacturer's instructions. DNA concentration was fluorimetrically determined using the Qubit 3.0 system.

5.4.2 Test for mycoplasm contamination

Before cryopreservation and after experiments, cells were tested for mycoplasm contamination. When cells were almost completely confluent, 2 ml of medium were taken and frozen at -20°C until further use. After thawing on ice, medium was centrifuged at 250 g for 2 min and supernatant was transferred into a new reaction tube. After centrifugation at 20000 g for 10 min, supernatant was discarded and pellet was resuspended in 50 µl PBS. 2 µl therefrom were used for polymerase chain reaction (PCR) according to Table 13. Agarose gel electrophoresis was performed as described in 5.2.3.

Table 13. Reaction mix and PCR conditions used for mycoplasm test.

Reaction mix		Conditions		
PCR-premix	15 µl	95 °C	15 min	
5'primer mix	2 µl	94 °C	1 min	
3'primer mix	2 µl	60 °C	1 min	40 x
distilled water	9 µl	74 °C	1 min	
templated	2 µl	72 °C	10 min	

5.4.3 Separation of DNA by agarose gel electrophoresis

For separating the DNA via agarose gel electrophoresis, 2% agarose gels were prepared. Therefore, 6-8 g agarose were dissolved in 400 ml 1xTAE buffer and heated for 7 min at maximal temperature. After 15 min of cooling, StainIN green nucleic acid stain were added according to the protocol and the gel chambers were filled with the mixture. When gels were polymerized, combs were loaded with 12 µl of PCR sample and electrophoresis was carried out at 120 V for 1-2 h.

5.4.4 Droplet digital polymerase chain reaction (ddPCR)

DNA of the three conditions, untreated, 72h FFX or Gem/nP and 72h wash out, was isolated and submitted for detection and absolute quantification of the *KRAS*^{G12D} mutation via ddPCR to the collaboration partners from the Department of Clinical Chemistry and Pathobiochemistry at Klinikum rechts der Isar.

The different components necessary for ddPCR were mixed as indicated (Table 14) and pipetted into a 96-well ddPCR plate. Reactions were carried out on a QX200 ddPCR system with automated droplet generation. Negative controls (murine pancreas tissue without Kras mutation), positive controls (gBlocks, synthetic DNA with amplicon sequence and KRAS mutation or KRAS wildtype) and no template controls (purified, nuclease-free water) were included. All samples were measured in duplicates.

After automatically generating 20.000 nanoliter-sized droplets per sample, 96-well plates were sealed and PCR was performed according to the cycling protocol for ddPCR (Table 15). Finally, the raw droplet fluorescence intensity of each droplet was analyzed individually by the QX200 droplet reader using a two-color detection system and the QuantaSoft droplet reader software. Custom R scripts were used to quantify the concentrations (c) of mutant and wildtype Kras.

Calculation was performed as follows:

c = (ln (Np + Nn) – ln (Nn)) / V

ln = natural logarithm

Np = number of positive droplets

Nn = number of negative droplets

V = average droplet volume 0.85 nL

Table 14. Components used for one ddPCR reaction.

Components	Volume for one reaction
ddPCR Supermix for Probes	10.5 µL (900 nM)
Target-specific primers	1.05 µL (250 nM)
MseI restricition enzyme	1.05 µL
ddH_2O	1.05 µL
DNA	6.3 µL (10 ng)
Total volume	**21 µL**

Table 15. Cycling protocol for ddPCR.

Reaction Mix	Conditions		
Enzyme activation	95 °C	10min	
Denaturation	94°C	30s	40x
Annealing/extension	55°C	60 s	
Enzyme deactivation	98°C	10min	
	4 °C	hold	

5.4.5 Whole exome sequencing

Genomic DNA was isolated as described in 5.4.1 from both organoid lines and blood as reference tissue. DNA concentration was fluorimetrically determined using the Qubit 3.0 system. Library for Whole Exome Sequencing were prepared using the Agilent SureSelectXT Low Input Exome-Seq Human v7 kit following the manufacturer's instructions. Samples were sequenced on an Illumina NovaSeq 6000 sequencer, resulting in approximately 140 Mio. 100 bp-long paired-end reads per sample. The GATK Best Practice suggestions were followed for alignment and mutation calling. After read trimming using Trimmomatic 0.38 (LEADING:25 TRAILING:25 MINLEN:50), BWA-MEM 0.7.17 was used to align reads to the human reference genome (GRCh38.p7). Picard 2.18.26 and GATK 4.1.0.0 were used for postprocessing (CleanSam, MarkDuplicates, BaseRecalibrator) using default settings. Somatic mutations

were called using MuTect2 v4.1.0.0 (default settings). Mutations with at least two reads supporting the alternate allele and a base coverage of at least 10 in the tumor and germline were kept. Single nucleotide variants (SNVs) and insertions/deletions (Indels) ≤ 10 base pairs were annotated using SnpEff 4.3t, based on ENSEMBL 92. Copywriter 2.6.1.2 (default settings) was used for the detection of copy number variations.

5.4.6 RNA isolation and cDNA synthesis

Cells were seeded in a 10 cm dish and harvested when they reached approximately 80% confluency. Thus, medium was aspirated and 350 µl of RLT buffer supplemented with 3.5 µl of 2-mercaptoethanol were added. Cells were harvested using a cell scraper and disrupted using a syringe. For organoids, cells of approximately 5-6 confluent wells were collected in a cell pellet and 350 µl of RLT buffer supplemented with 3.5 µl of 2-mercaptoethanol were added. RNA isolation was carried out using the RNeasy mini kit according to manufacturer´s protocol. cDNA synthesis was performed using the SensiFastTM cDNA Synthesis Kit following the manufacturer´s instructions. Generally, 1 µg of RNA were used for generation of cDNA, which was stored at -20 °C.

5.4.7 Quantitate real-time PCR (RT-qPCR)

RT-qPCR was performed with the StepOnePlus™ real time PCR system. As fluorescent DNA binding dye, the SensiFastTM SYBR Hi-Rox Kit was used according to manufacturer´s protocol in a 20µL mixture. mRNA expression was analyzed in triplicates on 5µL of cDNA, which was diluted 1:10 in qPCR water prior to usage. As a reference gene, the housekeeping gene β-actin was used. A melt curve was always done after the run to check for unwanted primer dimerization. Data analysis was performed with StepOne™ software and Excel according to the 2-ΔΔCt method (Pfaffl, 2001). Calculation was performed as follows:

ΔCt= Ct [gene of interest] – Ct [control gene]

$\Delta\Delta$Ct= ΔCt [treated sample] – ΔCt [reference sample]

2-ΔΔCt was used for data analysis and presentation of results.

5.4.8 Library preparation and RNA-Sequencing

To compare gene signatures and underlying signaling pathways, RNA sequencing analysis of PDAC cells upon FFX and Gem/nP treatment as well as a washout phase was performed. mRNA was extracted as described in 5.2.4. Library preparation for bulk-sequencing of poly(A)-

RNA was done as described previously (Parekh et al., 2016). Briefly, barcoded cDNA of each sample was generated with a Maxima RT polymerase (Thermo Fisher) using oligo-dT primer containing barcodes, unique molecular identifiers (UMI) and an adaptor. Ends of the cDNAs were extended by a template switch oligo and full-length cDNA was amplified with primers binding to the TSO-site and the adaptor. NEB UltraII FS kit was used to fragment cDNA. After end repair and A-tailing a TruSeq adapter was ligated and 3'-end-fragments were finally amplified using primers with Illumina P5 and P7 overhangs. In comparison to Parekh et al., the P5 and P7 sites were exchanged to allow sequencing of the cDNA in read1 and barcodes and UMIs in read2 to achieve a better cluster recognition. The library was sequenced on a NextSeq 500 (Illumina) with 63 cycles for the cDNA in read1 and 16 cycles for the barcodes and UMIs in read2. Data was processed using the published Drop-seq pipeline (v1.0) to generate sample- and gene-wise UMI tables (Macosko et al., 2015). Reference genome (GRCm38) was used for alignment. Transcript and gene definitions were used according to the GENCODE Version M25.

5.5 Protein biochemistry

5.5.1 Protein extraction

For harvesting protein, cells were cultured in a 10 cm dish until they reached around 80% confluency. Then, medium was removed and cells were washed twice with PBS. Organoids were processed as mentioned above to a cell pellet. Depending on the number of cells, 150 to 200 µl of cold RIPA lysis buffer were added and cells were harvested using a cell scraper. The protein samples were snap frozen in liquid nitrogen and stored at -20 °C until they were further used.

5.5.2 Protein concentration estimation

In order to determine the protein concentration in the lysates, the Bradford assay was carried out. Therefore, lysates were centrifuged at 4 °C and 15000 rpm for 20 min and the supernatant was transferred to a new reaction tube. 300 µl of the Bradford reagent, diluted 1:5 in distilled water, were placed into the wells of a 96-well plate and 1 µl of protein lysate was added as triplicates. To obtain a standard curve as reference, 0, 0.5, 1, 2, 4 and 8 µl of 1xBSA were used. Absorbance was measured at 595 nm using the photospectrometer Multiscan FC. Afterwards, all lysates were adjusted to the same protein concentration using protein loading (4x Laemmli) and RIPA buffer. For denaturation, samples were heated at 95 °C for 5 min and then stored at -20 °C.

5.5.3 SDS polyacrylamide gel electrophoresis (SDS-PAGE)

To allow the separation of proteins according to their molecular weight, SDS-PAGE was performed. Due to the protein size of the proteins of interest, 12% gels were prepared according to Table 16. After mixing the reagents for the separating gel and filling the gel chambers, 2-propanol was added to prevent gels from drying out. After polymerization, the stacking gel was prepared and added on top. Pockets were loaded with 100-120 µg of protein sample and SDS-PAGE was carried out the first 30 min at 80 V and later at 120 V for approximately 1.5 h.

Table 16. Mixture of components for one SDS polyacrylamide gel.

Compounds	12% separating gel	Stacking gel
H_2O	1700 µL	1500 µL
Separating gel buffer	1300 µL	-
Stacking gel buffer	-	650 µL
Rotiphorese® gel 30	2000 µL	375 µL
10% SDS	50 µL	25 µL
10% APS	25 µL	12.5 µL
TEMED	7.5 µL	5 µL

5.5.4 Immunoblot

After the gel electrophoresis, proteins were transferred onto a nitrocellulose membrane using a tank blot system. Blotting was performed at 350 mA for 1.5 h or 90 mA for 16 h at 4 °C. Afterwards, membranes were blocked with 5% skim milk or 5% BSA in PBS at RT and then incubated with the primary antibodies, diluted 1:1000 in 5% milk or BSA, overnight at 4 °C. After washing membranes three times with PBST for 15 min, they were incubated with the secondary antibody, diluted 1:10000 in 5% milk or BSA, for 1 h at RT in the dark. Before detecting the proteins at either 700 nm or 800 nm wavelength using the Odyssey ® infrared imaging system, three washing steps with PBST were carried out.

5.5.5 Proteomic analysis

Sample Preparation

Proteomic analysis was performed at the Institute of proteomics and bioanalytics at the TUM school of life sciences. Therefore, protein of cells in an untreated, 72h FFX and 72h wash out condition was harvested. Therefore, medium was removed and cells were washed twice with PBS. 200 µL of SDS lysis buffer was added and evenly distributed on the cells. After 5min of

incubation on ice, the lysate was collected using cell scrapers. To hydrolize the DNA and thereby reduce viscocity, the sample was boiled at 95 °C for 10 min and trifluoroacetic acid was added to a final concentration of 1 %, incubated for 1-2 min at 95°C and subsequently quenched with N-methylmorpholin (final concentration of 2 %) to obtain a pH of 7.5-8. The protein concentration in cell lysate was determined using the Pierce™ BCA Protein Assay Kit according to the manufacturer's protocol. In order to remove detergent from the sample, the protein lysate was processed via SP3 sample workup. The beads suspension was prepared by mixing magnetic SeraMag-A (c = 50 mg/ml) and SeraMag-B (c = 50 mg/ml) beads in a ratio of 1:1, immobilized on a magnet and the Supernatant was removed (Volume of the supernatant was noted down). Beads were washed twice with ddH_2O and then resuspended in ddH2O in the original volume. A total of 200 µg per sample for the tandem mass tags (TMT) workflow and 150 µg for the Label free experiment was mixed 1:10 (protein/beads weight) with the beads suspension. Acetonitrile (ACN) was added to a final concentration of 70 % and incubated at room temperature, 18 min, 800 rpm. After discarding the supernatant, beads were washed twice using 1 ml 80% ethanol and then once more washed with 1 ml of 100 % ACN and air dried for 2 min. For reduction and alkylation, beads were resuspended in 100 µl digestion buffer without trypsin (100 mM HEPPS, 2 mM CaCl2, 55 mM 2-Chloracetamid, 10 mM Tris-(2-carboxyethyl)-phosphin) and incubated for 1h at 37 °C and 800 rpm. Proteins were digested o/n at 37 °C by adding Trypsin 1:50 (trypsin/substrate weight) resuspended in 10 mM HEPPS in a volume of 10 µl per sample at 1000 rpm. Samples were sonicated 3 times for 30 sec, centrifuged (5 min, 13000 g) and supernatant was collected. Beads were washed once with 50 µl ddH_2O, sonicated 3 times for 30 sec, centrifuged (5 min, 13000 g), and supernatants were combined with previous supernatants. Peptide concentration was determined using a NanoDrop spectrophotometer. Samples were frozen at -80 °C and dried in a SpeedVac. Samples were reconstituted in 500 µl 0.1 % FA, desalted using tC18 RP solid-phase extraction cartridges (Waters Corp.; wash solvent: 0.1% FA; elution solvent: 0.1% FA in 50% ACN), frozen at -80 °C and dried in a SpeedVac. After desalting, LFQ samples were ready for measurement and stored at -20 °C until LC-MS^3. Samples that were analyzed via LC-MS^3 were further processed. Therefore, 100 ug of the desalted protein digest were labeled withTMT10-plex (Thermo Fisher Scientific) as previously described (Zecha et al., 2019). One TMT channel was used for each treatment condition and replicates (126 = Control, 127N = 4 h CTX, 127C = 8 h CTX, 128N = 24 h CTX, 128C = 48 h CTX, 129N = 72 h CTX, 129C = 4 h WO, 130N = 8 h WO, 130C = 24 h WO, 131N = 48 h WO). After labeling, peptides were pooled in a fresh tube. The TMT pool was frozen at – 80 C and dried in a SpeedVac. The peptide pool was reconstituted in 500 µl 0.1 % FA and desalted using tC18 RP solid-phase extraction cartridges (Waters Corp.; wash solvent: 0.1% FA; elution solvent: 0.1% FA in 50% ACN). A Dionex Ultra 3000 HPLC system operating a Waters XBridge BEH130 C18 3.5 µm 2.1 × 150 mm column

was used to fractionate 500 ug of the pooled protein digest (reconstituted in 200 µl solvent A). Solvent A was 25 mM ammonium bicarbonate (pH = 8.5), solvent B was 100 % ultrapure water (ELGA), solvent C was 100 % ACN. The proportion of buffer A was kept at 10 % during separation. Separation was obtained from a linear gradient from 7-45% C in 45 min at a flow rate of 200 µl/min, followed by a linear gradient from 45-85% C in 6 min. Fractions were collected every 30 sec into a 96 well plate and subsequently pooled into 48 fractions by adding fraction 49 to fraction 1, fraction 50 to fraction 2 and so forth and acidified with FA to a final concentration of 0.1 %. Peptide fractions were frozen at −80 °C freezer, dried in a SpeedVac without prior desalting, and stored at -20 °C until LC-MS^3 analysis.

Liquid chromatography and mass spectrometry

For microflow LC-MSMS analysis samples were analyzed on a micro-flow LC-MS/MS system using a modified Vanquish pump (Thermo Fisher Scientific) coupled online to a Q Exactive Orbitrap HF-X mass spectrometer (Thermo Fisher Scientific). Chromatographic separation was performed via direct sample injection onto the head of a 15 cm Acclaim PepMap 100 C18 column (2 µm particle size, 1 40mm ID, Thermo Fisher Scientific) at a flow rate of 50 µL/min. Solvent A was 0.1% FA, 3% DMSO in ddH2O, and solvent B was 0.1% FA, 3% DMSO in ACN (Bian et al., 2020). Column temperature was maintained at 55 °C using the integrated column oven. Samples were dissolved in 0.1 % FA and 50 ug of the protein digest were injected into the system. Samples were separated with a gradient of 1% to 24% B in 105 min followed by an increase of B to 35 % in 15 min. The HF-X was operated in positive ion mode, using an electrospray spray voltage at 4.0 kV, a funnel RF lens value of 40, capillary temperature of 320 °C and auxillary gas heater temperature of 300 °C. The flow rates for sheath gas, aux gas and sweep gas were set to 35, 5, and 0, respectively. Full MS resolution was set to 60,000 at m/z 200 and full MS AGC target was 3E6 with a maximum injection time (IT) of 50 ms. Mass range was set to 360–1300. AGC target value for fragment spectra was set to 1E5. The dynamic exclusion duration was set to 40 s. The TopN value was set to 50. For MS2 spectra, the minimum AGC target was kept at 2E3. The isolation width was set to 1.3 m/z, and the first mass was fixed at 100 m/z. The normalized collision energy was set to 28 %. MS1 and MS2 spectra were acquired in profile and centroid mode, respectively. For the full proteome analysis, the optimized 28 or 41 Hz methods were used, which were optimized in the previous literature (Kelstrup et al., 2018).

For microflow LC-MS3 measurement, a Dionex UltiMate 3000 RSLCnano System was coupled online to an Orbitrap Fusion Lumos mass spectrometer (Thermo Fisher Scientific) (Bian et al., 2020). Peptides were dissolved in 0.1 % FA and one half was directly injected onto the

microflow LC system. Online chromatography was performed using a commercially available Thermo Fisher Scientific Acclaim 15 cm Acclaim PepMap 100 C18 column (2 µm particle size, 1 40mm ID, Thermo Fisher Scientific catalog number 164711)) at a flow rate of 50 µL/min. Column temperature was maintained at 55 °C using the integrated column oven. Peptides were delivered at a flow rate of 50 µl/min and separated using a 25 min linear gradient from 4 % to 32 % LC solvent B (0.1 % FA, 3 % DMSO in ACN) in LC solvent A (0.1 % FA, 3 % DMSO (Hahne et al., 2013). The Orbitrap Fusion Lumos was operated as follows: positive polarity; spray voltage 3.5 kV, capillary temperature 325 °C; vaporizer temperature 125 °C. The flow rates of sheath gas, aux gas and sweep gas were set to 32, 5, and 0, respectively. Cycle time was set to 1.2 s. Full MS was readout in the Orbitrap, resolution was set to 60,000 and the mass range was set to 360–1560. Full MS AGC target value was 4E5 with a maximum IT of 50 ms and RF lens value was set to 50. The MIPS properties were set to peptide. The MIPS properties were set to peptide. Default charges were set to state 2–6. The dynamic exclusion duration was set to 50 s, exclude after one time. For readout of MS2 spectra, the ion trap was used applying the rapid scan function. The isolation width was set to 0.6 m/z, the first mass was fixed at 100 m/z, activation type was HCD, HCD collision energy [%] was 32. The AGC target value was set to 1.2E4 at a maximum IT of 40 ms. The precursor selection range was set to 400–2000, exclusion mass widths were set to 20 m/z for low and 5 m/z for high. For MS3 spectra readout, the orbitrap was used at 50,000 resolution and over a scan range of 100–1000. Synchronous precursor selection (SPS) was enabled, the number of SPS precursors was set to 8. MS2 isolation window was 3 m/z, activation type was HCD, and HCD collision energy was 55 %. The AGC target was 1E5 with a maximum IT of 86 ms.

Data Analysis

Protein and peptide identification and quantification was performed MaxQuant (Cox and Mann, 2008) by searching the MS2 and MS^3 data against all protein sequences (canonical and isoforms) as annotated in the UniProt reference database (mouse proteins only, 25333 swissprot entries, downloaded 17.12.2020, internally annotated with PFAM domains) using the search engine Andromeda (Cox et al., 2011). Carbamidomethylated cysteine was set as fixed modification. Oxidation of methionine and N-terminal protein acetylation were set as variable modification. Trypsin/P was specified as the proteolytic enzyme and up to two missed cleavage sites were allowed. The Match-between-runs feature and label-free quantification were enabled for samples that were measured via LC-MS^2 (Cox et al., 2014). All other settings were set to standard Maxquant default settings. For TMT quantification of LC-MS^3 measured data the data was quantified by a MS^3 search also applying default settings and TMT correction factors as supplied by the manufacturer were considered.

5.5.6 Immunofluorescence (IF) staining

For immunofluorescence (IF) staining, 2D cells were cultured on cover slips in a 6 well plate and when ready, washed and fixed for 10 min at RT using 4% PFA. In order to avoid background signal, cells were treated with 0.15% glycine for 5 min. For IF staining, cells were briefly permeabilized with 0.2% Triton-X 100 in PBS. After washing, cells were blocked for 1.5 h in 10% donkey serum and 0.1% BSA diluted in PBS. The primary antibodies were incubated overnight at 4°C in 0.1% BSA diluted in PBS. After washing, the secondary antibodies were incubated for 2.5 h at RT in the dark. Thereafter, cells were treated for 2 min with DAPI (0.03 µL/mL in PBS), washed and mounted. Slides were kept at 4°C until further analysis using the Leica TCS SP8 Confocal Microscope.

For the IF staining of PDOs, organoids were washed and fixed with 4% PFA for 15 min at RT and treated with 0.15% glycine for 5 min followed by a 2 min permeabilization using 0.2% Triton-X 100 in PBS. After washing, cells were blocked in 10% donkey serum and 0.1% BSA diluted in PBS overnight at 4°C. Afterwards, phalloidin (Phalloidin-Atto 647N, 1:250) was incubated for 2.5 h at RT in the dark. Thereafter, cells were treated for 2 min with DAPI (0.03µL/mL), washed and imaged using the Leica TCS SP8 Confocal Microscope.

5.6 Bioinformatic analysis of transcriptomic and proteomic data

High-throughput mRNA gene expression data from the conditions indicated in the text were carried out using the R environment for statistical computing1 (v4.0.4).

Proteomic data analysis was performed using the Perseus software suite and R (version 4.0.02) on identified and quantified protein groups, which were filtered for contaminants and reverse hits. The data was normalized using median centering and log2 transformed.

Genome-wide differential gene expression analysis was calculated using the DESeq2 R package (Love et al., 2014) for RNA-Seq count data and the limma R package (Ritchie et al., 2015) for normalized protein expression data. A false discovery rate (FDR) of < 0.1 was considered significant. Phenotype specific contrasts were generated examined using per sample information on morphological subtype (epithelial, mesenchymal) and on drug treatment (control, FOLFIRINOX=FFX, Gemcitabine/nab-Paclitaxel=Gem/nP) at different time points (72 hours=main drug effect and 72 hours=wash out/WO).

One versus rest differential gene expression signatures comparisons were calculated within each morphological subtype by contrasting biological replicates from each treatment (control, FFX, Gem/nP, WO-FFX, WO Gem/nP) with all other samples using DESeq2 for RNA count data and limma for normalized protein expression data, respectively, as described above.

These subtype- and treatment-specific gene expression signatures (GES) were represented by Wald and moderated t statistics per gene for RNA count and normalized protein expression data, respectively. GES were interrogated by gene set enrichment analysis (GSEA) (Korotkevich, 2021; Subramanian et al., 2005) using the HALLMARK gene set collection from MSigDb version 7.4 (Liberzon et al., 2015). The resulting normalized enrichment score (NES) matrix with HALLMARKS in rows and subtype- and treatment-specific one vs. rest signatures in columns were illustrated using the pheatmap R package (Kolde, 2019).

For selected human PDO cultures and human 2D cell lines, respectively, molecular subtype classifier gene sets (Bailey et al., 2016; Chan-Seng-Yue et al., 2020; Collisson et al., 2011; Moffitt et al., 2015) were scored per sample using analytic rank-based enrichment analysis (aREA) (Alvarez, 2016) after computing transcriptome-wide expression single-sample signatures first rank transforming and rescaling first each column (cell line sample) and then each row (gene) between 0 and 1. The resulting NES matrix with classifier sets in rows and individual cell lines in columns was illustrated using the pheatmap R package (Kolde, 2019).

To determine single-sample normalized enrichment scores (NES) regarding EMT, aREA was applied on normalized RNA-Seq count and protein expression data, respectively, using the HALLMARK_EPITHELIAL_MESENCHYMAL_TRANSITION gene set without rescaling genes before single-sample enrichment analysis. Single sample EMT (ssEMT) scores were rescaled between 0 and 1 for better comparability between results from RNA-Seq and protein expression samples, respectively.

Raw count data from RNA sequencing from each of the two technical replicates for each organoid line were collapsed by summing all counts per gene into one final raw count profile per organoid line. Afterwards, the variance was stabilized by applying a regularized log transformation to the data as implemented in the DESeq2 R package while accounting for different library sizes (Love et al., 2014).

A log2 fold change gene expression signature was generated between post- and pre-treatment organoid lines and was used as the input for GSEA which was carried out using the fgsea R package (Korotkevich, 2021). Gene sets were retrieved from the MSigDb v7.3 (Liberzon et al., 2015; Subramanian et al., 2005). Enrichment results for select pathways were illustrated using custom R code.

Continuous classification using probabilities of class membership were determined for each PDO line using its normalized RNA-Seq profile. The purity independent subtyping of tumors (PurIST) single-sample classification scheme was implemented based on the gene pairs and coefficients provided by the authors using custom R code (Rashid et al., 2020). Importantly, adjustment of gene expression for total gene length was omitted because of the 3'prime end

sequencing protocol described above. For the respective PurIST gene pairs, gene expression values were illustrated in a heatmap comparing pre- and post-treatment PDO lines.

5.7 Digital holographic microscopy

5.7.1 Sample preparation

Cell lines or organoids were processed as mentioned in 5.3 and trypsinized for 5 – 15 min to obtain a single cell suspension. Trypsinization was stopped using STI and cells were centrifuged at 1000 rpm for 5min. Afterwards the cell pellet was resuspended in 500 – 1000 µL of 0.9% of polyvinylpyrrolidone (PVP) diluted in PBS.

5.7.2 DHM measurement

DHM

In order to distinguish between mesenchymal and epithelial cells, an imaging technique that provides sufficient contrast is required. For this reason, a digital holographic microscope (DHM) from Ovizio Imaging Systems (Ovizio) was used which is based on a Mach-Zehnder off axis interferometer setup. The microscope is equipped with a Nikon CFI LWD objective with 40x magnification and a numerical aperture of NA = 0.55, an Oslon PowerStar SLED (Osram) with a wavelength of λ = 528 nm and a PointGrey Grashopper GS3U332S4 camera which takes 105 frames per second with an exposure time of 5 µs. By using a low coherent SLED instead of a laser, image degradation is eliminated and the image quality is improved. The light beam from the SLED first transmits the sample, which is located in the back focal plane of the microscope objective. Afterwards the beam is split with a grating filter into diffraction parts and a non-diffraction part (reference). The diffracted part is further shifted in x and y direction compared to the reference. By recombination of the shifted parts and the reference, they can be interfered, resulting in a hologram, which is recorded on the camera. Finally phase and amplitude images can be extracted out of the hologram using common off-axis interferometer reconstruction algorithms (Kemper et al., 2019; Anand et al., 2018). A more detailed description of the setup and the working principle has been described before (Dubois et al., 2015; Ugele et al., 2018; Klenk et al., 2019).

Microfluidic chip

To be able to measure cell in high throughput the imaging setup was combined with a microfluidic chip. The channel has a height of 50 µm, a width of 500 µm and a total length of 50,000 µm and is made of poly(methyl methacrylate) (PMMA) (Fraunhofer ICT-IMM). Two microfluidic focusing methods were combined for precise alignment of a submonolayer of cells, thus eliminating the need for further adjustment of the focus after an initial setup. Hydrodynamic focusing could be achieved by using 5 inlets, containing one sample flow, two side flows (y-sheaths), a top and a bottom flow (z-sheaths). Here, the flow rates were adjusted so that the lateral streams were fixed at 0.5 µl/s and all other streams (sample, top and bottom) at 0.2 µl/s. This leads to a total flow rate of 1.6 µl/s which was adjusted with a neMESYS Base 120 syringe pump system with 5 modules (cetoni GmbH). Each slot was equipped with a 2.5-ml gas tight syringe (VWR). Furthermore, 0.9% of PVP diluted in PBS was used as media for each of the 5 inlets to achieve viscoelastic focusing of the sample. Overall the maximum Reynolds number during the measurements is in the single digit range (Re ≈6.5), which implies that all measurements were performed in the laminar flow regime.

5.7.3 Computational analysis

Pre-Processing

Capturing 100 hologram images per second, a single measurement contains roughly 10.000 shots. From these holograms the commercial OsOne Software reconstructs the phase information using Poisson integration (Ugele et al., 2018a). The software provides 384px by 512px phase images with floating point precision (typically within an interval [–2, 6]) that contain multiple cells. These images were preprocessed to obtain usable single-cell patches for the following classification. As a first step, any background noise was removed, and afterwards, single cells were segmented, features extracted and then filtered to get rid of poor images.

To remove background noise and artifacts of the microfluidic channel, background subtraction is estimated by taking the median of n images generating significantly better results in comparison to using the mean. Best results regarding computing time and quality of the background are obtained for n = 50, while for n<50, artifacts of cells are still detected in the computed background. Due to the fixed alignment of lens, camera, light, and microfluidic channel, the background is not showing any changes during a single capture. This allows the computation to be done the background to be calculated only once based on the first few images. Afterwards, the calculated background is subtracted from every image.

In order to find the important regions of the image containing cells, we apply binary thresholding to the phase images. Here, a threshold value of 0.8 delivered good results for filtering out small debris. From the resulting binary images we extracted the contours of each region of interest (Suzuki, 1985). Each contour which covers more than 30 pixels is stored with its corresponding 96px x 96px image patch around its center.

For feature extraction, we combined two features types, morphological features and residual neural networks (ResNet) features. Therefore, we analyzed each digitalized cell for its morphology (Ugele et al., 2018a; Ugele et al., 2018b). Using established functions from OpenCV together with hand crafted methods, the following features in table 17 showed the most descriptive power for several discrimination tasks. Here, N is the number of pixels assigned to the cell in the image, λ is the wavelength of the coherent light source, vi,j is the intensity value of the pixel at the 2D index(i,j) and r is the radius estimation for each point of the cell contour.

Table 17. Overview of morphological features, their calculations and applied filter boundaries used in this study.

Feature	Equation	Filter
aspect ratio	max(width*height)/min(width*height)	-
cell area	N * (0,345µm)^2	[50, 500]
circularity	4π*cell area/perimeter^2	[0.85, 1]
optical height max	max($v_{i,j}$) * (λ/2π) $2\forall_{i,j}$	-
optical height min	min($v_{i,j}$) * (λ/2π) $2\forall_{i,j}$	-
optical height mean	mean($v_{i,j}$) * (λ/2π) $2\forall_{i,j}$	-
solidity	cell area/conex hull area	-
sphericity	correlation to f(x)=-x^2+1	-
biconcavity	correlation to f(x)=-4x^2+4x^2+0.5	-
radius variance	var(r) * 0,345µm	-
homogeneity	$\sum_{i,j=0}^{N-1} \frac{Pi,j}{\sigma 1+(i-j)^2}$ with $\mathrm{Pi,j} = \frac{vi,j}{\sum_{i,j=0}^{N-1} vi,j}$	-
correlation	$\sum_{i,j=0}^{N-1} Pi,j \frac{(i-\mu)(j-\mu)}{\sigma^2}$, with, $\sigma^2 = \sum_{i,j=0}^{N-1} Pi,j(i-\mu)^2$ and $\mu = \sum_{i,j=0}^{N-1} iPi,j$	-
contrast	$\sum_{i,j=0}^{N-1} Pi,j(i-j)^2$	

ResNets and their characteristic skip connections (He, 2015) are inspired by pyramidal cells in the cerebral cortex. Here, a lightweight ResNet with 18 convolutional layers (ResNet18) has been used for feature extraction. The network has been pretrained on the ImageNet dataset and thereby, it is capable of extracting the most prominent structures within images. In contrast to previous state of the art image classification networks like VGG-16 its layers are not simply stacked one on each other but organized in residual blocks. Using it as a feature extractor is possible by cutting the last fully connected layer, that would already perform a classification, and use the output of the second to last layer as features for our analysis. This layer provides 512 abstract features that describe the inherent structures of the images.

Sample preparation of our cells as well as our measurement setup with its high-throughput can lead to some damaged, deformed or unfocused cells. Since they can possibly disturb the classification, they have to be filtered. Therefore, we set some boundaries to the calculated morphological features based on their distribution and our experience with this approach in general. The applied filter rules are depicted in table 1.

Classification

The two generated feature sets, morphological and resnet features, are then used in various classification and clustering approaches to achieve the goal of separating the different cells respectively in each experiment. All of the experiments have been conducted with balanced datasets and using a cross-validation with 5 splits.

Random Forest (RF) is an ensemble classification method based on decision trees (Breiman, 2001). For random forests classification, a multitude of decision trees is automatically constructed based on different fractions of the given dataset. For classification of unknown samples, the average result of all trained decision trees is used. This concept reduces overfitting very effectively and works well for more complex classification tasks with large amounts of features. In our implementation we limited the algorithm to 100 individual decision trees without setting a bound for the maximum depth of a single tree.

A Support Vector Machine (SVM) is a binary linear classification technique, which divides data into two classes using the best hyperplane decision boundary. This decision boundary is obtained by maximizing the margin between the class border and sample data (Boser, 1992; Cortes, 1995). To classify non-linearly separable sample data the so-called kernel trick is utilized to provide non-linear combinations of the input data. Most commonly polynomial, sigmoid, or gaussian radial basis function kernels are used. Since in practice datasets are usually not perfectly separable, a concept named soft margin is applied which allows some

data points to violate the margin condition resulting in penalization. As a result, we achieved the best performances using a penalty parameter C =1 and radial basis function as kernel.

The K-Nearest Neighbor (k-NN) classifier is one of the simplest methods to classify data. It assumes that every class can be represented as a single cluster. For new data points it calculates the distance to all the other points using e.g. the euclidean distance and then assigns them to the class to which the majority of the neighbors belong. With the parameter k you can define how many of the nearest neighbors will be analyzed before assigning the class (Cover, 1967; Cunningham, 2021). k-NN is based on the idea that similar samples lie closer together in the feature space. The easiest and fastest classification is achieved with k=1, which simply classifies depending on the nearest sample point. This implementation is very vulnerable to noise which can be prevented with a higher k to get results that are more robust to noisy data or imperfect training samples. For this paper we set k=5.

(Artificial) Neural Networks (NN) are based on the biological concept of neurons simulating the human brain. They prove to be very successful in many but not solely machine vision problems due to their learning capabilities. An artificial neuron (Rosenblatt, 1958) takes multiple inputs and outputs the weighted sum of these inputs after applying an activation function. Many interconnected artificial neurons form a network (Hornik, 1989). The learning ability is achieved by adapting the neuron’s weights (axons) based on a sequence of training samples during a learning phase. Fostered by rapidly growing available computational power, networks with multiple hidden layers, called deep neural networks, are getting increasingly popular. For this work, a rather simple multi-layer neural network was created. It consists of a single hidden layer with 100 neurons and utilizes the Adam algorithm (Kingma, 2017) and a cross-entropy (Wang, 2020) loss function for optimization. The training was performed in batches of 256 samples.

Visualization

For the dendrogram we selected the 26 features with the highest impact (based on the *RF Importance*) to be shown on the y-axis. The hierarchical clustering at the top is performed using single linkage (Nielsen, 2016).

The Uniform Manifold Approximation and Projection (UMAP) (McInnes, 2018) is a clustering and visualization approach that uses all available features and represents them in a lower dimensional representation, e.g. in two dimensions as we did in the paper. In comparison to a standard dot plot, where you are limited to selecting two features for your visualization, this method can lead to more distinct clusters since it can make use of more information.

Based on the euclidean distance, it calculates a similarity measure among all data points. This describes how likely it is that these data points lie close together. The data points are then placed in the two-dimensional representation and moved around in an iterative fashion, until the similarity conditions are best satisfied.

As an indicator for the homogeneity of a cluster, you can calculate the distance of the data points to the cluster center. For an individual data point xi, this is calculated as

$d_i = ||x_i - c||_2$,

with c being the center of the cluster. The resulting values can then be compared by either calculating a mean value for each cluster or by analyzing their distribution in a violin plot.

Since this measure focuses on the dispersion of the individual cluster without considering the structure of the other clusters, it results in a robust analysis that is not susceptible to influence by poor measurements.

6 Results

6.1 DHM as label-free tool for high-throughput characterization of PDAC

6.1.1 Establishment of the DHM workflow

The aim of this study was to establish DHM for a detailed phenotypic characterization of PDAC on a cellular level in a label-free high-throughput fashion. We used a customized DHM (Oliver Hayden, TUM) coupled to a microfluidic system allowing us to focus on a single cell suspension flowing through the DHM system. Therefore, we processed cells derived from cell culture into a single cell suspension to measure them with DHM in flow. Single-cell phase images were then subjected to a computational analysis pipeline. In the first step we pre-processed the obtained phase images by subtracting the background to remove noise and artifacts. Then, using binary thresholding, we performed cell segmentation to find the regions of interest. For feature extraction and filtering we combined morphological features, partly derived from OpenCV and partly hand-created, with a lightweight residual neural network with 18 convolutional layers (ResNet18). As a last step, we applied the commonly used pixel-based classification tools random forest (RF), support vector machine (SVM), K-nearest neighbors (K-NN) and neuronal networks (NN) in order to discriminate experimental samples and visualized the results using hierarchical or UMAP clustering. The obtained results provide insight into tumor cell plasticity and particularly intratumoral heterogeneity. The established workflow is illustrated in Figure 1.

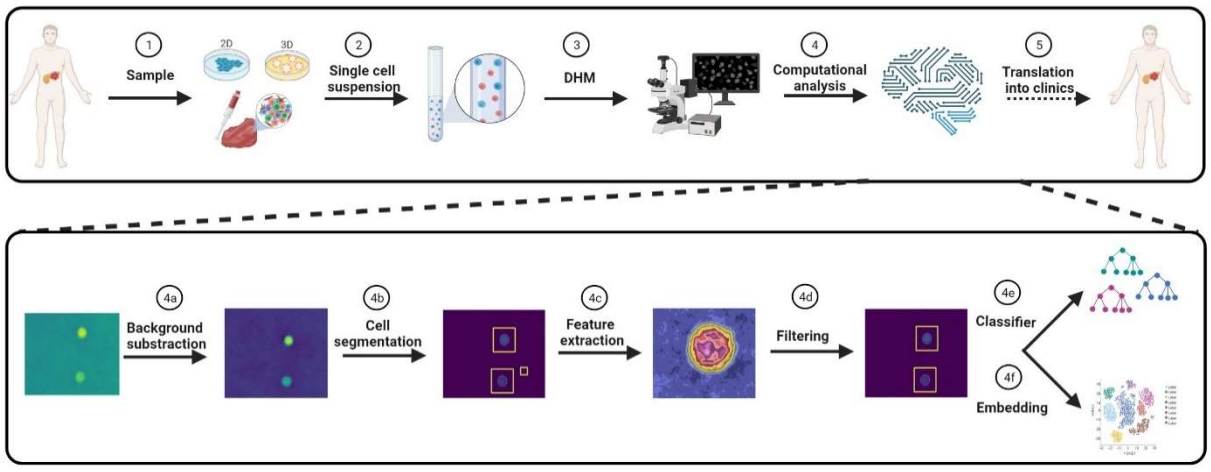

Figure 1. Schematic illustration of the established workflow of digital holographic microscopy.

6.1.2 Differentiation of two most distinct cell morphologies

Since cells in suspension appear round and consequently are visually inseparable from each other, we determined whether cells with most distinct morphologies in adherent cell culture can still be differentiated in a label-free single-cell approach using DHM.

To do so, we chose HPDECs with a classical cobblestone morphology and CAFs with spindle-like shape in our first comparison. The difference in morphology in an adherent condition is clearly recognizable by normal phase contrast microscopy as well as immunofluorescence staining of the actin filaments (Figure 2A). In addition, the expression of lineage markers for ductal epithelial cells such as cytokeratin 19 (CK19) and E-Cadherin as well as for CAFs such as α-SMA, Zeb1 and Vimentin were significantly different between the two cell types at RNA and protein levels (Figure 2B, C). Next, cells were measured in flow using DHM and analyzed with the four established machine learning classifiers (Figure 2D, E). All classifiers delivered good results, however Random Forest classification performed best throughout this study, therefore we focus further on only on this classification method. Here, using Random Forest classification we observed a separation of almost 85% based on morphological+ResNet18 features (Figure 2E). In addition, a right shift of the CAFs compared to the HPDECs was observed in UMAP analysis (Figure 2F). DHM demonstrates that even though HPDECs and CAFs look similiar in a round-up condition, the algorithm is capable of separating and clustering them with high accuracy.

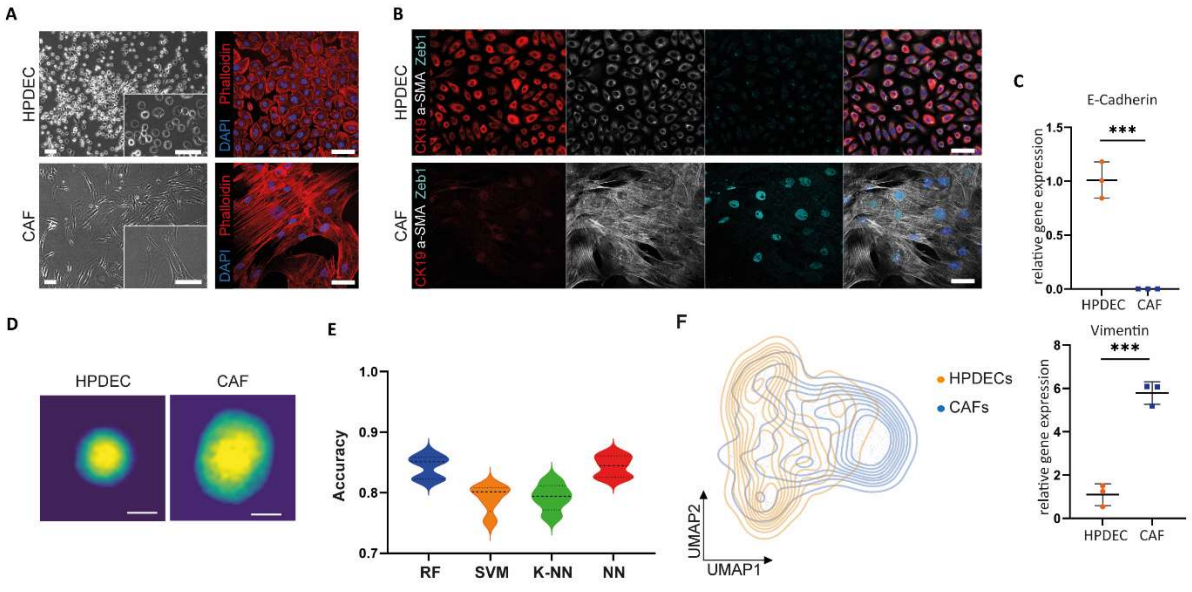

Figure 2. Separating ductal epithelial cells and cancer-associated fibroblasts.
A, Phase-contrast images and immunofluorescence staining of the cytoskeleton of HPDECs and CAFs. Scale bars represent 200µm (left) and 100µm (right). B, Immunofluorescence staining of CK19, α-SMA and Zeb1 of HPDECs and CAFs. Scale bars represent 100µm. C, Relative mRNA expression of E-cadherin and Vimentin in HPDECs and CAFs. Unpaired student´s t test of n=3 independent replicates, ***p<0.001. D, DHM phase images of HPDECs and CAFs. Scale bars indicate 10 µm. E, Accuracy for separating HPDECs and CAFs using different classification methods: random forest (RF), support vector

machine (SVM), K-nearest neighbors (K-NN) and neuronal network (NN). F, Unsupervised clustering of HPDECs and CAFs based on DHM phase images and visualized using the UMAP plot

6.1.3 Identifying TGF-β-induced EMT on a single-cell level

We next wanted to address whether we are able to identify morphological changes within a cell line. Treatment regimens like chemotherapy often induce phenotypic changes, such as EMT, in tumor cells (Hwang, 2020; Porter et al., 2019), which we wanted to mimic in a controlled setting using TGF-β. Therefore, we treated well-characterized murine epithelial PDAC cells for 14 days with TGF-β in order to induce EMT and to determine the phenotype switch within each line using DHM (Mueller et al., 2018). As expected, the epithelial cells lost their cell-cell contact and transformed into spindle-like spiky cells illustrated via phase contrast microscopy and F-actin staining (Figure 3A, C). For validation, EMT markers of untreated as well as TGF-β-treated cells were assessed on mRNA as well as protein level. Both showed a dramatic decrease in the epithelial marker E-Cadherin and an increase in the mesenchymal markers N-Cadherin and Vimentin (Figure 3B, C). However, the cell line 8442 did not respond as strongly to TGF-β treatment in comparison to 9591 and 53631, where a better response was observed as depicted in the phase-contrast images as well as IF staining. At a single cell level, comparing the morphological features upon EMT induction clearly showed differences in the respective DHM phase images (Figure 3D). For cell lines 9591 and 53631 the algorithm could predict a difference in morphology of 81% and 85% of untreated versus treated cells, respectively. In contrast, line 8442 showed a difference in only 75% of cells (Figure 3E). These results were visualized using UMAP analysis, in which a clear right shift was identified in 9591 and 53631 while 8442 showed a minor transition with a big overlap between control and TGF-β-treated cell morphologies (Figure 3F). This in turn recapitulated our observations of line 8442 in the validation experiments and was taken as an internal quality control for the algorithm we used in this study. Using DHM allowed us to identify TGF-β-induced EMT in murine PDAC cells and we additionally found a high degree of inter- as well as intratumoral heterogeneity strengthening the utility of our single-cell approach.

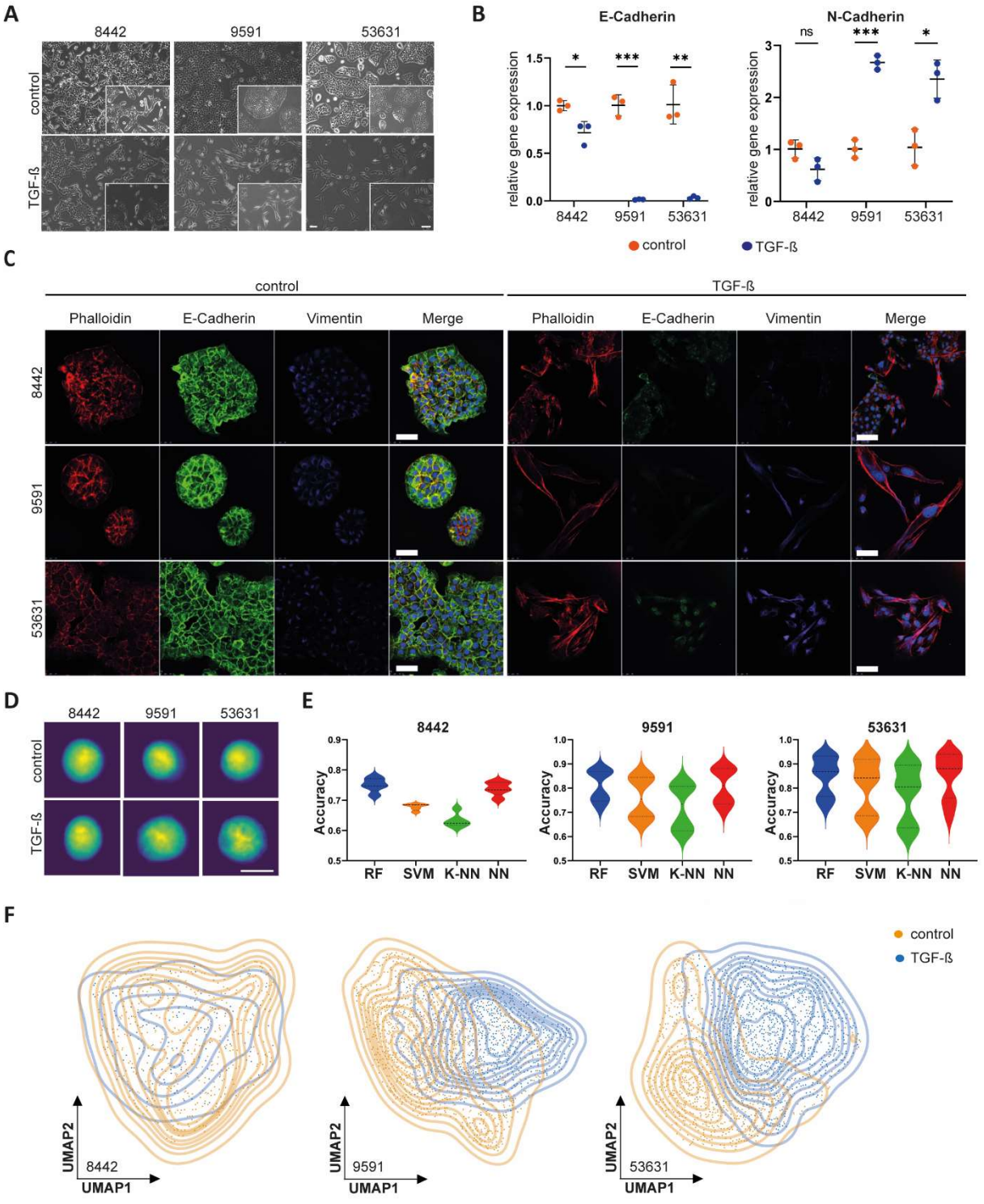

Figure 3. Identification of TGF-β-induced EMT.
A, Phase contrast images of control and TGF-β-treated epithelial PDAC cells. Scale bars represent 200 µm. B, Relative mRNA expression of E-cadherin and N-Cadherin compared between the control and TGF-β-treated condition. Unpaired student´s t test, ns = not significant, *p<0.05, **p<0.01 ***p<0.001. C, Immunofluorescence staining of Phalloidin, E-Cadherin and Vimentin in control and TGF-β-treated PDAC cells. Scale bars represent 100 µm. D, DHM phase images of control and TGF-β-treated PDAC cells. Scale bars represent 10 µm. E, Accuracy for separating control and TGF-β-treated PDAC cells individually for every cell line using different classification methods: random forest (RF), support vector machine (SVM), K-nearest neighbors (K-NN) and neuronal network (NN). F, Unsupervised clustering of control and TGF-β-treated PDAC cells based on DHM phase images and visualized using UMAP plots.

6.1.4 Clustering tumor cell plasticity according to their *p120catenin* mutation status

In a similar approach, we used genetically engineered murine *Kras*-mutant cells with wildtype (WT) or a homozygous deletion of *p120-catenin* (*p120ctn)* – the cytosolic binding partner of E-Cadherin and thus, an important component for adherens junctions (Reichert et al., 2018). The bi-allelic depletion of *p120ctn* leads to endocytosis and degradation of E-Cadherin and thereby induces the loss of epithelial identity accompanied by an acquisition of morphological features related to EMT. Consequently, genetically modulating epithelial plasticity via *p120ctn* was used as an alternative model system to train DHM for detecting different stages of EMT and plasticity, features that are important for PDAC characterization. The differences in phenotype upon *p120ctn* ablation were clearly visible in phase contrast microscopy as well as IF staining of cells in an adherent condition with the *p120ctn -/-* cells demonstrating spindle-like features (Figure 4A, B). Thus, indirectly removing E-Cadherin from the adherens junctions without the increase of the mesenchymal marker Vimentin is enough to remodel cellular morphology (Figure 4B). These morphologically different lines were subjected to DHM analysis (Figure 4C). Random Forest classification allowed a separation of 80% between WT and knockout cells with a clear right shift in the cells harboring a *p120ctn* deletion (Figure 4D, E). Again, this illustrates the capability of DHM to correctly identify the EMT status of PDAC cells in a controlled and characterized setting.

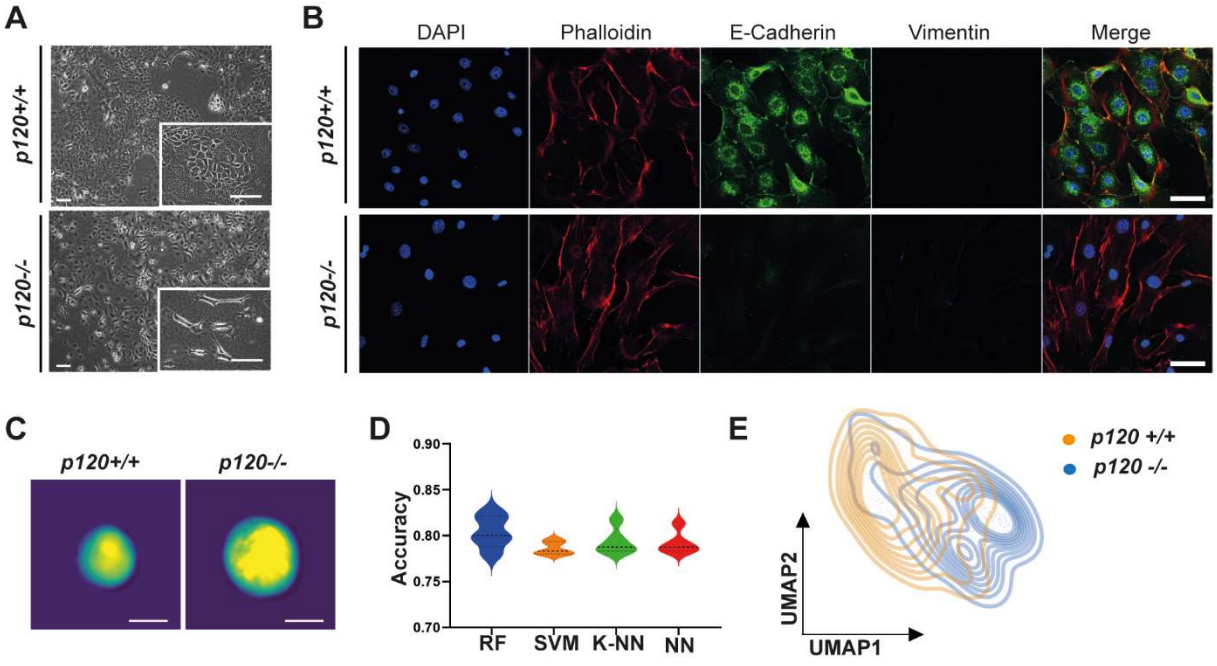

Figure 4. Detecting EMT in genetically engineered tumor cells harboring a *p120catenin* knockout. A, Phase contrast images of cells with *p120catenin* wildtype (*p120+/+*) or homozygous (*p120-/-*) deletion. Scale bars represent 200µm. B, Immunofluorescence staining of the EMT markers E-Cadherin, Vimentin and Phalloidin in *p120+/+* and *p120-/-* cells. Scale bar represents 100µm. C, Representative DHM phase images of *p120+/+* and *p120-/-* cells. Scale bars represent 10 µm. D, Accuracy for separating *p120+/+* and *p120-/-* cells using different classification methods: random forest (RF), support vector machine (SVM), K-nearest neighbors (K-NN) and neuronal network (NN). E, Unsupervised clustering of *p120+/+* and *p120-/-* cells based on DHM phase images and visualized using UMAP plots.

6.1.5 Phenotypic subtyping of characterized murine PDAC cells

As we have looked at EMT in a controlled setting by now, we wanted to focus on pancreatic cancer plasticity and heterogeneity in a more complex environment. Therefore, we used molecularly characterized murine PDAC cells recently grouped into the C2b and C1 cluster representing epithelial and mesenchymal cell morphology, respectively (Mueller et al., 2018). Hierarchical clustering based on their bulk transcriptomes (2000 most differentially expressed genes) clearly separates them according to their defined phenotype (Figure 5A). However, the mRNA expression levels of the main EMT markers like E-Cadherin, EpCAM, N-Cadherin, Vimentin, Zeb1 and Snail1 strongly vary not only between the two clusters but also within each cell line indicating a certain degree of heterogeneity within each cluster (Figure 5B). Going back to the cell morphology in an adherent cell culture condition, we indeed found a hybrid-like phenotype in 8442 with a large number of cells showing mesenchymal features and 8028 exhibiting a considerable sub-population of epithelial cells (Figure 5C). The other cell lines showed a subpopulation of the opposite phenotype as well, but not to the same extent as 8442 and 8028 emphasizing the presence of intratumoral heterogeneity, which remained undetected in bulk RNA sequencing.

As expected, measuring these lines with DHM and analyzing it using morphological+ResNet18 features did not predict a clear separation of phenotypes (Figure 5D). Random Forest classification of cells derived from the C2b versus C1 cluster showed a differentiation accuracy of only 72% (Figure 5E). However, UMAP clustering revealed a continuum of cellular phenotypes within each cluster as well as each cell line confirming high levels of inter- and intratumoral heterogeneity, a well-known and challenging feature of PDAC (Figure 5F). While the vast majority of 9591 and 53631 clustered on the left side of the spectrum, 8442 covered the whole spectrum with the majority located in the middle. Similar to this, 8028 showed a great overlap with the epithelial phenotype, while 9091 and 16992 clustered mainly on the right side of the spectrum (Figure 5G). Additionally, hierarchical clustering based on DHM showed a closer relationship between 8442 and 8028 than each cell line has to the members of their transcriptomic subtype further strengthening the hybrid-like EMT state of both (Figure 5H). Calculating the single cell distance to the cluster centroid allowed us to evaluate and quantify intratumoral heterogeneity from DHM-derived phase images. As expected, the cell lines 9591 and 53631 exhibited the lowest degree of intra-cell line heterogeneity while 8028 showed the highest score (Figure 5I). These data strongly indicate that although cells are grouped into a defined tumor subtype based on their bulk transcriptomic profile, they can be composed of a highly heterogeneous cell population, which can be analyzed in detail only using single cell technologies.

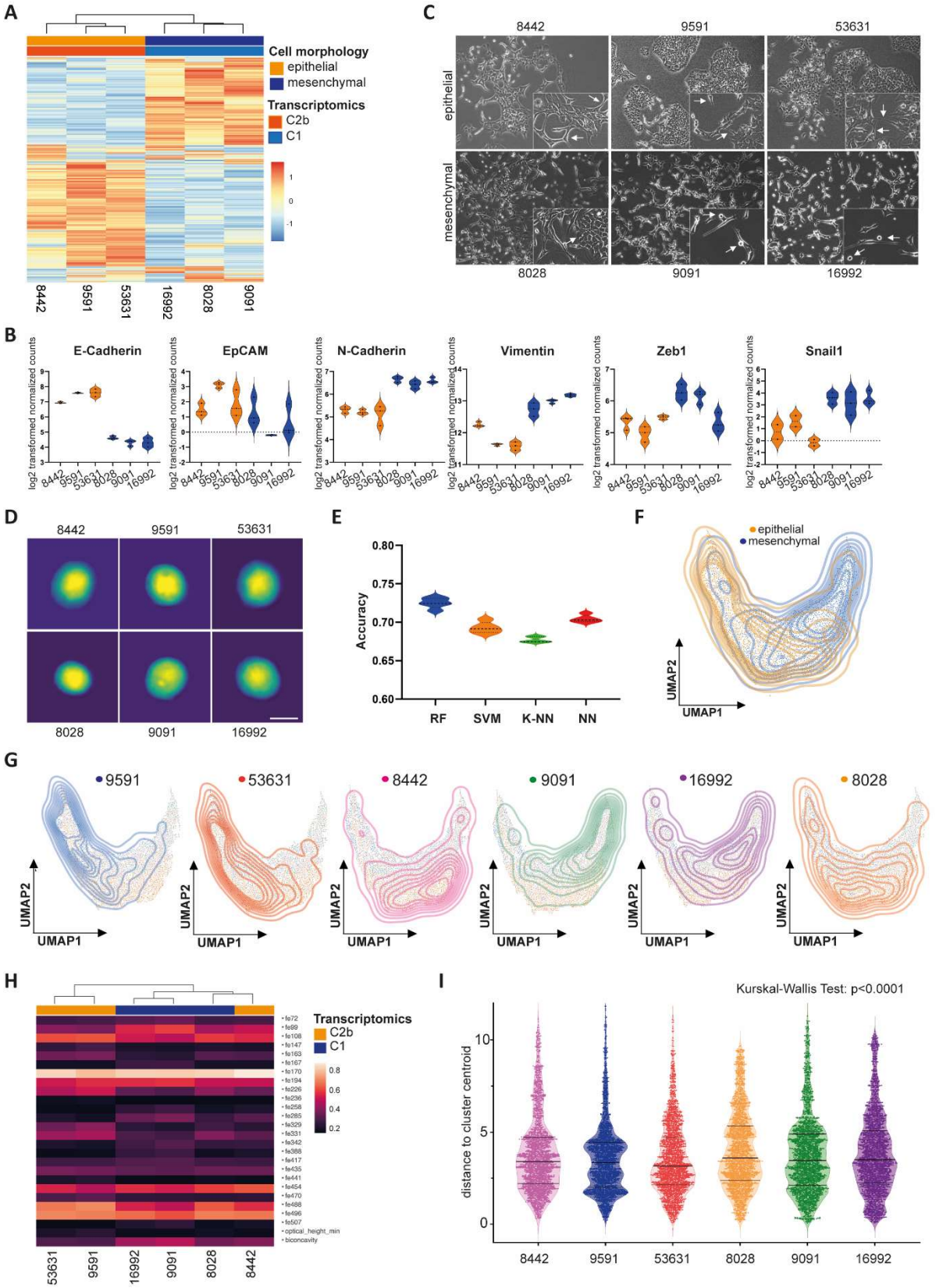

Figure 5. Label-free clustering of epithelial and mesenchymal murine PDAC cells.
A, Hierarchical clustering of 2000 most variable genes based on transcriptomic profiles of the six murine PDAC cell lines. n = three independent replicates per cell line. B, Relative expression of EMT markers (E-Cadherin, EpCAM, N-Cadherin, Vimentin, Zeb1 and Snail1) based on RNA sequencing compared between epithelial (E) and mesenchymal (M) PDAC cells. n = three independent replicates per cell line.

C, Phase contrast images of epithelial and mesenchymal PDAC cells. Arrows indicate subpopulations of the opposing phenotype. Scale bars represent 200 µm. D, DHM phase images of PDAC cells. Scale bars indicate 10 µm. E, Accuracy for separating epithelial and mesenchymal PDAC cells using different classification methods: random forest (RF), support vector machine (SVM), K-nearest neighbors (K-NN) and neuronal network (NN). F, Unsupervised clustering of DHM phase images derived from cells of the C2b and the C1 cluster visualized using the UMAP plot. G, Unsupervised clustering of individual PDAC lines based on DHM phase images and visualized using UMAP plots H, Hierarchical clustering of epithelial and mesenchymal PDAC cells based on the 26 most different ResNet18 and morphological features. I, Evaluation of intra-cell line heterogeneity using single cell distance to cluster centroid. Kruskal-Wallis test, ****p<0.0001.

In order to use DHM as a tool to investigate the phenotype of an unknown sample, it is key to identify different morphological subpopulations within one sample. Thus, we performed a spike experiment, mixing an epithelial (9591) as well as a mesenchymal cell line (16992) in different known concentrations (Figure 6A). The algorithm was trained using pure populations of both lines and the mixed populations were afterwards tested. The results of the DHM measurement significantly correlated with the calculated concentrations with a maximum deviation of 3% in the sample of 25% epithelial mixed with 75% mesenchymal cells (Figure 6B). These data clearly demonstrate the robustness of this technique in order to identify subpopulations of varying morphologies within one sample. This in turn is an important factor, as intra- as well as intertumoral heterogeneity is highly abundant in PDAC, which can be recorded on a single cell level using our DHM approach.

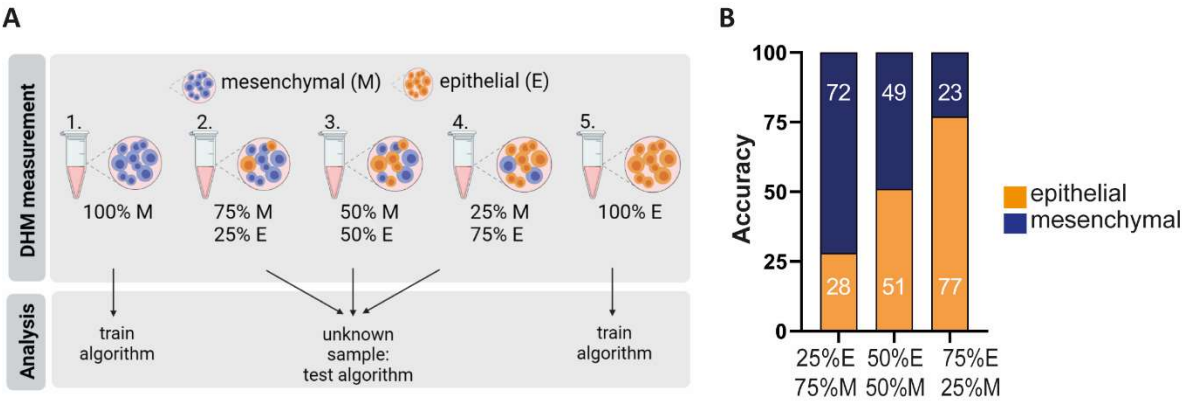

Figure 6. Detecting morphological subpopulations in unknown samples.
A, Schematic illustration of the spike experiment setup. B, Accuracies obtained using Random Forest classification when trained with 100% epithelial and 100% mesenchymal PDAC cells.

6.1.6 Phenotypic subtyping of characterized human PDAC cells

In parallel, we have performed the same approach using human established and well-characterized PDAC cell lines. When cultured in 2D, PatuS and HPAC exhibited an epithelial morphology with colony formation and cell-cell contact while PSN-1, DanG and PatuT showed a spindle-like single cell growth pattern (Figure 7A). When applying the well-known PDAC subtyping methodologies to these cell lines, we did not obtain definite subtypes for all cell lines (Figure 7B). While PatuS as well as PatuT and DanG were clustered into the classical and the quasi-mesenchymal PDAC subtype, respectively, HPAC and PSN-1 failed to be assigned to either subtype suggesting either a hybrid-like phenotype or a failure of subtyping approaches as Topham et al. demonstrated (Topham et al., 2021). However, when we measured these cells with DHM, we obtained a clear separation of the cells with epithelial and quasi-mesenchymal morphology (Figure 7C). Hierarchical clustering based on DHM phase images clearly separated HPAC and PatuS from PatuT, PSN-1 and DanG, similar to the morphology observed in adherent cell culture (Figure 7D). Random Forest classification and UMAP clustering further verified this grouping as the epithelial and quasi-mesenchymal cell lines could be separated with an accuracy of almost 90% with a clear left shift in the quasi-mesenchymal lines (Figure 7E, F). Interestingly, levels of intra-cell line heterogeneity differed independently of cellular morphology with PatuS and PatuT showing the lowest and PSN1 showing the highest intratumoral heterogeneity score (Figure 7G, H).

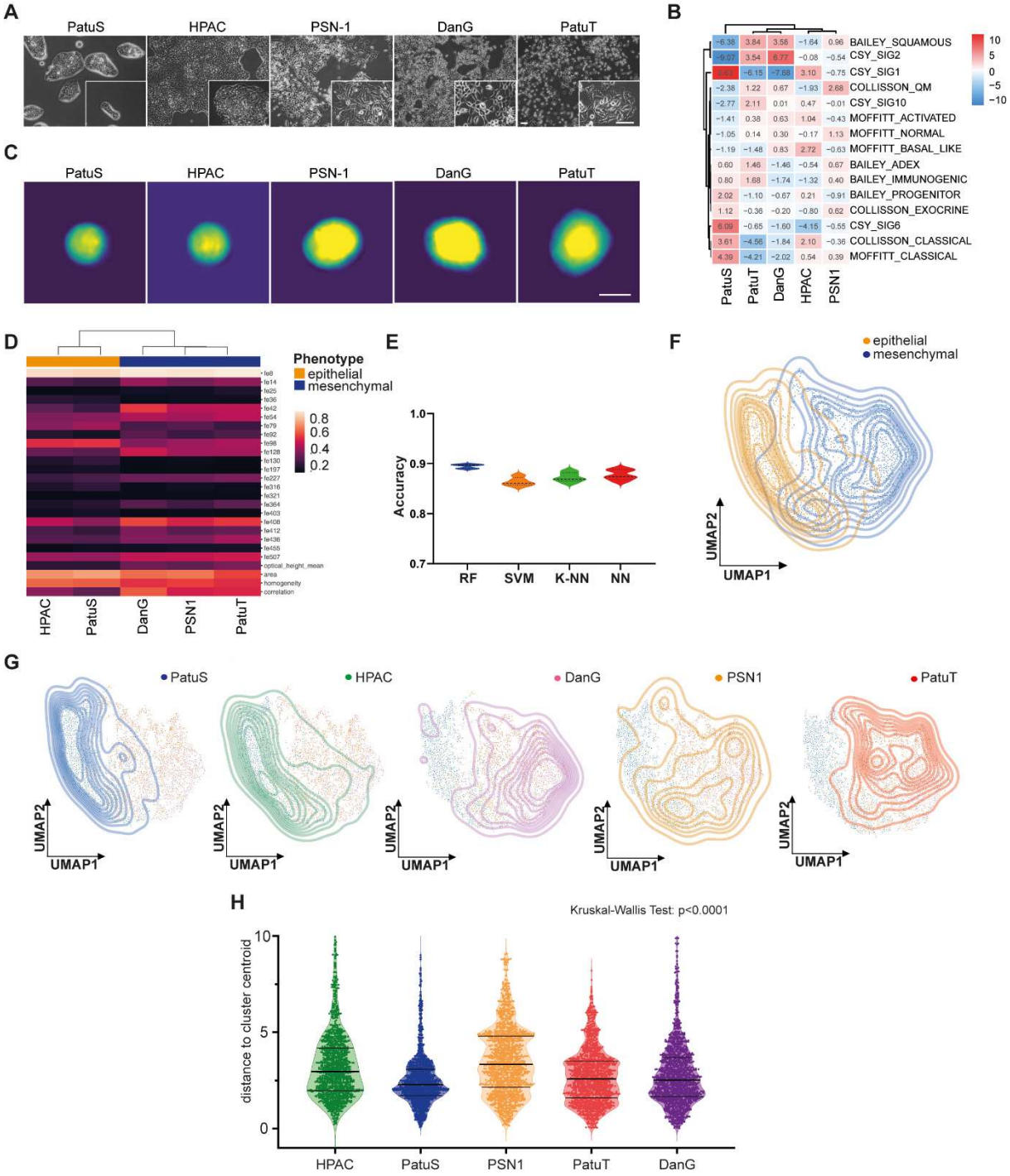

Figure 7. Label-free clustering of epithelial and mesenchymal human PDAC cells.
A, Phase contrast images of human PDAC cells. Scale bars represent 200 µm. B, Molecular subtype classifier gene sets applied to transcriptomic profiles of established PDAC cells. C, DHM phase images of PDAC cells. Scale bars indicate 10 µm. D, Hierarchical clustering of epithelial and mesenchymal human PDAC cells based on the most different Resnet18 and morphological features. E, Accuracy for separating epithelial and mesenchymal PDAC cells using different classification methods: random forest (RF), support vector machine (SVM), K-nearest neighbors (K-NN) and neuronal network (NN). F, Unsupervised clustering of epithelial (PatuS and HPAC) versus mesenchymal (PSN1, DanG and PatuT) PDAC cells based on DHM phase images and visualized using the UMAP plot. G, Unsupervised clustering of individual cell lines based on DHM phase images and visualized using UMAP plots.

6.1.7 Phenotypic characterization of patient-derived organoid heterogeneity

In the past decade, 3D model systems such as organoid cultures have been extensively studied since they more closely recapitulate human physiology and better depict heterogeneity compared to 2D cell cultures (Kim et al., 2020). Indeed, Juiz et al. performed scRNAseq of six PDAC PDOs and grouped their transcriptomic profiles into four clusters illustrating different levels of EMT. Interestingly, these clusters were found throughout the whole cell line panel. However, the cell count of each cluster was different between the PDO lines representing a high degree of intratumoral heterogeneity in these organoids (Juiz et al., 2020). Therefore, we next used six different PDO lines in order to identify inter- and intratumoral heterogeneity on a single cell level using DHM in a clinically relevant setting. When grown as organoids, ID188, ID203, ID208 and ID226 showed a lumen-filling growth pattern, while ID211 and ID250 grew with hollow lumen structures (Figure 8A). Transcriptional subtyping of PDO bulk RNA sequencing clustered them into 2 groups, however only ID211 was characterized as clearly classical and ID250 as quasi-mesenchymal. For the rest of the lines no definite subtype could be assigned (Figure 8B). Once PDOs were dissociated to a single cell suspension, DHM-based phenotyping did not predict a clear separation of the PDO lines into classical and quasi-mesenchymal based on single cell phase images using hierarchical clustering (Figure 8C, D) but rather demonstrated high inter- and intratumoral heterogeneity in the corresponding UMAP analysis (Figure 8E). Indeed, when quantifying the intra-cell line heterogeneity, we found significantly different levels in the six lines. While ID211 and ID226 showed the lowest heterogeneity within their respective cluster, ID208 showed by far the highest intratumoral heterogeneity (Figure 8F).

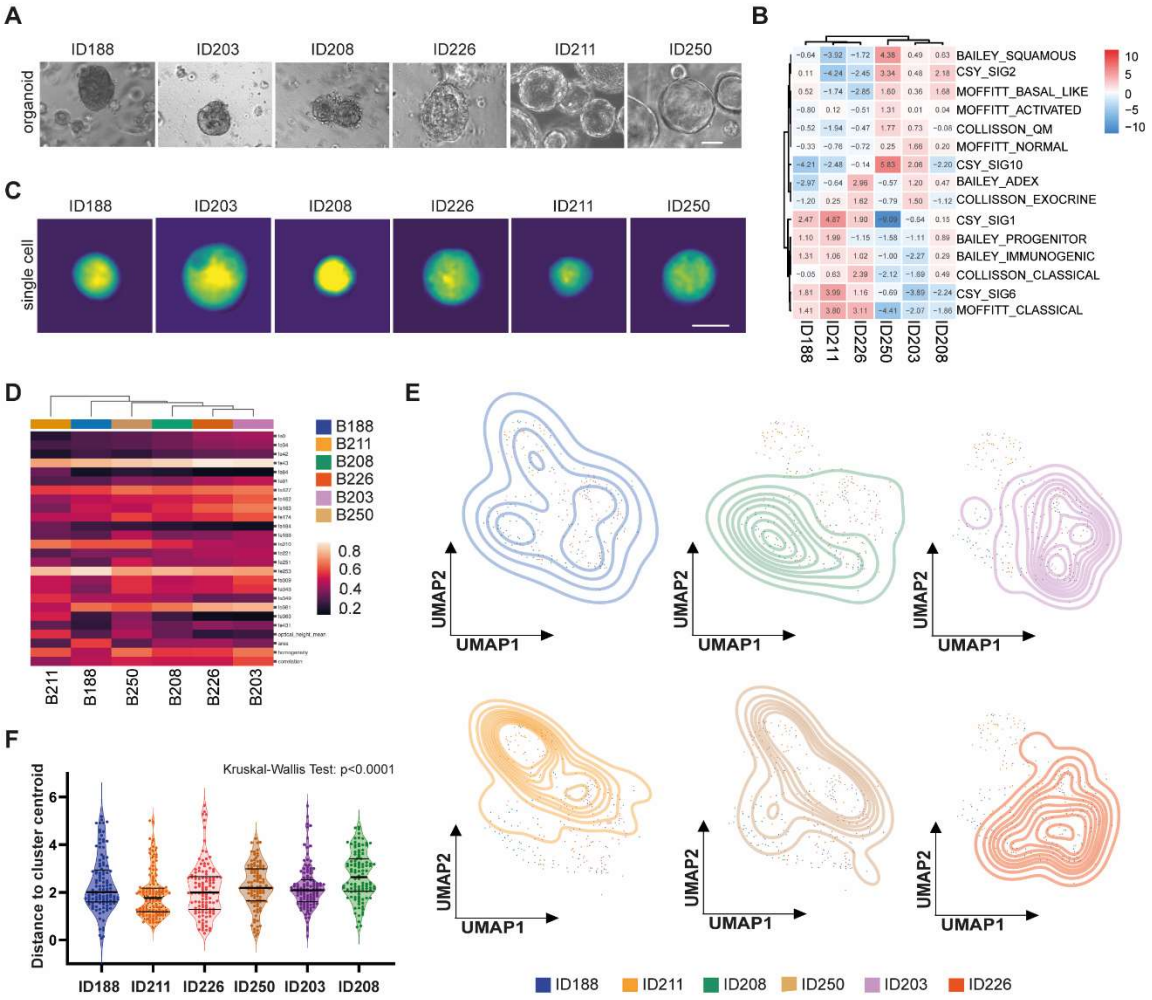

Figure 8. Detecting single cell tumor plasticity and heterogeneity in patient-derived organoids of PDAC.

A, Phase contrast images of patient-derived organoids (PDOs). Scale bar represents 200µm. B, Molecular subtype classifier gene sets applied to transcriptomic profiles of PDOs. C, DHM phase images of PDOs. Scale bars indicate 10 µm. D, Hierarchical clustering of PDOs based on the most different morphological+ResNet18 features. E, Unsupervised clustering of individual PDAC organoid lines based on DHM phase images and visualized using UMAP plots. F, Evaluation of intra-organoid line heterogeneity using single cell distance to cluster centroid. Kruskal-Wallis test, ****p<0.0001.

6.1.8 Detecting oncogene-induced changes in morphology

Differentiation and plasticity are indispensable parameters of PDAC characterization. However, oncogenic activity is the major factor for PDAC onset and progression and is influencing cellular morphology, as well. In particular, oncogene-induced senescence has been considered a potent anticancer mechanism in precursor lesions to prevent replication of malignant cells (Herranz and Gil, 2018) and thus might serve as diagnostic parameter for early detection. Senescence leads to cell cycle exit, morphological changes, chromatin remodeling as well as secretion of proinflammatory factors. Especially the change in phenotype might be detectable using DHM and thereby we might be able to use DHM as a diagnostic tool. For that reason, we used a doxycycline-inducible model system in HPDECs, in which a major hallmark of PDAC – the *KRAS*^{G12D} mutation, is activated upon treatment (Figure 9A). In order to potently activate *KRAS*^{G12D}, cells were treated for 24h with 125 ng/mL doxycycline. The activation of *KRAS*^{G12D} resulted in a senescent phenotype with increased lysosomal content, which returned to its baseline phenotype after a doxycycline withdrawal for 7 days (Figure 9B). The senescent phenotype of the cells was validated by assessing the senescence-associated β-galactosidase activity. While cells in the baseline and washout state did not exhibit high β-galactosidase activity, HPDECs with *KRAS*^{G12D} activation showed strongly increased levels (Figure 9C). In contrast to our expectations, the algorithm could predict only a difference in phenotype between with and without doxycycline-treated cells of approximately 78% upon oncogene induction, which was similar (82%) when we included also the doxycycline washout cells (Figure 9D, F). Using UMAP clustering of DHM phase images, we still observed a shift in morphology upon doxycycline-treatment, which returned to baseline after doxycycline-washout (Figure 9G). However, for validation purposes we additionally used HPDECs with doxycycline-inducible EGFP instead of *KRAS*^{G12D}. Phase contrast images as well as phase images of DHM demonstrated that doxycycline itself did not induce the senescent phenotype noticed upon *KRAS*^{G12D} activation since no difference in UMAP clustering and classification was observed (Figure 9H, I, J). Importantly, we observed a heterogeneous induction of EGFP in our IF staining suggesting different expression intensities of *KRAS*^{G12D} on a single cell level, leading to a heterogenous cell population (Figure 9H). This in turn explains the relatively low differentiation rate of only 78% upon *KRAS*^{G12D} activation and proves the propriety of our DHM system.

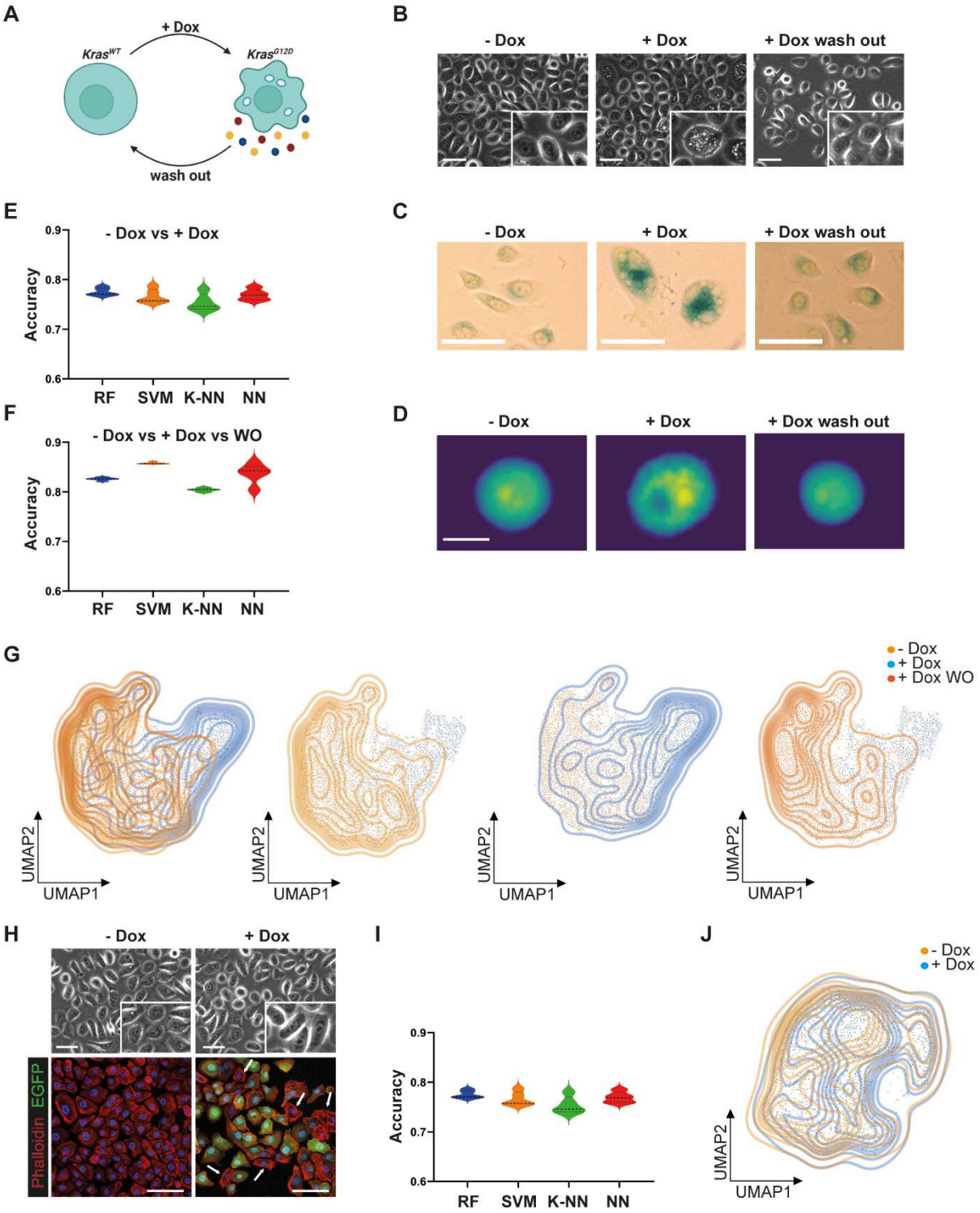

Figure 9. Detection of oncogenic activation of *KRAS* in HPDECs using DHM.
A, Schematic illustration of the doxycycline-inducible Tet-On system. B, Phase contrast images of control HPDECs and cells after doxycycline treatment and washout. Scale bar represents 50µm. C, β-Galactosidase staining of cells in doxycycline untreated, treated or washout stage. Scale bar represents 50µm. D, DHM-derived phase images of HPDECs. Scale bar represents 10µm. E, Accuracy for separating HPDECs with and without doxycycline using different classification methods: random forest (RF), support vector machine (SVM), K-nearest neighbors (K-NN) and neuronal network (NN). F, Accuracy HPDECs with and without doxycycline and the washout using different classification methods: random forest (RF), support vector machine (SVM), K-nearest neighbors (K-NN) and neuronal network (NN). G, Unsupervised clustering of HPDECs based on DHM phase images and visualized using UMAP plots. H, Phase contrast images (upper panel) and immunofluorescence staining (lower panel) of

HPDECs with doxycycline-inducible EGFP. Scale bars represent 50µm (up) and 100µm (down). Arrows indicate cells lacking EGFP expression. I, Accuracy for separating HPDECs (GFP-inducible) with and without doxycycline using different classification methods: random forest (RF), support vector machine (SVM), K-nearest neighbors (K-NN) and neuronal network (NN). J, Unsupervised clustering of HPDECs (GFP-inducible) based on DHM phase images and visualized using UMAP plots.

6.2 Treatment-induced vulnerabilities in murine PDAC cells

Research in the past mainly focused on the molecular effects of gemcitabine treatment, since it has been standard of care for many decades. Research groups were able to show that particularly EMT and the differentiation status of a tumor plays an important role in the response towards chemotherapy. However, the gold standard changed and therefore the necessity arises to study chemoresistance upon FFX as well as Gem/nP administration.

6.2.1 Phenotype-specific response rate towards chemotherapeutic treatment

First, we used the well characterized cell lines from the C2b as well as C1 Cluster in order to investigate phenotype-specific response towards FFX as well as Gem/nP. Single drug treatments of all cytostatic components of FFX revealed an increased sensitivity in the mesenchymal cells of the C1 Cluster compared to the epithelial cells with partially significantly reduced area under the curve as well as IC_{50} values (Figure 10A, B). Combining 5-FU, Irinotecan and Oxaliplatin in a ratio comparable to the one in clinical routine yielded similar results as the single drug treatments with increased resistance in the epithelial phenotype (Figure 10 C, D, E).

When treating the cells with gemcitabine only, mesenchymal cells showed again an increased sensitivity compared to the epithelial cells. Strikingly, paclitaxel as single agent showed the opposite result with significantly reduced area under the curve and IC_{50} value in the epithelial versus the mesenchymal lines (Figure 11A, B). When combining both cytostatic components based on the clinical ratio with 1µM of gemcitabine plus 0.125µM paclitaxel, the effects of paclitaxel outweigh the ones of gemcitabine (Figure C, D, E). Even though the concentration of gemcitabine is 8-way higher than paclitaxel, the epithelial cells again showed a significantly increased sensitivity compared to the mesenchymal cells.

This in turn shows a phenotype-specific response towards FFX and Gem/nP with mesenchymal cells being more sensitive towards FFX, but more resistant towards Gem/nP and epithelial cells acting vice versa.

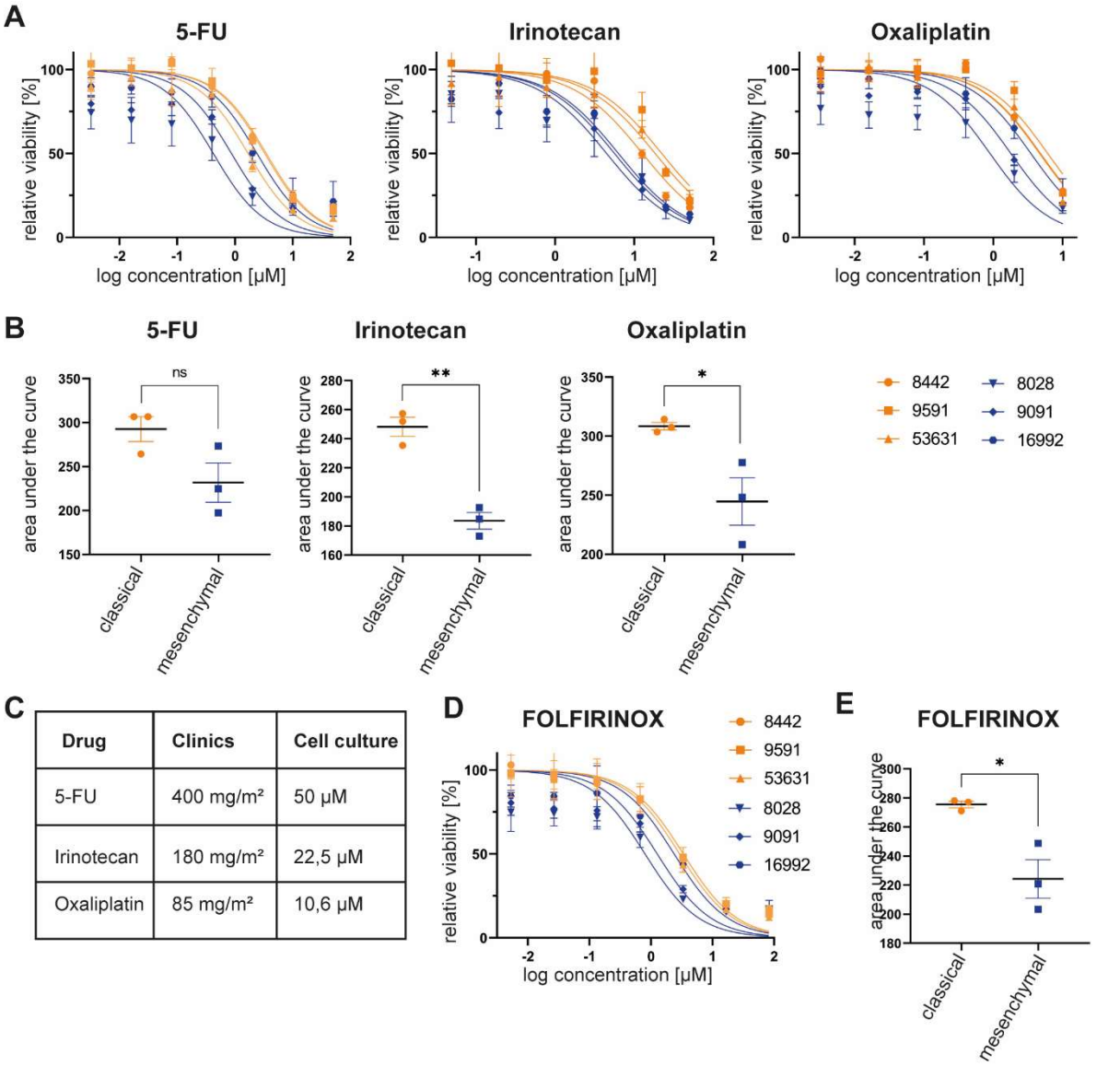

Drug	Clinics	Cell culture
5-FU	400 mg/m²	50 µM
Irinotecan	180 mg/m²	22,5 µM
Oxaliplatin	85 mg/m²	10,6 µM

Figure 10. Increased sensitivity towards FFX treatment in mesenchymal cells.
A, Single treatment of 5-FU, Irinotecan and Oxaliplatin in epithelial and mesenchymal cells. B, Corresponding area under the curve for all single treatments. Unpaired student´s t-test C, Drug concentrations in clinic and research for FFX. D, FFX drug response curve. E, Corresponding area under the curve for FFX treatment.

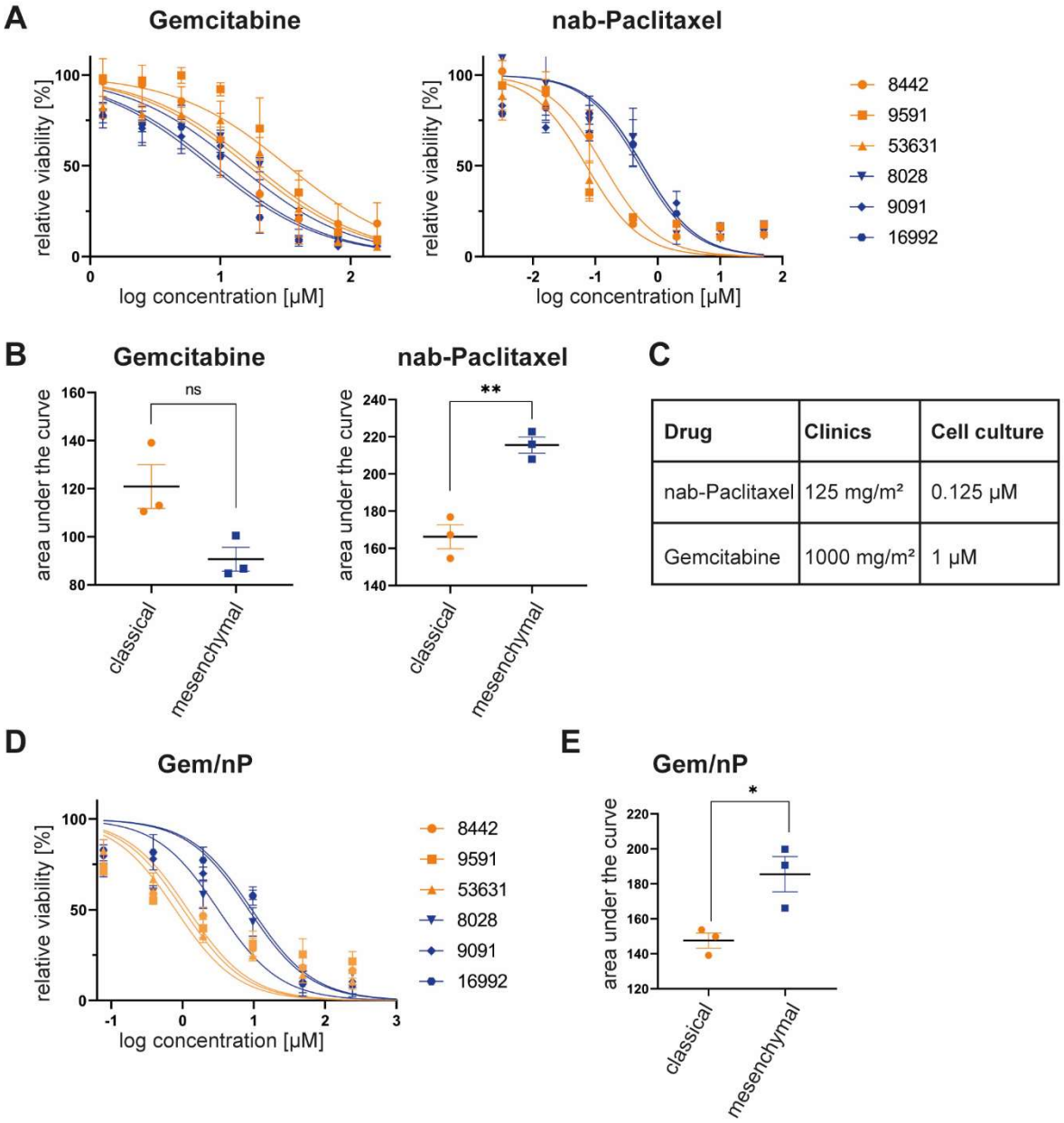

Figure 11. Increased sensitivity towards Gem/nP treatment in epithelial cells.
A, Single treatment of gemcitabine and paclitaxel in epithelial and mesenchymal cells. B, Corresponding area under the curve for all single treatments. Unpaired student´s t-test C, Drug concentrations in clinic and research for Gem/nP. D, Gem/nP drug response curve. E, Corresponding area under the curve for Gem/nP treatment.

6.2.2 Molecular mechanisms contributing to chemoresistance in PDAC cells

In order to analyze molecular changes and adaption processes occurring upon FFX and Gem/nP treatment, we have treated the murine epithelial and mesenchymal PDAC cells for 72h with their respective IC_{50} concentration of either drug combination. Surviving cells were recovered for additional 72h in normal medium in a wash out phase to differentiate between temporary and prolonged effects (Figure 12A). Different analyses were performed in order to obtain detailed insight into the individual mechanisms of chemoresistance, mainly focusing on FFX treatment. A time-lapse proteomics analysis of one cell line (9591) over 72h of FFX treatment and 48h of wash out period was performed in order to find the appropriate time points for later RNA sequencing and proteomics analysis (Figure 12B). The expression of most proteins was increased over time, however reached the plateau at 72h of FFX treatment and remained stable until the end of the wash out suggesting these time points for further analyses. Interestingly, epithelial cells responded phenotypically stronger compared to mesenchymal cells upon FFX treatment as well as wash out phase (Figure 12C). While mesenchymal cells barely change upon treatment, epithelial cells lost their cell-cell contact and acquired an EMT-like morphology. In contrast, neither epithelial nor mesenchymal PDAC cells changed in their respective morphology upon 72h of Gem/nP treatment and the wash out period (Figure 12C). Since Chan-Seng-Yue et al. found a reduction of mutant *KRAS* from $KRAS^{Ma}$ to $KRAS^{Ba}$ upon Gem/nP treatment to be the reason for the subtype switch from basal-like to classical in liver metastasis (Chan-Seng-Yue et al., 2020), we analyzed the mutant allele frequency of $Kras^{G12D}$ using digital droplet PCR for all time points and treatment regimens (Figure 12D). However, we could not observe any treatment-induced changes of $Kras^{G12D}$ in any cell line or treatment regimen. A possible explanation could be the short time period (72h) of chemotherapeutic treatment, which might not be sufficient to induce selective processes that are comparable to clinical chemotherapy administration.

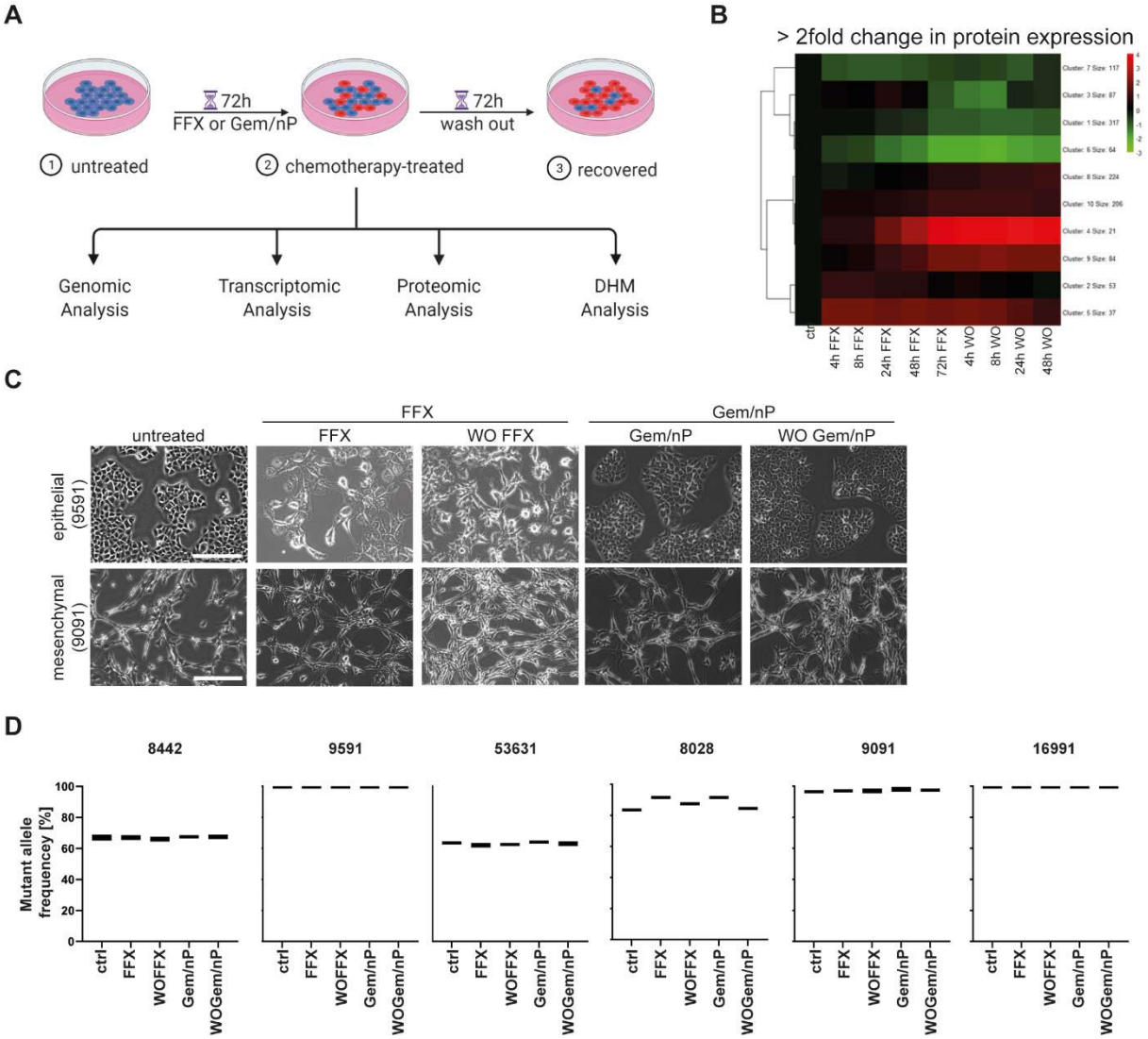

Figure 12. Molecular and phenotypic characterization of chemotherapy-treated PDAC cells.
A, Schematic illustration of the experimental workflow. B, Hierarchical clustering of proteins with a >2fold change in protein expression upon time-lapse FFX treatment. C, Representative images of epithelial and mesenchymal PDAC cells upon FFX or Gem/nP treatment and wash out. D, Mutant allele frequency of *Kras*^{G12D} obtained by digital droplet PCR upon FFX or Gem/nP treatment and wash out.

As mentioned above, RNA sequencing of three epithelial and mesenchymal PDAC lines in an untreated, FFX- or Gem/nP-treated condition or after the wash out period was performed. A first genome-wide differential gene expression analysis was conducted to discover global effects of either treatment regimen compared to the control cells irrespective of their cellular phenotype (Figure 13A). Strikingly, Gem/nP treatment itself did not induce major changes on mRNA level (88 genes different compared to control), which was in line with Figure 12C where no morphological changes were observed upon Gem/nP. However, a delayed response was detected after the wash out period on mRNA level with 2693 genes in total differentially expressed in Gem/nP wash out compared to the control. Highly upregulated pathways upon FFX treatment include p53 signaling, hypoxia as well as PI3K signaling, whereas cellular senescence as well as the response to external stimuli was downregulated (Figure 13B). Gem/nP treatment resulted in increased lipid metabolism with fatty acid oxidation and cholesterol biosynthesis, while glucose metabolism as well as cell cycle and cell growth were downregulated (Figure 13B). Although this was a phenotype-independent gene expression analysis, an augmented gene expression upon FFX was observed in a phenotype-dependent manner.

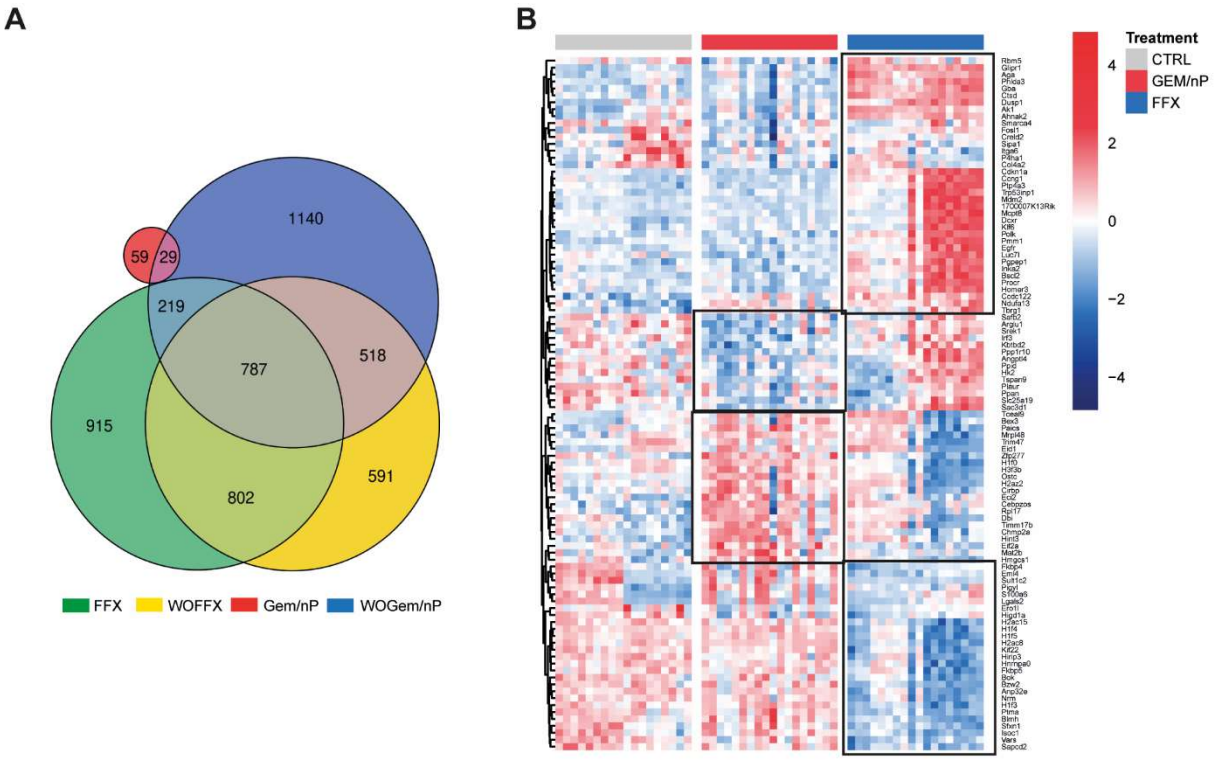

Figure 13. Genome-wide differential gene expression analysis upon FFX and Gem/nP treatment. A, Genome-wide differential gene expression of PDAC cells upon FFX or Gem/nP treatment and their respective wash out compared to their untreated counterparts. B, Hierarchical clustering of genome-wide differential gene expression analysis (top 100 differentially expressed genes) of control, FFX- and Gem/nP-treated PDAC cells.

In order to gain insight into specific pathways that are up- or downregulated upon either treatment option, we performed a phenotype-specific GSEA of both transcriptomic and proteomic data sets. As already mentioned, both phenotypes actually share most of the molecular changes during FFX treatment as well as the wash out phase, however to a variable extent with epithelial cells reacting the most (Figure 14C,D).

For instance, metabolic pathways such as glycolysis, fatty acid metabolism, OXPHOS and hypoxia as well as processes involved in epithelial plasticity like EMT and TGF-β signaling were highly upregulated upon chemotherapeutic treatment. In contrast, the expression of genes involved in cell cycle and proliferation such as E2F targets, mitotic spindle and G2M checkpoint were highly downregulated upon chemotherapy indicating good treatment efficacy. Interestingly, pathways involved in immune response s, ch as generation of reactive oxygen species (ROS) tumor necrosis factor-α (TNFA), interleukin 2 and 6 (IL-2, IL-6) as well as IFN-γ signaling were highly upregulated in epithelial and mesenchymal PDAC cells upon treatment. Additionally, Kras, PI3K and p53 signaling were upregulated, while the mammalian target of rapamycin (mTOR) C1, Myc and Wnt signaling were highly downregulated upon chemotherapy. The majority of pathways was uniformly altered, independent of phenotype or treatment regimen. However, Gem/nP did not induce EMT and TGF-β signaling as much compared to FFX treatment. Additionally, p53 and PI3K signaling were downregulated in epithelial PDAC cells upon Gem/nP, while mesenchymal PDAC cells increased mTORC1 signaling. Moreover, mesenchymal PDAC cells did not produce ROS upon Gem/nP as they did upon FFX. In sum, pathways involved in metabolism, plasticity, immune response as well as oncogenic signaling were highly upregulated upon FFX and Gem/nP often with a prolonged effect even in the wash out cells.

Slight discrepancies between mRNA and protein expression is typically due to differential regulatory processes during transcription and translation or epigenetic mechanisms.

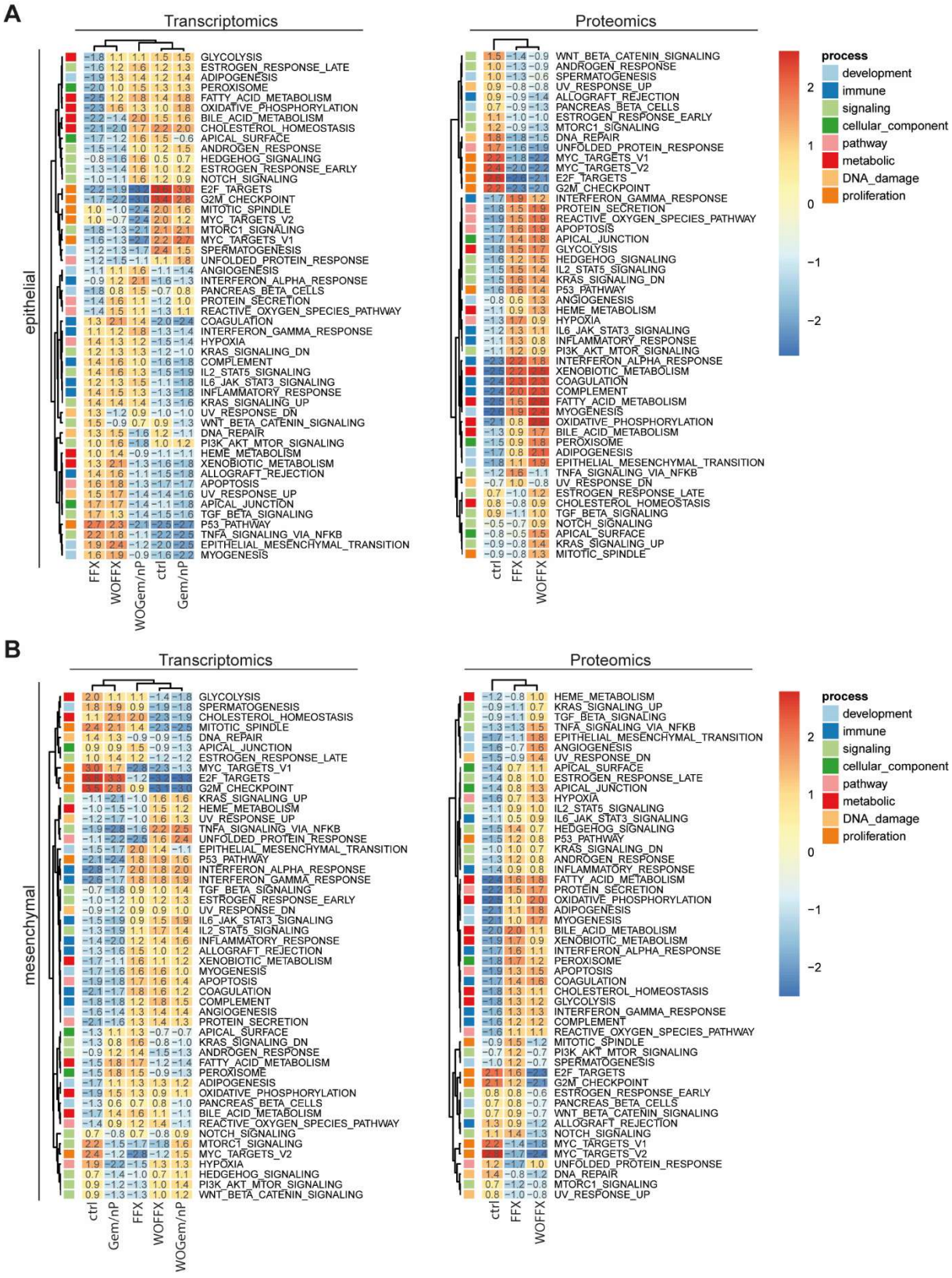

Figure 14. Gene set enrichment analysis upon FFX and Gem/nP treatment.
Normalized enrichment score matrix with HALLMARK gene sets in rows and subtype- and treatment-specific one versus rest signatures in columns of epithelial (A) and mesenchymal (B) PDAC cells. Data retrieved from transcriptomic (left) and proteomic (right) analysis.

In order to find potent targets for a combinatorial or sequential treatment regimen with FFX, we actively included the wash out time point into our RNA sequencing analysis. Since the status of tumor differentiation and subtype is mainly unclear in clinical routine, we decided to identify actionable targets, which were uniformly up- or down-regulated in epithelial as well as mesenchymal cells for a longer period. Therefore, genes with a log2 fold change of ≥1 or ≤ -1 as well as an FDR q-value of ≤ 0.05 between FFX and WOFFX compared to control were included into the analysis. Additionally, only genes with log2foldchange <1 and > -1 as well as FDR q-values > 0.05 between FFX and WOFFX were included, thus considering only targets with sustained effects upon wash out of FFX (Figure 15A). Here, we detected nine final hits meeting all abovementioned criteria and their respective gene expression pattern over time is illustrated (Figure 15B, C). These top genes are implicated in very distinct molecular pathways such as metabolism or immune response, particularly *Ddit4l*, *Ifit3* or *Egln3* suggesting high relevance for potential resistance mechanisms (Figure 15D).

A

Comparison	log2 fold change	FDR q-value
FFX vs control	≥ 1 or ≤ -1	≤ 0.05
WOFFX vs control	≥ 1 or ≤ -1	≤ 0.05
FFX vs WOFFX	< 1 and > -1	> 0.05

B

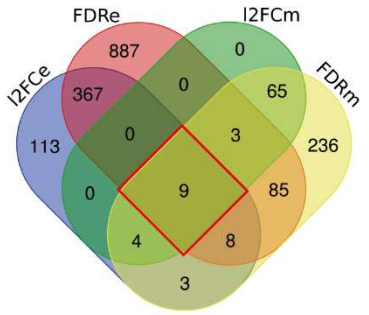

C

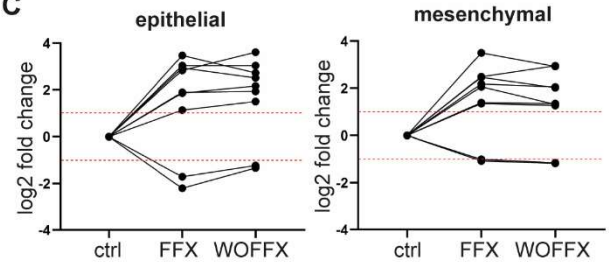

D

Gene	Pathway
Sytl1	Vesicle trafficking
Gbp8	GTPase activity
Gpx3	Glutathione peroxidase
Ddit4l	mTOR signaling
Ifit3	Interferon response
Serpinb9b	Serine proteinase inhibition
Tcn2	Vitamin B12 metabolism
H2ac13	Histones
Egln3	HIF1 metabolism

Figure 15. Time-dependent gene expression to identify actionable targets upon FFX treatment.
A, Inclusion criteria for genes significantly changed upon FFX and in wash out period. B, Venn diagram visualizing the number of genes identical between different conditions. e = epithelial, m = mesenchymal, l2FC = log2fold change, FDR = FDR q-values. C, Gene expression time course of the 9 top hits identified in B. D, Gene symbols and corresponding pathways of 9 top hits.

6.2.3 FFX-induced changes in plasticity and heterogeneity

In order to analyze single cell phenotypic differences in a label-free fashion, we measured the six cell lines in the untreated (control), FFX-treated and FFX wash out condition using our DHM approach (Figure 16A). Hierarchical clustering revealed acquired similarities as well as differences between the cell lines upon FFX induction (Figure 16B). We have already shown a tight relationship between 8442 and 8028 with a rather hybrid-like phenotype in the control setting (Figure 5G), however, upon FFX treatment both cell lines phenotypically drifted apart and acquired further phenotypic characteristics of the opposing transcriptomic subtype. While 8442 was tightly related to the mesenchymal line 9091 upon FFX treatment, 8028 morphologically behaved similar to the epithelial lines 9591 and 53631 confirming them as outliers of their transcriptomic cluster again. Additionally, DHM enabled a differentiation between untreated and FFX-treated cells with an accuracy of about 87% when compared in a cell line- and phenotype-independent fashion using Random Forest classification (Figure 16C). When plotted using UMAP clustering we observed a right shift in the FFX and the FFX wash out cells indicating a certain degree of EMT occurring upon FFX treatment (Figure 16D), which was observed in transcriptomic and proteomic profiling as well (Figure 14A, B).

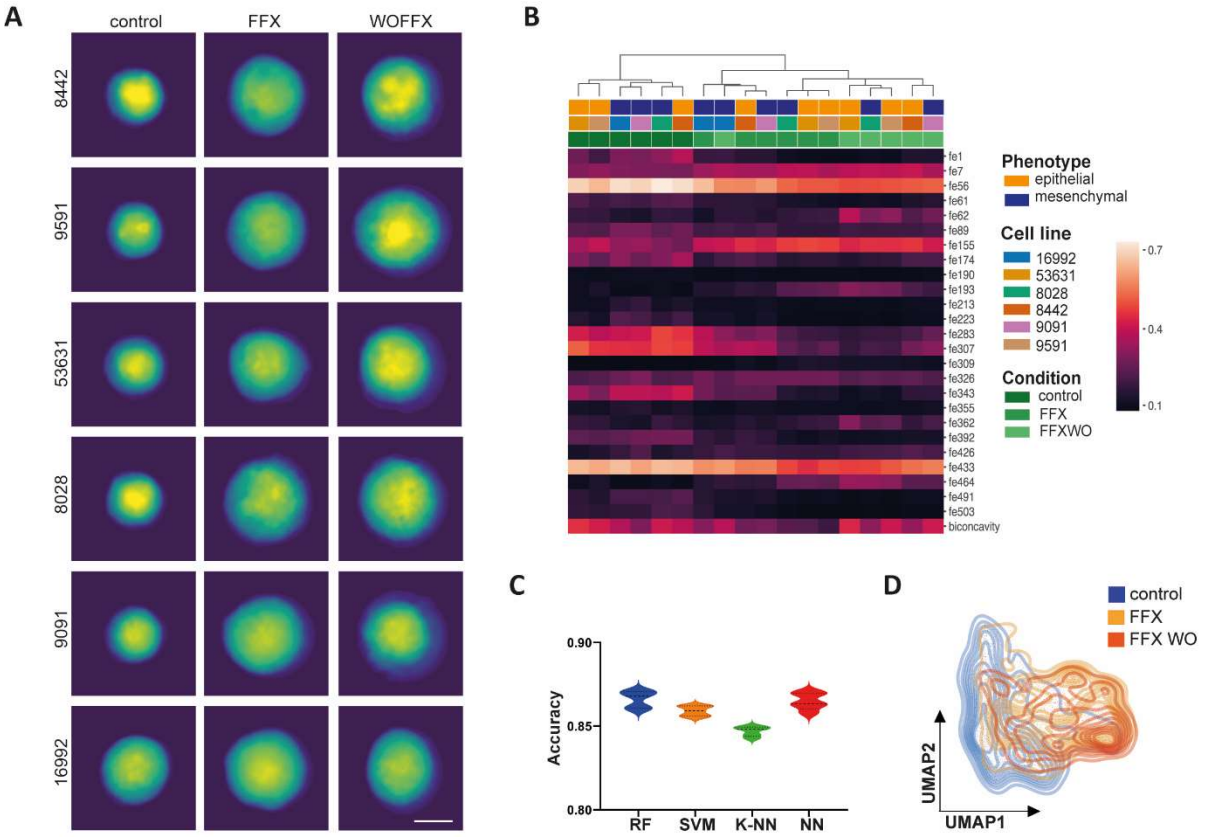

Figure 16. DHM-based separation of PDAC cells upon FFX treatment.
A, DHM phase images of murine PDAC cells untreated, FFX treated or after FFX washout. Scale bars indicate 10 µm. B, Hierarchical clustering of DHM phase images derived from murine PDAC cells in untreated, FFX treated or FFX wash out condition based on the most different Resnet18 and

morphological features. C, Accuracy for separating untreated versus FFX treated PDAC cells using different classification methods: random forest (RF), support vector machine (SVM), K-nearest neighbors (K-NN) and neuronal network (NN). D, Unsupervised clustering of murine PDAC cells untreated, FFX treated or after FFX washout based on DHM phase images and visualized using the UMAP plot.

Next, we performed a cell line-specific UMAP clustering to illustrate the single cell behavior and EMT status of individual lines upon FFX (Figure 17A). While we detected a clear right shift towards a more mesenchymal phenotype for the lines 8442, 9591, 53631 and 8028 in the treated and wash out condition, half of the population of 9091 and 16992 remained rather unaffected by FFX treatment. In order to validate these DHM results we compared the ssEMT score of the HALLMARK gene set retrieved from transcriptomic and proteomic profiling between the control, FFX and wash out FFX conditions. As shown in Figure 14, PDAC cells from both transcriptomic clusters (C2b and C1) have an upregulation of the EMT gene set. However, individual cell lines exhibited different levels of EMT upon FFX (Figure 17B). On mRNA level, 53631 showed the highest EMT score of the epithelial lines, which was detected in the cell line-specific UMAP clustering, as well. Interestingly, the mesenchymal line 16992 showed a significant increase in the EMT score upon FFX too, which, however, cannot be fully confirmed on single cell level as half of the population remain rather unaffected. On protein level, the effects of FFX treatment on the EMT score were augmented in all lines. Nevertheless, 53631 and 16992 were the lines with the greatest change in the ssEMT score upon FFX in their respective transcriptomic cluster. The discrepancy between transcriptomics as well as proteomics and DHM-based phenotyping might be explained by bulk sequencing and single cell analysis, respectively.

Interestingly, when analyzing the single cell distance to the cluster centroid, we found a subtype-dependent change in intratumoral heterogeneity upon FFX administration (Figure 17C). While the intratumoral heterogeneity significantly decreased in the epithelial lines 9591 and 53631 in the FFX and the wash out cells, it significantly increased in the mesenchymal lines 9091 and 16992 upon chemotherapy. Again, the line 8442 behaved similar to the mesenchymal lines showing an increase in intratumoral heterogeneity upon FFX compared to its untreated controls.

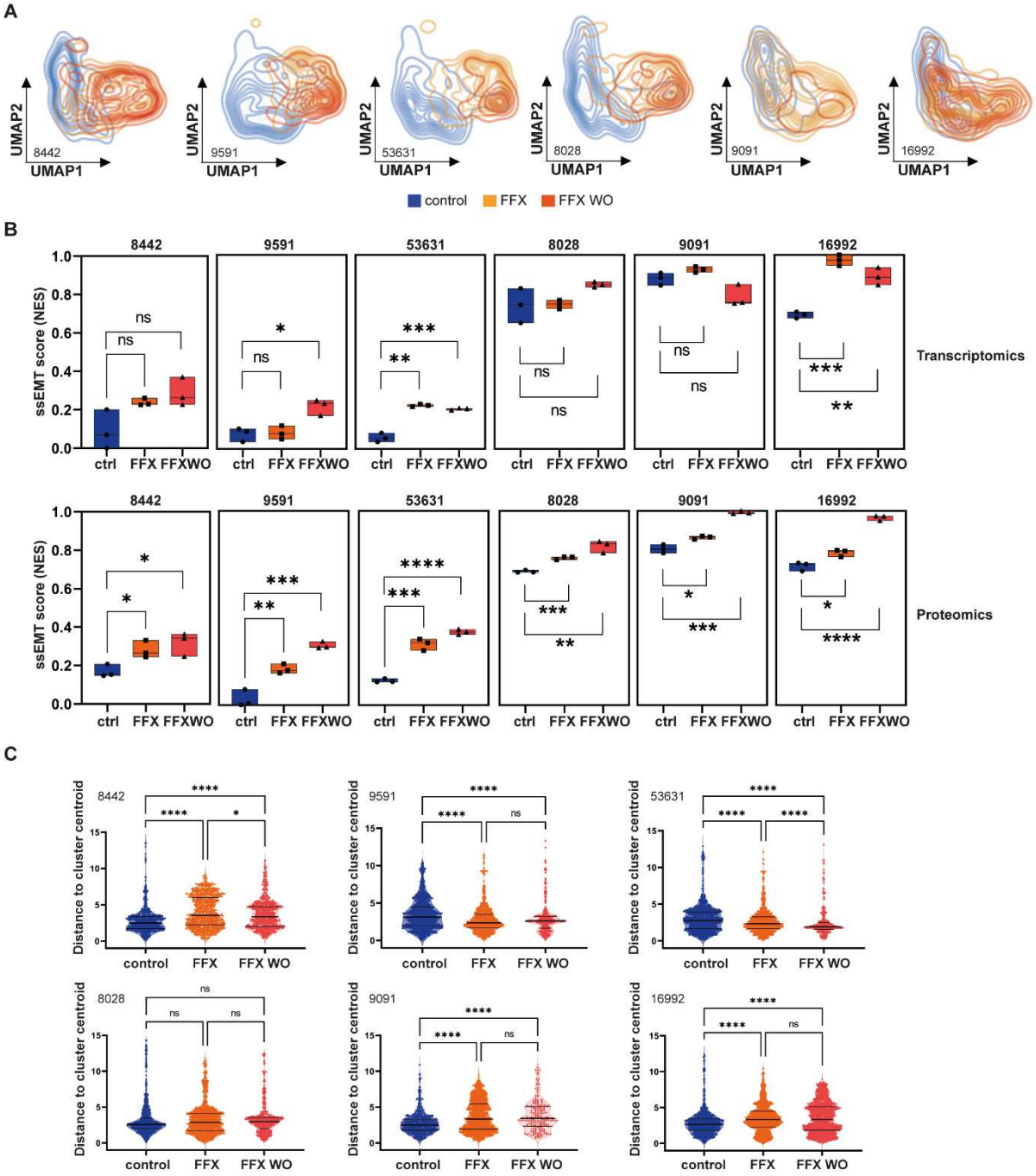

Figure 17. Single sample analysis of plasticity and intratumoral heterogeneity upon FFX treatment.

A, Unsupervised clustering different conditions in the individual cell lines based on DHM phase images and visualized using UMAP plots. B, Single-sample normalized enrichment scores (NES) of the HALLMARK_EPITHELIAL_MESENCHYMAL_TRANSITION gene set (ssEMT score) retrieved from RNA sequencing (upper panel) and proteomic analysis (lower panel). Unpaired student´s t test: ns = not significant, *p<0.05, **p<0.01, ***p<0.001 and ****p<0.0001. C, Evaluation of intra-cell line heterogeneity upon FFX treatment using single cell distance to cluster centroid. Kruskal Wallis test: ns = not significant and ****p<0.0001.

6.3 Treatment-induced vulnerabilities in patient-derived PDAC cells

6.3.1 Generation of chemotherapy-naïve and -exposed patient-derived models

In order to translate our findings into clinical research, we compared the tumor of one PDAC patient before and after neoadjuvant FFX treatment (4 cycles) using a multi-dimensional workflow for in-depth characterization including clinical, genomic, transcriptomic, functional and DHM analysis (Figure 18A). The patient was diagnosed with borderline resectable PDAC in March 2019 and was therefore treated with 4 cycles of neoadjuvant FFX prior to surgical resection. After 4 cycles of adjuvant FFX administration, he showed a partial response, however in May 2020, he relapsed with liver metastasis as well as peritoneal carcinosis and died 486 days after diagnosis (Figure 18B). The patient received ^{18}F-FDG-PET before and after one cycle of FFX induction. Although tumor size did not change upon treatment, the glucose uptake (SUV_{max}) markedly decreased from 5.4 to 4 (Figure 18C). Histologically, the pre-FFX (ID188) and the post-FFX (ID211) biopsies showed a well to moderate tumor differentiation (Figure 18D). Additional biopsies at both time points were used for generating 2D as well as 3D cell lines, ID188 and ID211, which were then subjected to in-depth molecular and functional characterization. Interestingly, while organoids of ID188 exhibited a lumen-filling growth pattern, ID211 organoids formed a hollow lumen as shown in phase contrast as well as confocal imaging of the actin filaments and HE staining (Figure 18E, F). Also, 2D cells of ID188 exhibited a more mesenchymal-like phenotype compared to ID211, which showed more colony formation (Figure 18E). Moreover, ID188 expressed highly ID211 demonstrated a significant increase in the proliferation rate upon FFX treatment compared to ID188 indicating selection processes or escape mechanisms occurring upon chemotherapy (Figure 18F).

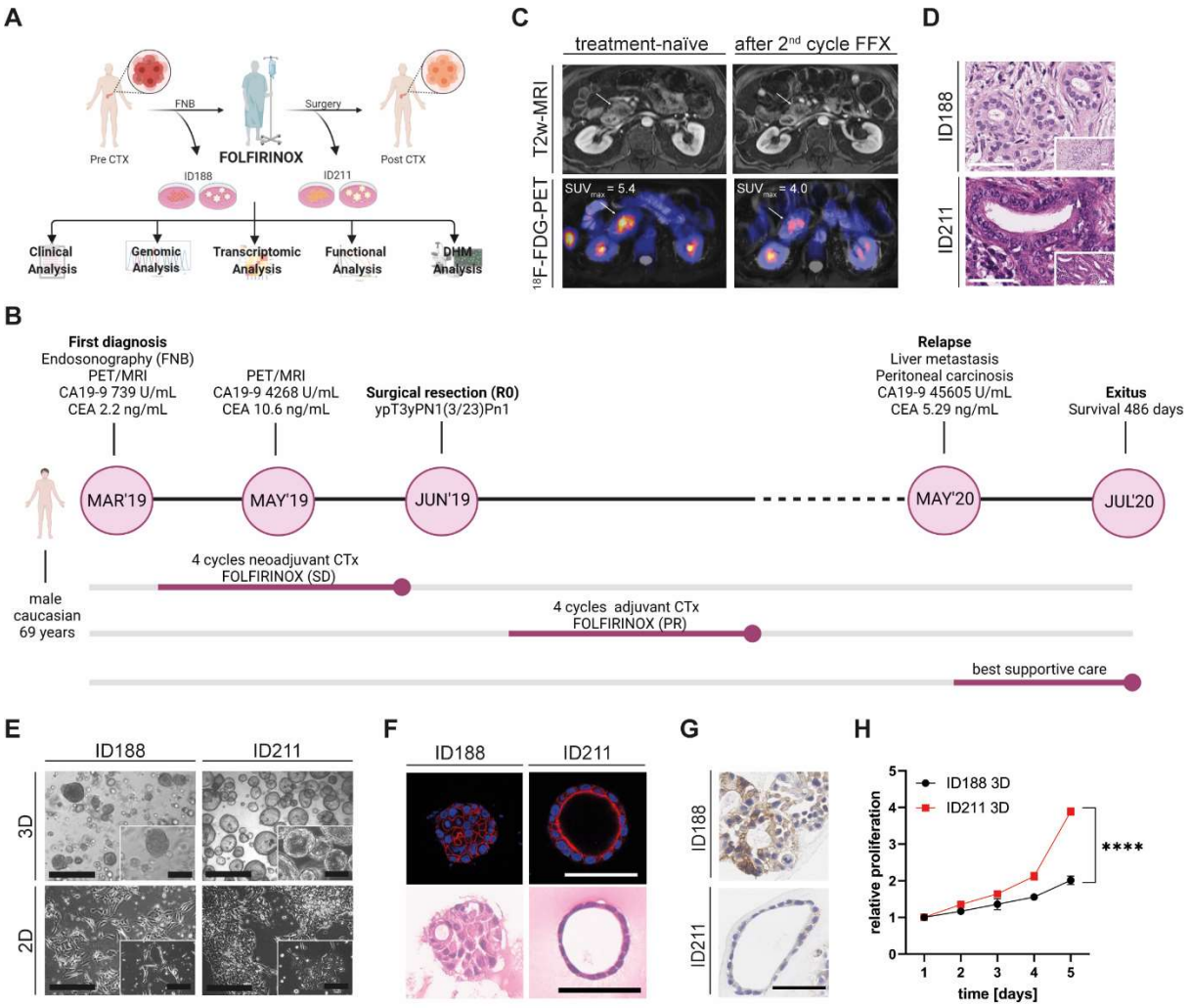

Figure 18. Generation and characterization of chemotherapy-naïve and -exposed patient-derived models to investigate treatment-imposed reprogramming.
A, Schematic illustration of the biopsy strategy and downstream applications. B, Clinical history of a PDAC patient receiving perioperative FOLFIRINOX including follow-up. C, ^{18}F-FDG PET-MRI at the time of the diagnosis and in the interim staging after one cycle of FOLFIRINOX. D, H&E staining of FNB and the resection specimen. Scale bar represents 50µm. E, Phase-contrast images of organoids (upper panel) and respective 2D cultures (isolated from the biopsy before FOLFIRINOX (ID188) or after the neoadjuvant therapy from the resected cancer (ID211). Scale bar represents 200µm. F, Immunofluorescence staining of the F-Actin filaments (upper panel) and HE staining (lower panel) in ID188 and ID211 organoids. Scale bars represent 50 µm. G, GLUT1 IHC staining of embedded and sectioned organoids. Scale bar represents 50 µm. H, Proliferation of ID188 and ID211 measured using CellTiter Glo assay for five consecutive days. Shown is the mean ±SEM of three independent replicates. Unpaired student´s t test on day 5, **** p<0.0001.

6.3.2 Genomic and transcriptomic characterization of FFX-induced changes

Since Chan-Seng-Yue et al. observed a re-differentiation from the basal-like to classical PDAC subtype after Gem/nP treatment due to a clonal selection during treatment leading to a reduction of mutant *KRAS* from $KRAS^{Ma}$ to $KRAS^{Ba}$ (Chan-Seng-Yue et al., 2020), we performed whole-exome sequencing of both organoid lines, as well. However, this did not reveal a general genomic instability or variation in *KRAS* copy numbers caused by FFX administration (Figure 19A). In fact, both organoid lines shared the same driver mutations such as $KRAS^{G12D}$, $MEN1^{L329P}$ or $MAP2K4^{R298C}$ and showed highly similar SNVs with a relevant mutant allele frequency (Figure 19B) suggesting that in this case these adaptive processes upon chemotherapy were driven by tumor cell plasticity rather than changes in the genetic landscape of the tumor. Transcriptomic PDAC subtyping using the purity independent subtyping of tumors (PurIST) as single sample classifier, which is based on 8 gene pairs each composed of a basal-like (gene 1) and classical (gene 2) gene, revealed a classical PDAC subtype in both organoid lines (Rashid et al., 2020). However, the probability of being basal-like was reduced in ID211 (0.00829) compared to ID188 (0.02073) suggesting a certain degree of re-differentiation (Figure 19C). This was verified on protein levels using western blot analysis. While the expression of E-Cadherin was increased in ID211, the mesenchymal markers Vimentin and KRT81 were decreased in ID211 (Figure 19D). The GSEA of both organoid transcriptomes further revealed a decreased activation of pathways associated with the basal-like PDAC subtype such as KRAS and TGF-β signaling, cell cycle, hypoxia as well as inflammation in ID211 compared to ID188 (Figure 19E). Additionally, in accordance with the reduced signal in ^{18}F-FDG-PET after FFX induction, glycolysis was depleted in the ID211, while OXPHOS and fatty acid metabolism were strongly increased compared to ID188.

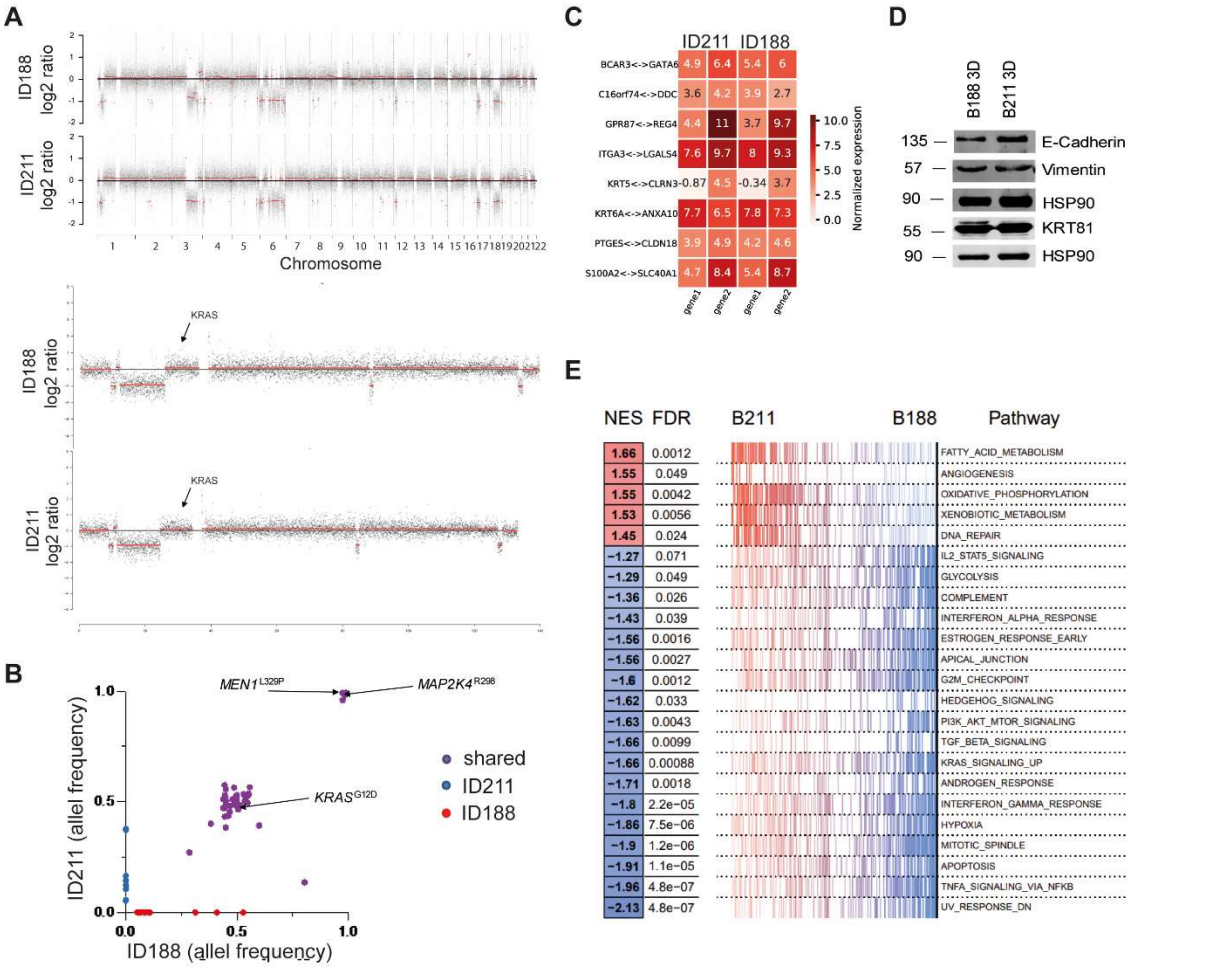

Figure 19. Molecular characterization of chemotherapy-naïve and -exposed patient-derived models to investigate treatment-imposed reprogramming.
A, Allele frequencies of miss- and nonsense SNVs and Indels which are shared between both organoid lines (purple), private to ID188 (red) or private to ID211 (blue). B, Whole exome sequencing-based copy number profiles for ID188 and ID211 organoids. C, Normalized expression (log_2 scale) for gene pairs evaluated during Purity independent subtyping of tumors (PurIST) for pre-(ID188) and post-treatment (ID211) PDO lines. D, Gene Set Enrichment Analysis (GSEA) of the indicated HALLMARK gene sets on a gene expression signature between post-(ID211, on the left)) and pre-treatment (ID188, on the right) PDO lines. Genes were sorted from high (positive in red, leftmost) to low (negative in blue, rightmost) log_2 fold change. The respective genes from each gene set are indicated by vertical bars whose color matches their position in the signature. Results are summarized as the normalized enrichment score (NES) and the associated adjusted p-value.

6.3.3 Functional layer to identify phenotypic changes and actionable targets upon FFX

In order to analyze the morphological differences in an unbiased fashion, we imaged the single cells with DHM for detailed 3D information (Figure 20A). Using Random Forest classification, we were able to differentiate pre and post FFX-treated cells in roughly 88% of cells (Figure 20B). Furthermore, we detected a left shift in the post FFX organoids ID211 confirming a certain degree of re-differentiation upon FFX treatment as observed on the molecular level with decreased KRAS signaling (Figure 20C, D). Interestingly, comparing the single cell distance to cluster centroid identified a highly significant decrease in intratumoral heterogeneity upon FFX treatment in ID211 compared to ID188 (Figure 20E). This is in line with results derived from the murine FFX treatment suggesting that FFX significantly reduces intratumoral heterogeneity in epithelial PDAC cells (Figure 16C).

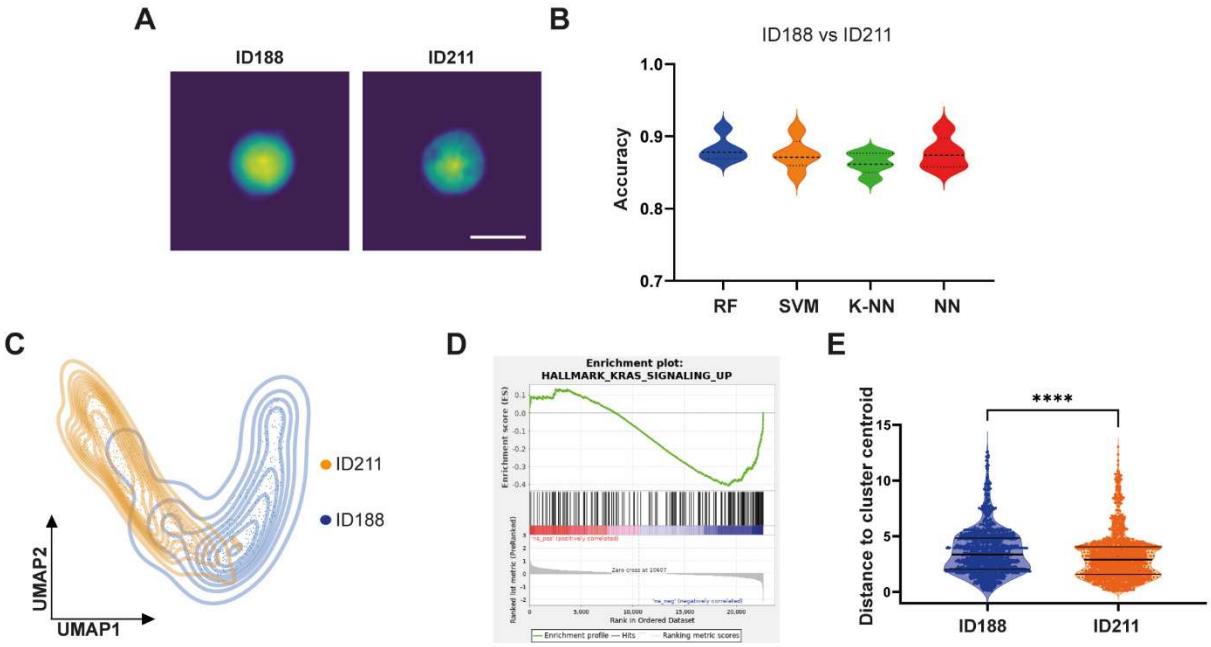

Figure 20. DHM-based identification of phenotypic changes upon FFX treatment in PDOs.
A, DHM phase images of pre (ID188) and post (ID211) FFX-treated organoids. Scale bars indicate 10 µm. B, Accuracy for separating ID188 and ID211 using different classification methods: random forest (RF), support vector machine (SVM), K-nearest neighbors (K-NN) and neuronal network (NN). C, Unsupervised clustering of ID188 and ID211 organoids based on DHM phase images and visualized using UMAP plots. D, Gene set enrichment analysis (HALLMARK gene sets) based on transcriptomic profiles of organoids pre and post FOLFIRINOX treatment. E, Evaluation of intra-organoid line heterogeneity of ID188 and ID211 using single cell distance to cluster centroid. Mann-Whitney test, ****p<0.0001.

Next, we investigated whether these molecular and phenotypic changes upon FFX administration were functionally relevant and can be used as potential chemotherapy-induced vulnerabilites for targeted therapies. Therefore, the 2D cells of ID188 and ID211 were subjected to an unbiased drug screen with a drug library containing 415 compounds (Figure 21A). Delta AUC between ID188 and ID211 was analyzed for all drugs and a threshold of >0.3 and <-0.3 was set to obtain top hits (Figure 21B). Interestingly, the top drugs that showed a highly different response between ID188 and ID211 were EGFR (Lapatinib, Poziotinib) and MEK inhibitors (Trametinib, Cobimetinib, BI-847325) proving evidence for the functional relevance of these targets.

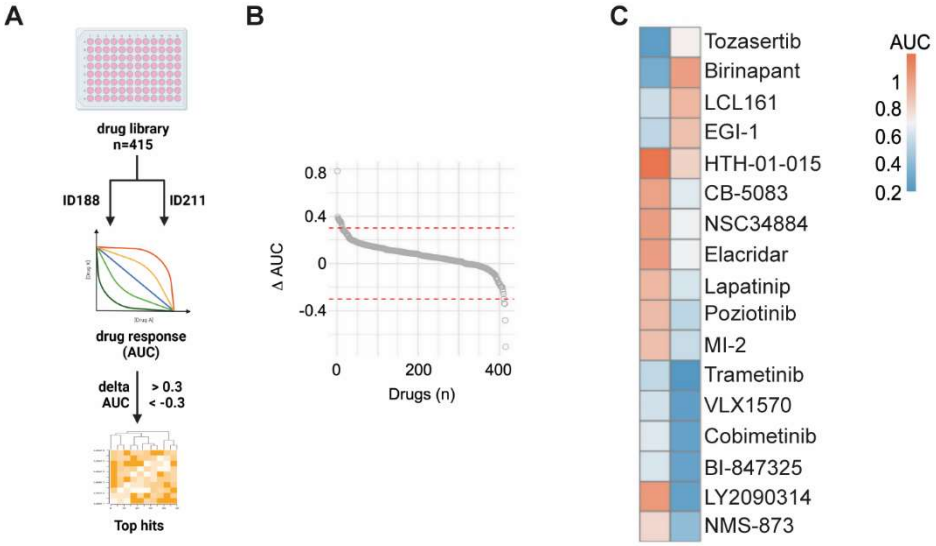

Figure 21. Unbiased drug screening revealed FFX-induced vulnerabilities.
A, Schematic illustration of the drug screen workflow. B, Delta AUC of 415 drugs in ID188 versus ID211. Red lines indicate the threshold of >0.3 and <-0.3. C, Heatmap of top hits derived from the unbiased drug screening with highest deviation of drug response between ID188 and ID211.

In order to validate these findings in the organoid lines, we performed drug screens with the EGFR inhibitors Lapatinib and Poziotinib and the MEK inhibitors Cobimetinib and Binimetinib. Although the OXPHOS inhibitor Elesclomol did not meet the inclusion criteria in the unbiased drug screening (delta AUC 0.15), we additionally included the OXPHOS inhibitors IACS-010759 and PF-3758309 for validation, as the OXPHOS gene set was stronly upregulated in ID211 compared to ID188 on mRNA level.

We observed in all three target groups a left shift of the drug-response curve in the post-FFX line ID211 indicating an increased sensitivity (Figure 22A, C, E). Although for the EGFR inhibitors it is just a trend, for the MEK and OXPHOS inhibitors the AUC was significantly decreased in ID211 compared to ID188 proving their functional relevance (Figure 22B, D, F).

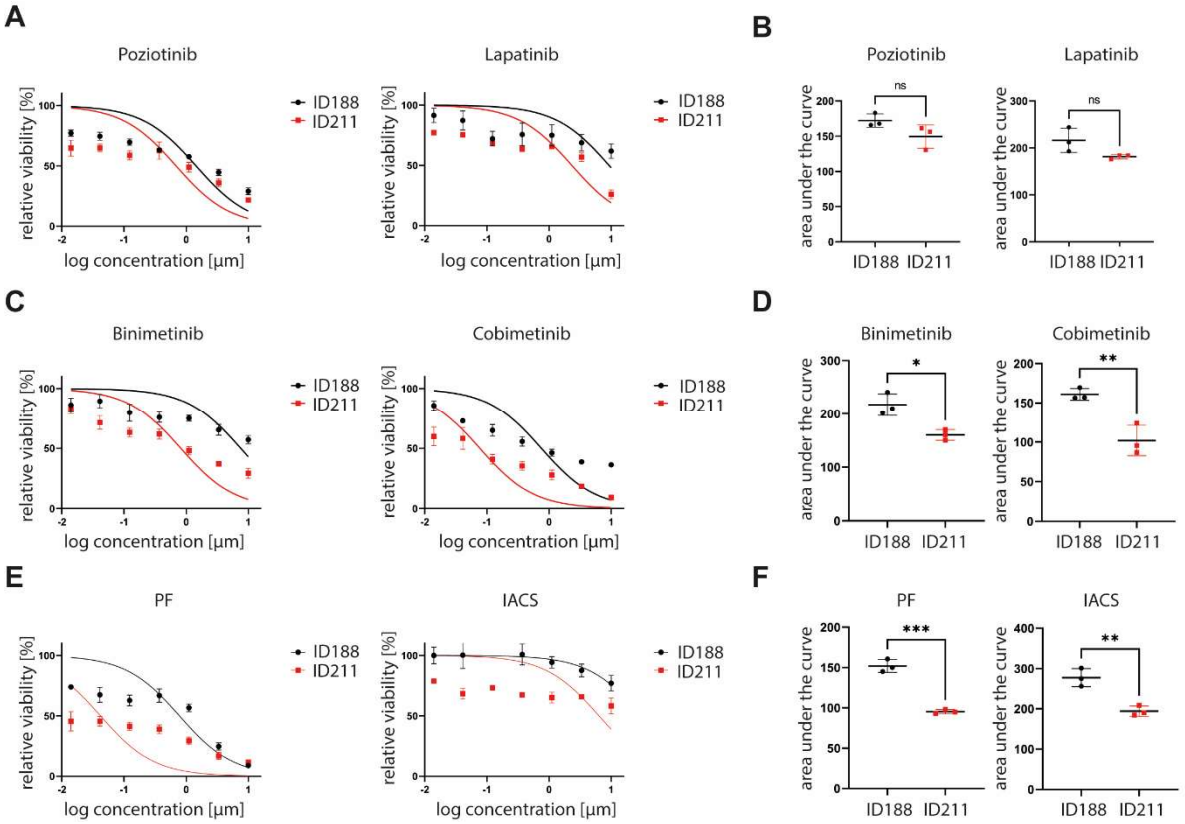

Figure 22. Functional screening of FOLFIRINOX-induced vulnerabilities.
A, C and E, Dose response curves of ID188 and ID211 treated with EGFR inhibitors (A), MEK inhibitors (B) and OXPHOS inhibitors (C) for 72h. Viability was measured using CellTiter Glo assay. Shown is the mean ±SEM of three independent replicates. B, D and F, Calculation of area under the curve for EGFR inhibitors (B), MEK inhibitors (D) and OXPHOS inhibitors. Student´s t test with ns=not significant, *p<0.05, **p<0.01 and ***p<0.001.

We further validated the efficacy of the MEK inhibitors Binimetinib and Cobimetinib and therefore stained the PDOs treated with different drug concentrations for the proliferation marker Ki67 (Figure 23A). As mentioned above, in the untreated condition ID188 exhibited a reduced proliferation compared to ID211 (Figure 18H). However, upon treatment the proliferation of ID188 remained mainly unaffected, whereas the proliferation of ID211 decreased in a dose-dependent manner in both treatment regimens confirming an increased sensitivity in the FFX-treated PDOs (Figure 23A, B). Additionally, we stained for the phosphorylation of ERK, the downstream target of MEK, and found a slight decrease in ID188 upon treatment, while the ERK phosphorylation was highly decreased in ID211 in the highest concentration of both MEK inhibitors (Figure 23C, D). Interestingly, the expression of ERK was significantly increased upon MEK inhibition in ID211 indicating a feedback loop due to a decreased ERK phosphorylation (Figure 23C, D). Despite the fact that both models were classified as classical PDAC subtype, they highly differ in their responsivness towards targeted therapies such as MEK inhibition suggesting to implement an additional functional layer such as unbiased drug screenings for precision oncology.

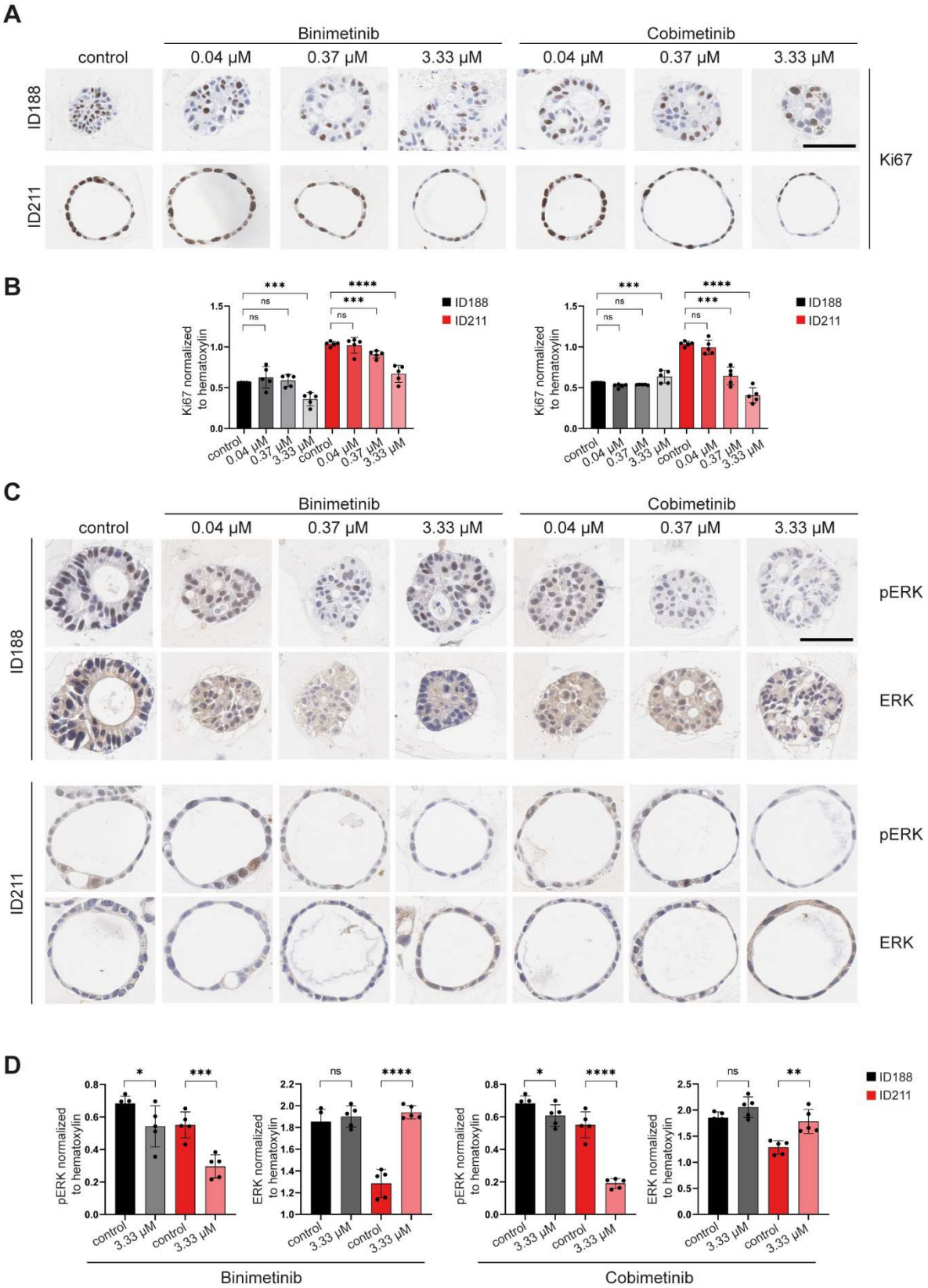

Figure 23. Validating the efficacy of MEK inhibition pre and post FOLFIRINOX treatment.
A, Ki67 staining of ID188 and ID211 upon 24 hours of Binimetinib and Cobimetinib treatment. Scale bar indicates 50 µm. B, Quantification of Ki67 normalized to hematoxylin (n = 5 organoid images). Student´s t test with ns=not significant, *p<0.05, ***p<0.001 and ****p<0.0001. C, Phospho-ERK and ERK staining of ID188 and ID211 upon 24 hours of Binimetinib and Cobimetinib treatment. Scale bar indicates 50 µm. D, Quantification of pERK and ERK normalized to hematoxylin (n = 5 organoid images). Student´s t test with ns=not significant, *p<0.05, **p<0.01, ***p<0.001 and ****p<0.0001.

7 Discussion

7.1 DHM as label-free tool for high-throughput characterization of PDAC

PDAC is a complex disease with a highly diverse tumor composition including tumor cells as well as the tumor microenvironment with CAFs and different immune cell populations. However, the tumoral compartment itself displays an extensive inter- but also intratumoral heterogeneity, which is a key parameter for overall survival, dissemination and treatment response. Several studies have been performed using scRNAseq approaches to identify intratumoral heterogeneity in PDAC specimen and PDO cultures and they found a co-existence of the classical and basal-like tumor cells in majority of the samples ((Chan-Seng-Yue et al., 2020; Juiz et al., 2020; Krieger et al., 2021).

Currently, the characterization of PDAC takes place mainly by in-depth molecular analysis using multi-omics technologies with RNA- and DNA-sequencing as well as proteomics approaches mainly from bulk tumors. Even though these genomic and transcriptomic analysis were substantial contributions for understanding the tumor biology in the past (Bailey et al., 2016; Chan-Seng-Yue et al., 2020; Collisson et al., 2011; Moffitt et al., 2015), the considerable amount of time and money make it very difficult to implement these procedures into clinical routine for diagnostic and functional purposes. Information about the tumor differentiation and composition is needed immediately in order to not waste time and treat PDAC patients right.

Therefore, in this study we established DHM as a novel tool for the high-throughput characterization of PDAC heterogeneity on a single cell level in real-time. This approach allows us to examine samples in a rapid and cost-efficient fashion without the need of prior labeling and staining procedures. Samples are processed to a single-cell suspension and subjected to DHM measurement, followed by a computational analysis composed of segmentation, filtering, feature extraction and the final classification and visualization. We first started with cells – epithelial cells versus fibroblasts – most distinct in their respective phenotypes and continued with different characterized human and murine epithelial as well as (quasi-)mesenchymal PDAC cells in order to prime the applied algorithm for different stages of EMT. We found a high degree of intratumoral heterogeneity even in cell lines classified as epithelial or mesenchymal according to their transcriptomic profiles. Furthermore, we were able to monitor treatment-induced phenotypic changes upon TGF-β and FFX treatment on a single cell level, which allowed us to track changes in intratumoral heterogeneity as well. Here, we observed a phenotype-specific change in intratumoral heterogeneity upon FFX treatment with a decrease in epithelial and an increase in mesenchymal PDAC cells. The ultimate goal of this DHM approach is to directly analyze patient biopsies, FNAs as well as surgical resections, in order

to obtain detailed information regarding tumor cell plasticity as well as tumor composition and TME in a clinically-relevant time frame.

Since EMT is a major factor for chemoresistance and patient outcome, many research projects in the field of holographic imaging have focused on this particular process, as well. For instance, Kamlund et al. applied digital holographic cytometry to human and mouse epithelial and mesenchymal cell lines grown in an adherent condition, which presented highly differentiated morphological features. The digital holographic cytometry-derived correlation matrix was then used to develop an epithelial-mesenchymal phenotypic classifier score, which was tested with different cell lines as well as under TGF-ß treatment. They could show a peak of this classifier score 16 hours after TGF-ß administration, which remained significantly different until the end time point (Kamlund S, 2020). Similarly, noncancerous epithelial and mesenchymal cells cultured on plates were used to establish an epithelial-mesenchymal score based on machine learning algorithms in order to grade cancer cells. This algorithm was then applied to the breast cancer cells MCF-7 and MDA-MB-231 with mixed morphology in order to test the algorithm. While MCF-7 cells exhibited a more epithelial score, the MDA-MB-231 cells showed rather a mesenchymal score (Lam et al., 2020). Moreover, the metastatic potential of PDAC cells was assessed using DHM-derived quantitative phase images. The segmentation-based evaluation of the phase images revealed a decreased cell thickness and increased elongation in the cells with higher metastatic potential compared to the ones with low metastatic potential. Tracking the movement of these cells on plates over 12 hours showed additionally a higher motility and longer distance of the highly metastatic cells (Kastl et al., 2019). Varol et al. used DHM in combination with fluidic chips as well in order to detect the dynamic process of EMT by TGF-ß treatment. However, in contrast to our approach they used the fluidic chip to reduce the signal-to-noise ratio introduced by the cell culture medium and seeded cells into three different channels. A watershed transform-based segmentation method allowed them to detect morphological changes during 48 hours of TGF-ß treatment derived from the cell depth maps. DHM-obtained parameters such as eccentricity, describing the circularity of a cell, as well as surface area as an indicator for adhesion was decreased during the process of EMT (Varol et al., 2020). Although these studies present a similar approach compared to ours in order to detect the different stages of EMT, all of the experiments are based on cells grown in 2D in an adherent state leading to a bias in cellular morphology due to cell culture conditions. Using a microfluidic cytometry chip, Liu et al. tried to mimic the circulatory system in order to study cancer heterogeneity and invasive phenotypes by separating cells by size and transportability. The transportability-derived parameters cell stiffness and cell-surface frictional property were further on used to distinguish epithelial from basal-like breast cancer cells. High transportability was observed in the basal-like subtype as

well as the epithelial breast cancer cell line MCF-7 treated with EMT-inducer 12-O-tetradecanoylphorbol-13-acetate. Increased transportability was additionally correlated with an up-regulation of the cancer stem cell marker CD44. Interestingly, they have analyzed the transportability parameters of single tumor cells located in the periphery versus the center derived from mouse tumor xenografts. Tumor cells located in the center showed a decreased transportability correlating with high E-cadherin and low vimentin expression, while contradictory behavior was observed in tumor cells derived from the tumor periphery (Liu et al., 2015). Moreover, an automated microfluidic technology with a uniform delivery was established allowing to probe single-cell deformability of pleural effusions in a high-throughput manner in order to obtain useful information regarding cytoskeleton rearrangement, degree of differentiation as well as metastatic potential. They used constructed deformability profiles of 47 patients to characterize disease stages such as control, acute or chronic inflammation as well as malignancy. Especially cases with diagnosed malignancy showed an increase in cell size as well as increased deformability. They furthermore analyzed the effects of cytoskeletal perturbation on the cellular deformability. Blebbistatin treatment, which is inhibiting myosin contractility, changed the deformation capacity with an increased population of deformable cells (Gossett et al., 2012). These novel single-cell technologies based on the investigation of cellular phenotypes is not only useful for the tumor characterization but might have diagnostic value, as well. In order to establish a rapid, quantitative and easy-to-implement biomarker in clinical oncology, it is necessary to distinguish phenotypic characteristics of several different cell types present in e.g. tumor tissue, blood, ascites or pleural fluids. Therefore, in the future we will use single-cell phase images of different cell populations of the TME such as various leukocytes including lymphocytes, myeloid-derived suppressor cells, monocytes and granulocytes as well as CAFs in order to accurately differentiate them from the tumor cells. A similar approach was performed using six breast cancer cells as well as the lymphocyte cells THP-1 and monocyte cells Jurkat in a stationary cell culture setting. The leukocytes were in general of smaller size with a reduced cell area as well as volume and optical thickness. Especially the volume showed a 3-fold and the cell area a 2-fold increase in the tumor cells compared to the leukocytes (El-Schich et al., 2020). In a real-time and stain-free classification, Nissim et al. tried to differentiate single cancer cells from leukocytes in flow as well using a microfluidic channel alike ours and subjected resulting quantitative phase images to machine learning classification based on support vector machines and feature extraction. The leukocytic cell population with monocytes, erythrocytes, lymphocytes and granulocytes could be predicted with a probability ranging from 82.6 to 97.8 percentage depending on the cell line. The classification of the primary colon cancer cells SW-480 and the corresponding lymph node metastasis cells SW-620 achieved a separation of 97.5 and 90.1 percentage, respectively (Nissim et al., 2020). So far, DHM approaches mainly focus on the identification of CTCs in

blood samples, the identification of various cell populations derived from patient tumor biopsies has not yet been described in literature. Thus, we would like to establish an experimental and analysis pipeline for the measurement of primary and metastatic PDAC specimen on a single cell level in order to fully characterize tumor composition as well as intratumoral heterogeneity. However, considering the various cell types present in these PDAC specimen ranging from CAFs, lymphocytes, tissue-associated macrophages, classical and quasi-mesenchymal tumor cells as well as healthy endothelial and acinar cells detected via single-cell transcriptomics (Lin et al., 2020; Peng et al., 2019), the major challenge in this approach is to accurately identify each cell population and distinguish it from others.

Apart from already mentioned applications for PDAC, an interesting and promising application of DHM is to monitor treatment response and treatment-induced vulnerabilities in PDAC cells as well as patients in order to obtain clinically relevant information. Here, we have treated different cell lines from both transcriptomic subtypes with FFX and identified a phenotypic shift towards a more mesenchymal phenotype in all lines, however to various extents. In contrast, we were able to correctly identify a shift towards a more epithelial phenotype in PDOs (ID211) isolated after neoadjuvant FFX treatment. In addition, DHM allowed us to quantify changes in intratumoral heterogeneity. Thereby, we detected a significant decrease in intratumoral heterogeneity in epithelial/classical PDAC cells upon FFX administration, while it highly increased in mesenchymal cells. Being able to analyze intratumoral heterogeneity will allow us to directly monitor for instance the efficacy of neoadjuvant chemotherapy in patients. Once we observe an increase in heterogeneity, we can assume that the treatment regimen will fail as tumor cells will rapidly acquire resistance eventually suggesting to change treatment.

Monitoring treatment response is of high interest also in the field of DHM and imaging. For instance, drug-resistant ovarian cancer cells as well as platinum-resistant endometrial cancer cells were distinguished from their sensitive counterparts using DHM-derived morphological parameters such as cell height and density (Singh et al., 2017; Yao et al., 2019). Using tissue dynamics spectroscopic imaging of a 3D grown intestinal adenocarcinoma line as well as *ex vivo* grown human esophageal tumor biopsies treated with different chemotherapeutic drugs detected spatial drug response variabilities (Li et al., 2020). High-throughput drug screening approaches often possess limited predictive power and fail, since they do not consider intratumoral heterogeneity. Thus, several technologies are evolving for testing chemosensitivity on a single-cell level including droplet-based microfluidics, fluorescence imaging, flow/mass/ghost cytometry or single-cell RNA sequencing (Jabs et al., 2017; Yang et al., 2021).

The advantage of the DHM approach for drug testing is the automated high-throughput procedure, which does not require prior labeling, can be performed in a scalable and cost-

effective manner and is analyzed in a standardized fashion. In the future, DHM can be included into our precision oncology platform as additional functional layer for testing and monitoring patient drug response.

7.2 Treatment-induced vulnerabilities in PDAC

As PDAC patients often rapidly acquire resistance towards chemotherapies such as FFX and Gem/nP, deciphering treatment-induced vulnerabilities might allow to additionally apply targeted therapies in order to effectively kill escaping tumor cells. Here, we characterized in detail short-term and prolonged resistance mechanisms occurring upon FFX and Gem/nP treatment in murine and human 2D and 3D functional model systems.

Treating murine PDAC cells, derived from the epithelial and mesenchymal transcriptomic subtype, with both standard of care polychemotherapies in a time course experiment including wash out phase allowed us to analyze phenotype- and treatment-specific response processes. Interestingly, the identified adaptive mechanisms occurred rather in a phenotype- and treatment-independent fashion. In general, we observed a phenotypic shift towards a more mesenchymal phenotype in all cell lines, which could be confirmed by DHM-based single cell phenotyping and proteomic and transcriptomic analysis with an increased upregulation of EMT and TGF-β signaling. Additionally, metabolic processes such as glycolysis, OXPHOS, fatty acid metabolism and hypoxia were highly upregulated upon chemotherapy. Interestingly, also mechanisms involved in inflammatory response including TNFA, IL-2 and 6 as well as IFN-γ signaling were upregulated upon treatment accompanied by an increased production of ROS. Furthermore, we identified genes in our RNA sequencing data set that were up- or downregulated for a prolonged time period such as *Egln3* and *Ddit4l*. Both genes are known to be involved in cellular metabolism making them an attractive target for functional screenings.

In parallel, we compared in detail the tumor of one PDAC patient before and after neoadjuvant FFX treatment using a longitudinal precision oncology platform. Although both PDO lines were classified as classical PDAC and did not show significant alterations in their genomic landscape, they drastically differed regarding cellular phenotype and response to targeted therapies. In this setting, FFX administration in the patient induced a susceptibility for the inhibition of the EGFR, MEK and OXPHOS pathways in ID211, suggesting beneficial effects when applied as targeted therapies in combination or consecutively with FFX. Expanding this precision oncology platform for additional patients will enable us to apply personalized medicine and identify uniform resistance mechanisms occurring upon chemotherapy administration.

Comparing the murine and human study, we found similarities particularly in the metabolic switch towards enhanced OXHPOS and fatty acid metabolism based on GSEA. Interestingly, chemotherapy-resistant acute myeloid leukemia cells were found to have an increased mitochondrial mass with increased OXPHOS and fatty acid oxidation, which was additionally accompanied by an increased production of ROS, similar to what we observed in our GSEA. Targeting these metabolic processes re-sensitized tumor cells for the first-line chemotherapy treatment (Farge et al., 2017). Likewise, chemoresistant breast cancer cells showed a phenotypic change towards a more aggressive state with increased expression of CD44 accompanied by increased expression of cytokines such as IL-6 and IL-23 and IFN-γ. This in turn resulted in enhanced oxidative stress with ROS production and HIF1A expression, leading to an increase in GLUT1 expression and glycolysis. When inhibiting the cytokines, CD44-high chemoresistant breast cancer cells returned back to their original phenotype. Additionally, the inhibition of the mitochandrial machinery, which is a major driver of ROS production (Sena and Chandel, 2012), reduced oxidative stress and thus the secretion of pro-oxidative cytokiness. Interestingly, they found chemoresistant tumor cells to escape and tolerate oxidative stress by increasingly activating the pentose-phosphate pathway (Goldman et al., 2019). Due to a high concordance between this resistance mechanism and pathways enriched upon FFX and Gem/nP treatment, this signaling network deserves to be followed up in future in our experimental setting of murine PDAC cells, as well.

The major discrepancy between our murine and human chemotherapy studies is that all murine cells, independent of baseline morphology, underwent EMT during and after treatment, whereas the post-FFX PDOs and 2D cells acquired a more epithelial-like phenotype upon FFX treatment *in vivo*. Recent studies investigating the impact of chemotherapy-induced vulnerabilities suggest rather a one-way direction towards a more aggressive mesenchymal phenotype. Porter et al. performed a FFX treatment of six patient-derived 3D PDAC cell lines and found an enrichment of the quasi-mesenchymal subtype in all lines after 14 days of treatment. GSEA identified MYC targets, KRAS signaling, EMT and TNFA signaling as top enriched pathways. Additionally, they compared a cohort of untreated versus neoadjuvant FFX-treated PDAC tissue specimen and identified an increase in the QM subtype from 37.5% to 67% (Porter et al., 2019). Moreover, single-nucleus RNA sequencing of untreated and neoadjuvant treated PDAC specimen detected a depletion of the classical subtype favoring more quasi-mesenchymal signatures such as TNFA and IFN-γ signaling (Hwang, 2020). Futhermore, tissue and PDOs of five untreated and five neoadjuvant FFX-treated tumors was compared regarding resistance mechanisms. GSEA of the Reactome gene sets identified mainly genomic instability and alternative energy metabolism as upregulated pathways, whereas immune system and senescence were downregulated upon treatment (Farshadi et

al., 2021). However, the major limitation of all these studies is that treatment-naïve and chemotherapy-treated samples were not derived from the same patient, which makes a direct comparison more challenging and strengthens our approach using this longitudinal precision oncology platform.

Pishvaian et al. performed molecular profiling of PDAC in the Know Your Tumor registry trial in order to apply targeted therapies, which allowed a survival advantage of 2.58 years versus 1.51 years with unmatched therapies (Pishvaian et al., 2020). However, 3 out of 4 patients did not reveal actionable targets, similar to the patient in our study, who only showed a few mutations including *KRAS*^{G12D}. Therefore, functional screenings are essential add-ons for precision oncology, as molecular characterization alone is mostly insufficient to effectively propose targeted therapies. In the past, similar screening approaches were performed in different tumor entities in order to evaluate the functional relevance of inhibiting genes of interest for precision oncology. Vecchione et al. performed a short hairpin RNA screening for genes solely upregulated in the *BRAF*-mutant subtype of colorectal cancer, which can be exploited therapeutically. They have identified the RAN binding protein 2 to be essential for the survival of the BRAF-mutant but not the BRAF-WT tumors cells. Further effective *in vitro* and *in vivo* inhibition experiments allowed them to suggest this gene as a potent target for precision oncology in *BRAF*-mutant colorectal cancer (Vecchione et al., 2016). Similar to PDAC, melanoma patients often acquire resistance towards inhibition of the MAPK pathway. Therefore, Wang et al. have generated MEK- and BRAF-resistant melanoma cells and tested them for functional and genomic differences to their parental and sensitive counterparts. They identified a strong correlation between increased resistance and increasing levels of ROS. Treating the ROS-high resistant tumor cells with histone deacetylase inhibitors further enhanced ROS production to a lethal dosage, while their drug-sensitive counterparts stayed unaffected demonstrating the effectiveness of testing for functional relevance (Wang et al., 2018). Furthermore, a kinome-focused screening was performed in hepatocellular carcinoma, in which the DNA replication kinase CDC7 was identified to selectively induce senescence in *Trp53*-mutant cancer cells. A follow-up chemical testing detected the antidepressant sertraline to potently kill escaping tumor cells by targeting the mTOR pathway (Wang et al., 2019). These studies clearly illustrate the benefit of adding functional screenings to the molecular characterization in order to identify treatment-induced vulnerabilities and in future successfully apply targeted therapies.

7.3 Conclusion

In summary, in this study we have established and combined two functional approaches for the detailed characterization of treatment-induced vulnerabilities in pancreatic cancer. Using DHM-based phenotyping allowed us to detect the single cell EMT status of numerous cell lines including PDOs and additionally gave insight into the degree of intratumoral heterogeneity. By now, it is still a major challenge to asses intratumoral heterogeneity on a cellular level in clinical routine, which is why our DHM approach is a significant contribution for the implementation of easy-to-use single cell technologies into clinics. In addition, we have applied a longitudinal precision oncology platform with in-depth genomic, transcriptomic and particularly functional characterization of PDAC specimen and functional model systems in a neoadjuvant setting. This allowed us to identify and validate treatment-induced vulnerabilities such as the sensitivity towards MEK inhibition. In future, integrating both approaches into clinics will enable us to apply personalized medicine to PDAC patients by identifying functionally relevant targets and monitoring treatment response.

8 Acknowledgement

Hereby, I would like to thank everyone who contributed to the success of this PhD thesis.

First, I thank Prof. Dr. Maximilian Reichert for giving me the chance to work on this interesting project, for his advice and support, valuable comments on the project as well as revision of the thesis.

I owe my gratitude to Prof. Dr. Roland Schmid for giving me the opportunity to work in his department, the II. Medizinische Klinik and Poliklinik at Klinikum rechts der Isar.

I also would like to thank Prof. Dr. Heiko Witt and PD Dr. Rickmer Braren for their kindness being members of my PhD thesis committee.

Furthermore, I owe my gratitude to…

… Manuel Lengl, Stefan Röhrl, Christian Klenk, David Fresacher, Farid Harb and Nawal Hafez for performing DHM measurement and image analysis in order to help establish the DHM workflow in pancreatic cancer.
… Dr. Rupert Öllinger and Dr. Carlo Maurer for rapid RNA sequencing and bioinformatic analysis.
… Carmen Escorial-Iriarte and Patrick Wustrow, who contributed to my project with their work.
… Nicole Kabella for proteomic measurement and analysis.
… Hannah Jakubowsky for performing the automated drug screening.
… the CPE team with Olga Seelbach, Marion Mielke and Nils Wirges for histopathological support.
… all members from Schneider, Saur and Rad lab for technical support.
… all my colleagues from the Reichert lab – especially Aris, Ash (thesis revision), Karin, Raphela and Zahra – for fruitful discussions and the nice atmosphere in the lab.
… Joanna Madej for her friendship and unforgettable moments making this journey a lot easier.
… Tobias Wittenzellner for his support and revision of the thesis.

Last but not least, I especially thank my family and my friends who always supported me in the past four years to successfully finish this doctoral thesis.

9 Publications, patents and awards

Peschke K*, Jakubowski H*, Schäfer A, Maurer C, Lange S, Orben F, Bernad R, Harder FN, Eiber M, Öllinger R, Schlitter M, Weichert W, Veit P, Schlag C, Schmid RM, Braren RF, Kong B, Demir I, Friess H, Rad R, Saur D, Schneider G*, Reichert M*. (2021). Identification of treatment-induced vulnerabilities in pancreatic cancer patients using functional model systems. EMBO Molecular Medicine (in revision, *equal contribution).

Randriamanantsoa S*, Papargyriou A*, Maurer C, **Peschke K**, Schuster M, Steiger K, Öllinger R, Saur D, Scheel C, Rad R, Hannezo E, Reichert M*, Bausch AR*. (2021). Spatiotemporal dynamics of self-organised branching pancreatic cancer-derived organoids. Nature Communications (in revision, *equal contribution).

Feldmann K, Maurer C, **Peschke K**, Teller S, Schuck K, Steiger K, Engleitner T, Öllinger R, Nomura A, Wirges N, Papargyriou A, Sarker RSJ, Ranjan RA, Dantes Z, Weichert W, Rustgi AK, Schmid RM, Rad R, Schneider G, Saur D, Reichert M. (2021). Mesenchymal Plasticity Regulated by Prrx1 Drives Aggressive Pancreatic Cancer Biology. Gastroenterology; 160:346–385

Dantes Z, Yen HY, Pfarr N, Winter C, Steiger K, Muckenhuber A, Hennig A, Lange S, Engleitner T, Öllinger R, Maresch R, Orben F, Heid I, Georgios Kaissis, Shi K, Topping G, Stögbauer F, Wirth M, **Peschke K**, Papargyriou A, Rezaee-Oghazi M, Feldmann K, Schäfer APG, Ranjan R, Lubeseder-Martellato C, Stange DE, Welch T, Martingnoni M, Ceyhan GO, Friess H, Herner A, Liotta L, Treiber M, von Figura G, Abdelhafez M, Klare P, Schlag C, Algül H, Siveke J, Braren R, Weirich G, Weichert W, Saur D, Rad R, Schmid RM, Schneider G, Reichert M. (2020). Implementing cell-free DNA of pancreatic cancer patient–derived organoids for personalized oncology. JCI Insight 5 (15): e137809.

Poster Award: “Label-free high-throughput digital holographic microscopy to characterize pancreatic cancer heterogeneity on a single-cell level”, SFB1321 Young Scientists Retreat, Munich 2021

Patent submission: “Analysis of tissue samples using quantitative phase-contrast microscopy”, 6th of November 2020

Poster Award: “The role of epithelial plasticity in chemotherapeutic resistance occurring in PDAC.” Deutscher Pankreasclub, Halle 2020

10 References

Abal, M., Andreu, J. M., and Barasoain, I. (2003). Taxanes: microtubule and centrosome targets, and cell cycle dependent mechanisms of action. Curr Cancer Drug Targets *3*, 193-203.

Adamska, A., Domenichini, A., and Falasca, M. (2017). Pancreatic Ductal Adenocarcinoma: Current and Evolving Therapies. Int J Mol Sci *18*.

Alvarez, M. J., Shen, Y., Giorgi, F. M., Lachmann, A., Ding, B. B., Ye, B. H., Califano, A. (2016). Network-based inference of protein activity helps functionalize the genetic landscape of cancer. Nat Genet *48(8): 838-847*.

Apte, M. V., Xu, Z., Pothula, S., Goldstein, D., Pirola, R. C., and Wilson, J. S. (2015). Pancreatic cancer: The microenvironment needs attention too! Pancreatology *15*, S32-38.

Arumugam, T., Ramachandran, V., Fournier, K. F., Wang, H., Marquis, L., Abbruzzese, J. L., Gallick, G. E., Logsdon, C. D., McConkey, D. J., and Choi, W. (2009). Epithelial to mesenchymal transition contributes to drug resistance in pancreatic cancer. Cancer Res *69*, 5820-5828.

Aung, K. L., Fischer, S. E., Denroche, R. E., Jang, G. H., Dodd, A., Creighton, S., Southwood, B., Liang, S. B., Chadwick, D., Zhang, A.*, et al.* (2018). Genomics-Driven Precision Medicine for Advanced Pancreatic Cancer: Early Results from the COMPASS Trial. Clin Cancer Res *24*, 1344-1354.

Bailey, P., Chang, D. K., Nones, K., Johns, A. L., Patch, A. M., Gingras, M. C., Miller, D. K., Christ, A. N., Bruxner, T. J., Quinn, M. C.*, et al.* (2016). Genomic analyses identify molecular subtypes of pancreatic cancer. Nature *531*, 47-52.

Baldwin, S. A., Mackey, J. R., Cass, C. E., and Young, J. D. (1999). Nucleoside transporters: molecular biology and implications for therapeutic development. Mol Med Today *5*, 216-224.

Becker, A. E., Hernandez, Y. G., Frucht, H., and Lucas, A. L. (2014). Pancreatic ductal adenocarcinoma: risk factors, screening, and early detection. World J Gastroenterol *20*, 11182-11198.

Bian, Y., Zheng, R., Bayer, F. P., Wong, C., Chang, Y. C., Meng, C., Zolg, D. P., Reinecke, M., Zecha, J., Wiechmann, S.*, et al.* (2020). Robust, reproducible and quantitative analysis of thousands of proteomes by micro-flow LC-MS/MS. Nat Commun *11*, 157.

Biankin, A. V., Waddell, N., Kassahn, K. S., Gingras, M. C., Muthuswamy, L. B., Johns, A. L., Miller, D. K., Wilson, P. J., Patch, A. M., Wu, J.*, et al.* (2012). Pancreatic cancer genomes reveal aberrations in axon guidance pathway genes. Nature *491*, 399-405.

Boser, B. E., Guyon, I. M., Vapnik, V. N. (1992). A training algorithm for optimal margin classifiers. Proceedings of the fifth annual workshop on Computational learning theory - COLT '92, 144–152.

Breiman, L. (2001). Random Forests. Mach Learn *45(1), 5-21*.

Bruchard, M., Mignot, G., Derangere, V., Chalmin, F., Chevriaux, A., Vegran, F., Boireau, W., Simon, B., Ryffel, B., Connat, J. L.*, et al.* (2013). Chemotherapy-triggered cathepsin B release in myeloid-derived suppressor cells activates the Nlrp3 inflammasome and promotes tumor growth. Nat Med *19*, 57-64.

Burris, H. A., 3rd, Moore, M. J., Andersen, J., Green, M. R., Rothenberg, M. L., Modiano, M. R., Cripps, M. C., Portenoy, R. K., Storniolo, A. M., Tarassoff, P.*, et al.* (1997). Improvements in survival and clinical benefit with gemcitabine as first-line therapy for patients with advanced pancreas cancer: a randomized trial. J Clin Oncol *15*, 2403-2413.

Calin, V. L., Mihailescu, M., Scarlat, E. I., Baluta, A. V., Calin, D., Kovacs, E., Savopol, T., and Moisescu, M. G. (2017). Evaluation of the metastatic potential of malignant cells by image processing of digital holographic microscopy data. FEBS Open Bio *7*, 1527-1538.

Chan-Seng-Yue, M., Kim, J. C., Wilson, G. W., Ng, K., Figueroa, E. F., O'Kane, G. M., Connor, A. A., Denroche, R. E., Grant, R. C., McLeod, J.*, et al.* (2020). Transcription phenotypes of pancreatic cancer are driven by genomic events during tumor evolution. Nat Genet *52*, 231-240.

Chan, K. K. W., Guo, H., Cheng, S., Beca, J. M., Redmond-Misner, R., Isaranuwatchai, W., Qiao, L., Earle, C., Berry, S. R., Biagi, J. J.*, et al.* (2020). Real-world outcomes of FOLFIRINOX vs gemcitabine and nab-paclitaxel in advanced pancreatic cancer: A population-based propensity score-weighted analysis. Cancer Med *9*, 160-169.

Chuang, V. T., Kragh-Hansen, U., and Otagiri, M. (2002). Pharmaceutical strategies utilizing recombinant human serum albumin. Pharm Res *19*, 569-577.

Clark, N. A., Hafner, M., Kouril, M., Williams, E. H., Muhlich, J. L., Pilarczyk, M., Niepel, M., Sorger, P. K., and Medvedovic, M. (2017). GRcalculator: an online tool for calculating and mining dose-response data. BMC Cancer *17*, 698.

Collisson, E. A., Sadanandam, A., Olson, P., Gibb, W. J., Truitt, M., Gu, S., Cooc, J., Weinkle, J., Kim, G. E., Jakkula, L.*, et al.* (2011). Subtypes of pancreatic ductal adenocarcinoma and their differing responses to therapy. Nat Med *17*, 500-503.

Conroy, T., Desseigne, F., Ychou, M., Bouche, O., Guimbaud, R., Becouarn, Y., Adenis, A., Raoul, J. L., Gourgou-Bourgade, S., de la Fouchardiere, C.*, et al.* (2011). FOLFIRINOX versus gemcitabine for metastatic pancreatic cancer. N Engl J Med *364*, 1817-1825.

Conroy, T., Hammel, P., Hebbar, M., Ben Abdelghani, M., Wei, A. C., Raoul, J. L., Chone, L., Francois, E., Artru, P., Biagi, J. J.*, et al.* (2018). FOLFIRINOX or Gemcitabine as Adjuvant Therapy for Pancreatic Cancer. N Engl J Med *379*, 2395-2406.

Cortes, C., Vapnik, V. (1995). Support-vector networks. Mach Learn *20(3) 273-297*.

Cover, T., Hart, P. (1967). Nearest neighbor pattern classification. IEEE Trans Inf Theory *13(1) 21-27*.

Cox, J., Hein, M. Y., Luber, C. A., Paron, I., Nagaraj, N., and Mann, M. (2014). Accurate proteome-wide label-free quantification by delayed normalization and maximal peptide ratio extraction, termed MaxLFQ. Mol Cell Proteomics *13*, 2513-2526.

Cox, J., and Mann, M. (2008). MaxQuant enables high peptide identification rates, individualized p.p.b.-range mass accuracies and proteome-wide protein quantification. Nat Biotechnol *26*, 1367-1372.

Cox, J., Neuhauser, N., Michalski, A., Scheltema, R. A., Olsen, J. V., and Mann, M. (2011). Andromeda: a peptide search engine integrated into the MaxQuant environment. J Proteome Res *10*, 1794-1805.

Cunningham, P., Delany, S. J. (2021). k-Nearest Neighbour Classifiers - A Tutorial. ACM Comput Surv *54(6) 1-25*.

Daemen, A., Peterson, D., Sahu, N., McCord, R., Du, X., Liu, B., Kowanetz, K., Hong, R., Moffat, J., Gao, M.*, et al.* (2015). Metabolite profiling stratifies pancreatic ductal adenocarcinomas into subtypes with distinct sensitivities to metabolic inhibitors. Proc Natl Acad Sci U S A *112*, E4410-4417.

Dantes, Z., Yen, H. Y., Pfarr, N., Winter, C., Steiger, K., Muckenhuber, A., Hennig, A., Lange, S., Engleitner, T., Ollinger, R.*, et al.* (2020). Implementing cell-free DNA of pancreatic cancer patient-derived organoids for personalized oncology. JCI Insight *5*.

Desai, N., Trieu, V., Yao, Z., Louie, L., Ci, S., Yang, A., Tao, C., De, T., Beals, B., Dykes, D., *et al.* (2006). Increased antitumor activity, intratumor paclitaxel concentrations, and endothelial cell transport of cremophor-free, albumin-bound paclitaxel, ABI-007, compared with cremophor-based paclitaxel. Clin Cancer Res *12*, 1317-1324.

Driehuis, E., van Hoeck, A., Moore, K., Kolders, S., Francies, H. E., Gulersonmez, M. C., Stigter, E. C. A., Burgering, B., Geurts, V., Gracanin, A., *et al.* (2019). Pancreatic cancer organoids recapitulate disease and allow personalized drug screening. Proc Natl Acad Sci U S A.

El-Schich, Z., Janicke, B., Alm, K., Dizeyi, N., Persson, J. L., and Wingren, A. G. (2020). Discrimination between Breast Cancer Cells and White Blood Cells by Non-Invasive Measurements: Implications for a Novel In Vitro-Based Circulating Tumor Cell Model Using Digital Holographic Cytometry. Applied Sciences *10(14), 4854*.

El-Schich, Z., Moelder, A. L., and Wingren, A. G. (2018). Quantitative Phase Imaging for Label-Free Analysis of Cancer Cells—Focus on Digital Holographic Microscopy. Applied Sciences *8, 1027*.

Farge, T., Saland, E., de Toni, F., Aroua, N., Hosseini, M., Perry, R., Bosc, C., Sugita, M., Stuani, L., Fraisse, M., *et al.* (2017). Chemotherapy-Resistant Human Acute Myeloid Leukemia Cells Are Not Enriched for Leukemic Stem Cells but Require Oxidative Metabolism. Cancer Discov *7*, 716-735.

Farshadi, E. A., Chang, J., Sampadi, B., Doukas, M., Van 't Land, F., van der Sijde, F., Vietsch, E. E., Pothof, J., Koerkamp, B. G., and van Eijck, C. H. J. (2021). Organoids Derived from Neoadjuvant FOLFIRINOX Patients Recapitulate Therapy Resistance in Pancreatic Ductal Adenocarcinoma. Clin Cancer Res *27*, 6602-6612.

Feldmann, K., Maurer, C., Peschke, K., Teller, S., Schuck, K., Steiger, K., Engleitner, T., Ollinger, R., Nomura, A., Wirges, N., *et al.* (2021). Mesenchymal Plasticity Regulated by Prrx1 Drives Aggressive Pancreatic Cancer Biology. Gastroenterology *160*, 346-361 e324.

Goldman, A., Khiste, S., Freinkman, E., Dhawan, A., Majumder, B., Mondal, J., Pinkerton, A. B., Eton, E., Medhi, R., Chandrasekar, V., *et al.* (2019). Targeting tumor phenotypic plasticity and metabolic remodeling in adaptive cross-drug tolerance. Sci Signal *12*.

Gossett, D. R., Tse, H. T., Lee, S. A., Ying, Y., Lindgren, A. G., Yang, O. O., Rao, J., Clark, A. T., and Di Carlo, D. (2012). Hydrodynamic stretching of single cells for large population mechanical phenotyping. Proc Natl Acad Sci U S A *109*, 7630-7635.

Gourgou-Bourgade, S., Bascoul-Mollevi, C., Desseigne, F., Ychou, M., Bouche, O., Guimbaud, R., Becouarn, Y., Adenis, A., Raoul, J. L., Boige, V.*, et al.* (2013). Impact of FOLFIRINOX compared with gemcitabine on quality of life in patients with metastatic pancreatic cancer: results from the PRODIGE 4/ACCORD 11 randomized trial. J Clin Oncol *31*, 23-29.

Grunwald, B. T., Devisme, A., Andrieux, G., Vyas, F., Aliar, K., McCloskey, C. W., Macklin, A., Jang, G. H., Denroche, R., Romero, J. M.*, et al.* (2021). Spatially confined sub-tumor microenvironments in pancreatic cancer. Cell *184*, 5577-5592 e5518.

Guillaumond, F., Leca, J., Olivares, O., Lavaut, M. N., Vidal, N., Berthezene, P., Dusetti, N. J., Loncle, C., Calvo, E., Turrini, O.*, et al.* (2013). Strengthened glycolysis under hypoxia supports tumor symbiosis and hexosamine biosynthesis in pancreatic adenocarcinoma. Proc Natl Acad Sci U S A *110*, 3919-3924.

Guillaumond, F., and Vasseur, S. (2013). The metabolic facet of pancreatic cancer: how hypoxia shapes fatal cancer cells. Cell Cycle *12*, 1155-1156.

Hafner, M., Niepel, M., Chung, M., and Sorger, P. K. (2016). Growth rate inhibition metrics correct for confounders in measuring sensitivity to cancer drugs. Nat Methods *13*, 521-527.

Hahne, H., Pachl, F., Ruprecht, B., Maier, S. K., Klaeger, S., Helm, D., Medard, G., Wilm, M., Lemeer, S., and Kuster, B. (2013). DMSO enhances electrospray response, boosting sensitivity of proteomic experiments. Nat Methods *10*, 989-991.

Harder, F. N., Jungmann, F., Kaissis, G. A., Lohofer, F. K., Ziegelmayer, S., Havel, D., Quante, M., Reichert, M., Schmid, R. M., Demir, I. E.*, et al.* (2021). [(18)F]FDG PET/MRI enables early chemotherapy response prediction in pancreatic ductal adenocarcinoma. EJNMMI Res *11*, 70.

He, K., Zhang, X., Ren, S., Sun, J. (2015). Deep Residual Learning for Image Recognition. ArXiv151203385 Cs.

Herranz, N., and Gil, J. (2018). Mechanisms and functions of cellular senescence. J Clin Invest *128*, 1238-1246.

Hishinuma, S., Ogata, Y., Tomikawa, M., Ozawa, I., Hirabayashi, K., and Igarashi, S. (2006). Patterns of recurrence after curative resection of pancreatic cancer, based on autopsy findings. J Gastrointest Surg *10*, 511-518.

Hornik, K., Stinchbombe, M. (1989). Multilayer feedforward networks are universal approximators. Neural Netw *2(5) 259-336*.

Hruban, R. H., Adsay, N. V., Albores-Saavedra, J., Compton, C., Garrett, E. S., Goodman, S. N., Kern, S. E., Klimstra, D. S., Kloppel, G., Longnecker, D. S.*, et al.* (2001). Pancreatic intraepithelial neoplasia: a new nomenclature and classification system for pancreatic duct lesions. Am J Surg Pathol *25*, 579-586.

Hruban, R. H., Maitra, A., Kern, S. E., and Goggins, M. (2007). Precursors to pancreatic cancer. Gastroenterol Clin North Am *36*, 831-849, vi.

Huang, P., Chubb, S., Hertel, L. W., Grindey, G. B., and Plunkett, W. (1991). Action of 2',2'-difluorodeoxycytidine on DNA synthesis. Cancer Res *51*, 6110-6117.

Huang, P., and Plunkett, W. (1995). Induction of apoptosis by gemcitabine. Semin Oncol *22*, 19-25.

Hwang, W. L., Jagadeesh, K. A., Guo, J. A., Hoffman, H. I., Yadollahpour, P., Mohan, R., Drokhlyansky, E., Van Wittenberghe, N., Ashenberg, O., Farhi, S., Schapiro, D., reeves, J., Zollinger, D. R., Eng, G., Schenkel, J. M., Free-Pastor, W. A., Rodrigues, C., Gould, J., Lambden, C., Porter, C., Tsankov, A., Dionne, D., Abbondanza, D., Waldman, J., Cuoco, M., Nguyen, L., Delorey, T., Phillips, D., Ciprani, D., Kern, M., Mehta, A., Furhman, K., Fropf, R., Beechem, J., Loeffler, J. S., Ryan, D. P., Weekes, C. D., Ting, D. T., Ferrone, C. R., Wo, J. Y., Hong, T. S., Aguirre, A. J., Rozenblatt-Rosen, O., Kenudson, M. M., Fernandez-del Castillo, C., Liss, A. S., Jacks, T. Regev, A. (2020). Single-nucleus and spatial transcriptomics of archival pancreatic cancer reveals multi-compartment reprogramming after neoadjuvant treatment. Biorxiv.

Jabs, J., Zickgraf, F. M., Park, J., Wagner, S., Jiang, X., Jechow, K., Kleinheinz, K., Toprak, U. H., Schneider, M. A., Meister, M.*, et al.* (2017). Screening drug effects in patient-derived cancer cells links organoid responses to genome alterations. Mol Syst Biol *13*, 955.

Jones, S., Hruban, R. H., Kamiyama, M., Borges, M., Zhang, X., Parsons, D. W., Lin, J. C., Palmisano, E., Brune, K., Jaffee, E. M.*, et al.* (2009). Exomic sequencing identifies PALB2 as a pancreatic cancer susceptibility gene. Science *324*, 217.

Juiz, N., Elkaoutari, A., Bigonnet, M., Gayet, O., Roques, J., Nicolle, R., Iovanna, J., and Dusetti, N. (2020). Basal-like and classical cells coexist in pancreatic cancer revealed by single-cell analysis on biopsy-derived pancreatic cancer organoids from the classical subtype. FASEB J *34*, 12214-12228.

Kamlund S, J. B., Alm K, Judson-Torres RL, Oredsson S (2020). Quantifying the Rate, Degree, and Heterogeneity of Morphological Change during an Epithelial to Mesenchymal Transition Using Digital

Holographic Cytometry. Applied Sciences *10, 4726*.

Kanda, M., Matthaei, H., Wu, J., Hong, S. M., Yu, J., Borges, M., Hruban, R. H., Maitra, A., Kinzler, K., Vogelstein, B., and Goggins, M. (2012). Presence of somatic mutations in most early-stage pancreatic intraepithelial neoplasia. Gastroenterology *142*, 730-733 e739.

Kastl, L., Kemper, B., and Schnekenbuger, J. (2019). Cancer cells metastatic potential measurement by quantitative phase microscopy. SPIE Proceedings *Vol. 10887*.

Kelstrup, C. D., Bekker-Jensen, D. B., Arrey, T. N., Hogrebe, A., Harder, A., and Olsen, J. V. (2018). Performance Evaluation of the Q Exactive HF-X for Shotgun Proteomics. J Proteome Res *17*, 727-738.

Kindler, H. L., Ioka, T., Richel, D. J., Bennouna, J., Letourneau, R., Okusaka, T., Funakoshi, A., Furuse, J., Park, Y. S., Ohkawa, S.*, et al.* (2011). Axitinib plus gemcitabine versus placebo plus gemcitabine in patients with advanced pancreatic adenocarcinoma: a double-blind randomised phase 3 study. Lancet Oncol *12*, 256-262.

Kindler, H. L., Niedzwiecki, D., Hollis, D., Sutherland, S., Schrag, D., Hurwitz, H., Innocenti, F., Mulcahy, M. F., O'Reilly, E., Wozniak, T. F.*, et al.* (2010). Gemcitabine plus bevacizumab compared with gemcitabine plus placebo in patients with advanced pancreatic cancer: phase III trial of the Cancer and Leukemia Group B (CALGB 80303). J Clin Oncol *28*, 3617-3622.

Kingma, D. P., Ba, J. (2017). Adam: A Method for Stochastic Optimization. ArXiv14126980 Cs.

Kitada, T., Seki, S., Sakaguchi, H., Sawada, T., Hirakawa, K., and Wakasa, K. (2003). Clinicopathological significance of hypoxia-inducible factor-1alpha expression in human pancreatic carcinoma. Histopathology *43*, 550-555.

Ko, A. H., LoConte, N., Tempero, M. A., Walker, E. J., Kate Kelley, R., Lewis, S., Chang, W. C., Kantoff, E., Vannier, M. W., Catenacci, D. V.*, et al.* (2016). A Phase I Study of FOLFIRINOX Plus IPI-926, a Hedgehog Pathway Inhibitor, for Advanced Pancreatic Adenocarcinoma. Pancreas *45*, 370-375.

Kolde, R. (2019). pheatmap: Pretty Heatmaps.

Korotkevich, G., Sukhov, V., Budin, N., Shpak, B., Artyomov, M.N., Sergushichev, A. (2021). Fast gene set enrichment analysis. Biorxiv.

Krieger, T. G., Le Blanc, S., Jabs, J., Ten, F. W., Ishaque, N., Jechow, K., Debnath, O., Leonhardt, C. S., Giri, A., Eils, R.*, et al.* (2021). Single-cell analysis of patient-derived PDAC organoids reveals cell state heterogeneity and a conserved developmental hierarchy. Nat Commun *12*, 5826.

Lam, V., Nguyen, T., Bui, V., Chung, B. M., Chang, L. C., Nehmetallah, G., and Raub, C. (2020). Quantitative scoring of epithelial and mesenchymal qualities of cancer cells using machine learning and quantitative phase imaging. J Biomed Opt *25*, 1-17.

Li, Z., Hu, B., Li, G., Fox, S., Jalal, S., Turek, J., Brown, J. Q., and Nolte, D. (2020). Tissue dynamics spectroscopic imaging: functional imaging of heterogeneous cancer tissue. J Biomed Opt *25*.

Liberzon, A., Birger, C., Thorvaldsdottir, H., Ghandi, M., Mesirov, J. P., and Tamayo, P. (2015). The Molecular Signatures Database (MSigDB) hallmark gene set collection. Cell Syst *1*, 417-425.

Lin, W., Noel, P., Borazanci, E. H., Lee, J., Amini, A., Han, I. W., Heo, J. S., Jameson, G. S., Fraser, C., Steinbach, M.*, et al.* (2020). Single-cell transcriptome analysis of tumor and stromal compartments of pancreatic ductal adenocarcinoma primary tumors and metastatic lesions. Genome Med *12*, 80.

Liu, L. F., Desai, S. D., Li, T. K., Mao, Y., Sun, M., and Sim, S. P. (2000). Mechanism of action of camptothecin. Ann N Y Acad Sci *922*, 1-10.

Liu, Q., Liao, Q., and Zhao, Y. (2017). Chemotherapy and tumor microenvironment of pancreatic cancer. Cancer Cell Int *17*, 68.

Liu, Z., Lee, Y., Jang, J., Li, Y., Han, X., Yokoi, K., Ferrari, M., Zhou, L., and Qin, L. (2015). Microfluidic cytometric analysis of cancer cell transportability and invasiveness. Sci Rep *5*, 14272.

Longley, D. B., Harkin, D. P., and Johnston, P. G. (2003). 5-fluorouracil: mechanisms of action and clinical strategies. Nat Rev Cancer *3*, 330-338.

Love, M. I., Huber, W., and Anders, S. (2014). Moderated estimation of fold change and dispersion for RNA-seq data with DESeq2. Genome Biol *15*, 550.

Macosko, E. Z., Basu, A., Satija, R., Nemesh, J., Shekhar, K., Goldman, M., Tirosh, I., Bialas, A. R., Kamitaki, N., Martersteck, E. M.*, et al.* (2015). Highly Parallel Genome-wide Expression Profiling of Individual Cells Using Nanoliter Droplets. Cell *161*, 1202-1214.

Mathijssen, R. H., Loos, W. J., Verweij, J., and Sparreboom, A. (2002). Pharmacology of topoisomerase I inhibitors irinotecan (CPT-11) and topotecan. Curr Cancer Drug Targets *2*, 103-123.

McInnes, L., Healy, J., Saul, N., Großberger, L. (2018). UMAP: Uniform Manifold Approximation and Projection. Open Source Softw *3(29) 861*.

Min, J., Yao, B., Trendafilova, V., Ketelhut, S., Kastl, L., Greve, B., and Kemper, B. (2019). Quantitative phase imaging of cells in a flow cytometry arrangement utilizing Michelson interferometer-based off-axis digital holographic microscopy. J Biophotonics *12*, e201900085.

Moffitt, R. A., Marayati, R., Flate, E. L., Volmar, K. E., Loeza, S. G., Hoadley, K. A., Rashid, N. U., Williams, L. A., Eaton, S. C., Chung, A. H.*, et al.* (2015). Virtual microdissection identifies distinct tumor- and stroma-specific subtypes of pancreatic ductal adenocarcinoma. Nat Genet *47*, 1168-1178.

Molder, A., Sebesta, M., Gustafsson, M., Gisselson, L., Wingren, A. G., and Alm, K. (2008). Non-invasive, label-free cell counting and quantitative analysis of adherent cells using digital holography. J Microsc *232*, 240-247.

Mueller, S., Engleitner, T., Maresch, R., Zukowska, M., Lange, S., Kaltenbacher, T., Konukiewitz, B., Ollinger, R., Zwiebel, M., Strong, A.*, et al.* (2018). Evolutionary routes and KRAS dosage define pancreatic cancer phenotypes. Nature *554*, 62-68.

Nielsen, F. (2016). Hierarchical Clustering. Introduction to HPC with MPI for Data Science, 195-211.

Nissim, N., Dudaie, M., Barnea, I., and Shaked, N. T. (2020). Real-Time Stain-Free Classification of Cancer Cells and Blood Cells Using Interferometric Phase Microscopy and Machine Learning. Cytometry A.

Olive, K. P., Jacobetz, M. A., Davidson, C. J., Gopinathan, A., McIntyre, D., Honess, D., Madhu, B., Goldgraben, M. A., Caldwell, M. E., Allard, D.*, et al.* (2009). Inhibition of Hedgehog signaling enhances delivery of chemotherapy in a mouse model of pancreatic cancer. Science *324*, 1457-1461.

Papneja, N., Zaidi, A., Chalchal, H., Moser, M., Tan, K., Olson, C., Haider, K., Shaw, J., and Ahmed, S. (2019). Comparisons of Outcomes of Real-World Patients With Advanced Pancreatic Cancer Treated With FOLFIRINOX Versus Gemcitabine and Nab-Paclitaxel: A Population-Based Cohort Study. Pancreas *48*, 920-926.

Parekh, S., Ziegenhain, C., Vieth, B., Enard, W., and Hellmann, I. (2016). The impact of amplification on differential expression analyses by RNA-seq. Sci Rep *6*, 25533.

Patel, T. S., T., Miccio, J. A., Lacy, J., Stein, S., Kormansky, J. S., Staugaard, C., Gambaccini, M., Axtmayer, A., Cecchini, M. (2020). Clinical outcomes of first-line FOLFIRINOX versus gemcitabine plus nab-paclitaxel in metastatic pancreatic cancer at the Yale Smilow Healthcare System. J Clin Oncol *38*.

Peng, J., Sun, B. F., Chen, C. Y., Zhou, J. Y., Chen, Y. S., Chen, H., Liu, L., Huang, D., Jiang, J., Cui, G. S.*, et al.* (2019). Single-cell RNA-seq highlights intra-tumoral heterogeneity and malignant progression in pancreatic ductal adenocarcinoma. Cell Res *29*, 725-738.

Pfaffl, M. W. (2001). A new mathematical model for relative quantification in real-time RT-PCR. Nucleic Acids Res *29*, e45.

Pishvaian, M. J., Blais, E. M., Brody, J. R., Lyons, E., DeArbeloa, P., Hendifar, A., Mikhail, S., Chung, V., Sahai, V., Sohal, D. P. S.*, et al.* (2020). Overall survival in patients with pancreatic cancer receiving matched therapies following molecular profiling: a retrospective analysis of the Know Your Tumor registry trial. Lancet Oncol *21*, 508-518.

Plunkett, W., Huang, P., Xu, Y. Z., Heinemann, V., Grunewald, R., and Gandhi, V. (1995). Gemcitabine: metabolism, mechanisms of action, and self-potentiation. Semin Oncol *22*, 3-10.

Porter, R. L., Magnus, N. K. C., Thapar, V., Morris, R., Szabolcs, A., Neyaz, A., Kulkarni, A. S., Tai, E., Chougule, A., Hillis, A.*, et al.* (2019). Epithelial to mesenchymal plasticity and differential response to therapies in pancreatic ductal adenocarcinoma. Proc Natl Acad Sci U S A.

Pothula, S. P., Xu, Z., Goldstein, D., Pirola, R. C., Wilson, J. S., and Apte, M. V. (2016). Key role of pancreatic stellate cells in pancreatic cancer. Cancer Lett *381*, 194-200.

Raghavan, S., Winter, P. S., Navia, A. W., Williams, H. L., DenAdel, A., Lowder, K. E., Galvez-Reyes, J., Kalekar, R. L., Mulugeta, N., Kapner, K. S.*, et al.* (2021).

Microenvironment drives cell state, plasticity, and drug response in pancreatic cancer. Cell *184*, 6119-6137 e6126.

Rahib, L., Smith, B. D., Aizenberg, R., Rosenzweig, A. B., Fleshman, J. M., and Matrisian, L. M. (2014). Projecting cancer incidence and deaths to 2030: the unexpected burden of thyroid, liver, and pancreas cancers in the United States. Cancer Res *74*, 2913-2921.

Rahib, L., Wehner, M. R., Matrisian, L. M., and Nead, K. T. (2021). Estimated Projection of US Cancer Incidence and Death to 2040. JAMA Netw Open *4*, e214708.

Rashid, N. U., Peng, X. L., Jin, C., Moffitt, R. A., Volmar, K. E., Belt, B. A., Panni, R. Z., Nywening, T. M., Herrera, S. G., Moore, K. J.*, et al.* (2020). Purity Independent Subtyping of Tumors (PurIST), A Clinically Robust, Single-sample Classifier for Tumor Subtyping in Pancreatic Cancer. Clin Cancer Res *26*, 82-92.

Raymond, E., Faivre, S., Woynarowski, J. M., and Chaney, S. G. (1998). Oxaliplatin: mechanism of action and antineoplastic activity. Semin Oncol *25*, 4-12.

Reichert, M., Bakir, B., Moreira, L., Pitarresi, J. R., Feldmann, K., Simon, L., Suzuki, K., Maddipati, R., Rhim, A. D., Schlitter, A. M.*, et al.* (2018). Regulation of Epithelial Plasticity Determines Metastatic Organotropism in Pancreatic Cancer. Dev Cell *45*, 696-711 e698.

Reichert, M., Takano, S., Heeg, S., Bakir, B., Botta, G. P., and Rustgi, A. K. (2013). Isolation, culture and genetic manipulation of mouse pancreatic ductal cells. Nat Protoc *8*, 1354-1365.

Rhim, A. D., Mirek, E. T., Aiello, N. M., Maitra, A., Bailey, J. M., McAllister, F., Reichert, M., Beatty, G. L., Rustgi, A. K., Vonderheide, R. H.*, et al.* (2012). EMT and dissemination precede pancreatic tumor formation. Cell *148*, 349-361.

Ritchie, M. E., Phipson, B., Wu, D., Hu, Y., Law, C. W., Shi, W., and Smyth, G. K. (2015). limma powers differential expression analyses for RNA-sequencing and microarray studies. Nucleic Acids Res *43*, e47.

Roberts, N. J., Norris, A. L., Petersen, G. M., Bondy, M. L., Brand, R., Gallinger, S., Kurtz, R. C., Olson, S. H., Rustgi, A. K., Schwartz, A. G.*, et al.* (2016). Whole Genome Sequencing Defines the Genetic Heterogeneity of Familial Pancreatic Cancer. Cancer Discov *6*, 166-175.

Rosenblatt, F. (1958). The perceptron: A probabilistic model for information storage and organization in the brain. Psychol Rev *65(6) 386-408*.

Sakamoto, H., Attiyeh, M. A., Gerold, J. M., Makohon-Moore, A. P., Hayashi, A., Hong, J., Kappagantula, R., Zhang, L., Melchor, J. P., Reiter, J. G.*, et al.* (2020). The Evolutionary Origins of Recurrent Pancreatic Cancer. Cancer Discov *10*, 792-805.

Sena, L. A., and Chandel, N. S. (2012). Physiological roles of mitochondrial reactive oxygen species. Mol Cell *48*, 158-167.

Shibaji, T., Nagao, M., Ikeda, N., Kanehiro, H., Hisanaga, M., Ko, S., Fukumoto, A., and Nakajima, Y. (2003). Prognostic significance of HIF-1 alpha overexpression in human pancreatic cancer. Anticancer Res *23*, 4721-4727.

Siegel, R. L., Miller, K. D., and Jemal, A. (2020). Cancer statistics, 2020. CA Cancer J Clin *70*, 7-30.

Singh, D. K., Ahrens, C. C., Li, W., and Vanapalli, S. A. (2017). Label-free fingerprinting of tumor cells in bulk flow using inline digital holographic microscopy. Biomed Opt Express *8*, 536-554.

Subramanian, A., Tamayo, P., Mootha, V. K., Mukherjee, S., Ebert, B. L., Gillette, M. A., Paulovich, A., Pomeroy, S. L., Golub, T. R., Lander, E. S., and Mesirov, J. P. (2005). Gene set enrichment analysis: a knowledge-based approach for interpreting genome-wide expression profiles. Proc Natl Acad Sci U S A *102*, 15545-15550.

Suzuki, S., KeiichiA be (1985). Topological structural analysis of digitized binary images by border following. Computer Vision, Graphics, and Image Processing *30, 32-46*.

Tiriac, H., Belleau, P., Engle, D. D., Plenker, D., Deschenes, A., Somerville, T. D. D., Froeling, F. E. M., Burkhart, R. A., Denroche, R. E., Jang, G. H.*, et al.* (2018). Organoid Profiling Identifies Common Responders to Chemotherapy in Pancreatic Cancer. Cancer Discov *8*, 1112-1129.

Ugele, M., Weniger, M., Leidenberger, M., Huang, Y., Bassler, M., Friedrich, O., Kappes, B., Hayden, O., and Richter, L. (2018a). Label-free, high-throughput detection of P. falciparum infection in sphered erythrocytes with digital holographic microscopy. Lab Chip *18*, 1704-1712.

Ugele, M., Weniger, M., Stanzel, M., Bassler, M., Krause, S. W., Friedrich, O., Hayden, O., and Richter, L. (2018b). Label-Free High-Throughput Leukemia Detection by Holographic Microscopy. Adv Sci (Weinh) *5*, 1800761.

Varol, R., Esmer, B. G., and Uvet, H. (2020). Interferometric Measurement of TGF-β Induced Epithelial-Mesenchymal Transition of Tumor Cells. Applied Sciences *10, 9107*.

Vecchione, L., Gambino, V., Raaijmakers, J., Schlicker, A., Fumagalli, A., Russo, M., Villanueva, A., Beerling, E., Bartolini, A., Mollevi, D. G.*, et al.* (2016). A Vulnerability of a Subset of Colon Cancers with Potential Clinical Utility. Cell *165*, 317-330.

Von Hoff, D. D., Ervin, T., Arena, F. P., Chiorean, E. G., Infante, J., Moore, M., Seay, T., Tjulandin, S. A., Ma, W. W., Saleh, M. N.*, et al.* (2013). Increased survival in pancreatic cancer with nab-paclitaxel plus gemcitabine. N Engl J Med *369*, 1691-1703.

Wang, C., Vegna, S., Jin, H., Benedict, B., Lieftink, C., Ramirez, C., de Oliveira, R. L., Morris, B., Gadiot, J., Wang, W.*, et al.* (2019). Inducing and exploiting vulnerabilities for the treatment of liver cancer. Nature *574*, 268-272.

Wang, G. L., Jiang, B. H., Rue, E. A., and Semenza, G. L. (1995). Hypoxia-inducible factor 1 is a basic-helix-loop-helix-PAS heterodimer regulated by cellular O2 tension. Proc Natl Acad Sci U S A *92*, 5510-5514.

Wang, L., Leite de Oliveira, R., Huijberts, S., Bosdriesz, E., Pencheva, N., Brunen, D., Bosma, A., Song, J. Y., Zevenhoven, J., Los-de Vries, G. T.*, et al.* (2018). An Acquired Vulnerability of Drug-Resistant Melanoma with Therapeutic Potential. Cell *173*, 1413-1425 e1414.

Wang, Q., Ma, Y., Zhao, K., Tian, Y. (2020). A Comprehensive Survey of Loss Functions in Machine Learning. Ann Data Sci.

Weizman, N., Krelin, Y., Shabtay-Orbach, A., Amit, M., Binenbaum, Y., Wong, R. J., and Gil, Z. (2014). Macrophages mediate gemcitabine resistance of pancreatic adenocarcinoma by upregulating cytidine deaminase. Oncogene *33*, 3812-3819.

Yang, C., Yang, C., Yarden, Y., To, K. K. W., and Fu, L. (2021). The prospects of tumor chemosensitivity testing at the single-cell level. Drug Resist Updat *54*, 100741.

Yao, T., Cao, R., Xiao, W., Pan, F., and Li, X. (2019). An optical study of drug resistance detection in endometrial cancer cells by dynamic and quantitative phase imaging. J Biophotonics *12*, e201800443.

Zecha, J., Satpathy, S., Kanashova, T., Avanessian, S. C., Kane, M. H., Clauser, K. R., Mertins, P., Carr, S. A., and Kuster, B. (2019). TMT Labeling for the Masses: A Robust and Cost-efficient, In-solution Labeling Approach. Mol Cell Proteomics *18*, 1468-1478.

Zeng, S., Pottler, M., Lan, B., Grutzmann, R., Pilarsky, C., and Yang, H. (2019). Chemoresistance in Pancreatic Cancer. Int J Mol Sci *20*.

Zheng, X., Carstens, J. L., Kim, J., Scheible, M., Kaye, J., Sugimoto, H., Wu, C. C., LeBleu, V. S., and Kalluri, R. (2015). Epithelial-to-mesenchymal transition is dispensable for metastasis but induces chemoresistance in pancreatic cancer. Nature *527*, 525-530.